The Islamic University–Gaza
Deanship of Research and Graduate Studies
Faculty of Engineering
Master of Electrical Engineering
Control Engineering

الجامعـــــــة الإســـلاميـة – غـزة
عمادة البحث العلمي والدراسات العليا
كليـــــــــــة الهندســـــــــــة
ماجستيـــــر الهندســـة الكهربيـــة
هندســـــــــة التحكـــــــــم

Motion Estimation of On-Road Vehicles from Moving Platform Using Stereo Vision

استنباط حركة المركبات على الطريق من واجهة متحركة باستخدام الرؤية الثنائية

By
Hazem Jamal Abu Jalala

Supervised by

Dr. Hatem Elaydi
Associate Prof. of Control Engineering

Dr. Iyad Abuhadrous
Associate prof. of Computer and Control

A thesis submitted in partial fulfillment
of the requirements for the degree of
Master of Science in Electrical Engineering

May/2018

إقـــــــــــــــــــــــــــــرار

أنا الموقع أدناه مقدم الرسالة التي تحمل العنوان:

Motion Estimation of On-Road Vehicles from Moving Platform Using Stereo Vision

استنباط حركة المركبات على الطريق من واجهة متحركة باستخدام الرؤية الثنائية

أقر بأن ما اشتملت عليه هذه الرسالة إنما هو نتاج جهدي الخاص، باستثناء ما تمت الإشارة إليه حيثما ورد، وأن هذه الرسالة ككل أو أي جزء منها لم يقدم من قبل الاخرين لنيل درجة أو لقب علمي أو بحثي لدى أي مؤسسة تعليمية أو بحثية أخرى.

Declaration

I understand the nature of plagiarism, and I am aware of the University's policy on this. The work provided in this thesis, unless otherwise referenced, is the researcher's own work, and has not been submitted by others elsewhere for any other degree or qualification.

Student's name:	حازم جمال أبو جلالة	اسم الطالب:
Signature:		التوقيع:
Date:	19/5/2018	التاريخ:

بسم الله الرحمن الرحيم

الجامعة الإسلامية غزة
The Islamic University of Gaza
عمادة البحث العلمي والدراسات العليا
هاتف داخلي: 1150

ج س ع/35/
الرقم: Ref: 2018/07/11م
التاريخ: Date:

نتيجة الحكم على أطروحة ماجستير

بناءً على موافقة عمادة البحث العلمي والدراسات العليا بالجامعة الإسلامية بغزة على تشكيل لجنة الحكم على أطروحة الباحث/ **حازم جمال محمد ابوجلالة** لنيل درجة الماجستير في كلية **الهندسة**/ قسم **الهندسة الكهربائية** وموضوعها:

استنباط حركة المركبات على الطريق من واجهة متحركة باستخدام الرؤية الثنائية

Motion Estimation of On-Road Vehicles from Moving Platform Using Stereo Vision

وبعد المناقشة التي تمت اليوم **الاربعاء 15 رمضان 1439**هـ الموافق **2018/05/30**م الساعة **الثانية عشرة والنصف مساءً**، في قاعة مبنى **طيبة** اجتمعت لجنة الحكم على الأطروحة والمكونة من:

د. حاتم علي العايدي	**مشرفاً ورئيساً**	.....
د. إياد محمد أيوب أبو هدروس	**مشرفاً**	.....
د. مؤيد نصر المبيض	**مناقشاً داخلياً**	.....
د. محمد عمر عقل	**مناقشاً خارجياً**	.....

وبعد المداولة أوصت اللجنة بمنح الباحث درجة الماجستير في **كلية الهندسة/قسم الهندسة الكهربائية**.

واللجنة إذ تمنحه هذه الدرجة فإنها توصيه بتقوى الله تعالى ولزوم طاعته وأن يسخر علمه في خدمة دينه ووطنه.

والله ولي التوفيق،،،

عميد البحث العلمي والدراسات العليا

أ. د. مازن إسماعيل هنية

+97082644400 +97082644800 public@iugaza.edu.ps www.iugaza.edu.ps iugaza iugaza mediaiug iugaza
P.O Box 108, Rimal,Gaza,Palestine ص.ب 108 الرمال . غزة . فلسطين

الرقم العام للنسخة	310667	اللغة	E

التاريخ: 16/7/1438 20

الموضوع/ استلام النسخة الإلكترونية لرسالة علمية

قامت إدارة المكتبات بالجامعة الإسلامية باستلام **النسخة الإلكترونية** من رسالة

الطالب/ عازم جمال محمد أبو طالب

رقم جامعي: 12162168 قسم: هندسة التعدين كلية: الهندسة

وتم الاطلاع عليها، ومطابقتها بالنسخة الورقية للرسالة نفسها، ضمن المحددات المبينة أدناه:

- تم إجراء جميع التعديلات التي طلبتها لجنة المناقشة.
- تم توقيع المشرف/المشرفين على النسخة الورقية لاعتمادها كنسخة معدلة ونهائية.
- تم وضع ختم "عمادة الدراسات العليا" على النسخة الورقية لاعتماد توقيع المشرف/المشرفين.
- وجود جميع فصول الرسالة مجمَّعة في ملف (WORD) وآخر (PDF).
- وجود فهرس الرسالة، والملخصين باللغتين العربية والإنجليزية بملفات منفصلة (PDF +WORD).
- تطابق النص في كل صفحة ورقية مع النص في كل صفحة تقابلها في الصفحات الإلكترونية.
- تطابق التنسيق في جميع الصفحات (نوع وحجم الخط) بين النسخة الورقية والإلكترونية.

128

ملاحظة: ستقوم إدارة المكتبات بنشر هذه الرسالة كاملة بصيغة (PDF) على موقع المكتبة الإلكتروني

والله ولي التوفيق،

توقيع الطالب .....

إدارة المكتبة .....

2018

إدارة المكتبات
IUG Central Library

Abstract

In this thesis, a novel approach for estimating the motion of on-road vehicles based on stereo image sequences from a moving platform is proposed. The approach focuses on the practical situations of the on-road traffic such as oncoming traffic and turning vehicles at urban intersections. The estimated states are the 2D position and orientation (yaw) of an observed vehicle relative to the ego-vehicle, as well as the observed vehicle's velocity, acceleration and the rotational velocity (yaw rate). These parameters are estimated by means of 1st order Extended Kalman Filter provided by the stereo vision observations of tracked point on the observed vehicle's surface. The stereo vision measurement model noise is analyzed and successfully characterized for the real test data, also the dynamic models noise is analyzed and sufficiently estimated through the proposed mechanical limitations assumption. The observability property of the overall system is inspected, such that its proved analytically and numerically that the system is observable for on-road practical situations. The overall system is systematically evaluated both on synthesized and real-world data from the realistic dataset "KITTI benchmark", where the synthesized data results show that the proposed mechanically limited filter initialization and process noise variance accurately estimate the object pose and motion parameters in a very complicated situation with fast convergence, also the real data results show that the proposed system is able to reliably estimate the object pose and motion parameters in a variety of challenging situations. Finally, the limits of the system and the practical issues such as the filter initialization and the numerical errors are carefully investigated.

Keywords: Kalman Filtering, Stereo Vision, Driver Assistance System, KITTI Benchmark, Random Process.

ملخص الدراسة

يقترح هذا البحث طريقة جديدة لاستنباط متغيرات حركة المركبات على الطريق اعتمادا على دفق من صور الرؤية الثنائية يتم التقاطها من مركبة متحركة. تركز الدراسة على الحالات العملية للمرور على الطرق مثل المركبات القادمة و المركبات الملتقة على التقاطعات المرورية. تقوم الطريقة باستنباط موضع المركبة ثنائي الأبعاد و واتجاهها نسبة إلى المركبة المرجعية و سرعتها وتسارعها و معدل دوران اتجاهها. تستخدم الطريقة في استنباط المتغيرات المذكورة مرشح كلمان الموسع من الدرجة الأولى والذي يتم تزويده بقياسات الرؤية الثنائية لنقطة يتم تتبعها على سطح المركبة. في هذا البحث تم تحليل ضوضاء نموذج القياس للرؤية الثنائية وقياسها بشكل صحيح، و كذلك تم تحليل ضوضاء النموذج الديناميكي وتقديره كمياً بشكل فعال من خلال فرضية الحدود الميكانيكية للحركة. لقد تم دراسة خاصية قابلية استنباط متغيرات الحركة حيث أثبتنا أن الطريقة تتميز بهذه الخاصية في الحالات العملية للمركبات على الطرق إثباتاً تحليلياً و إثباتاً عددياً. لقد تم بشكل نظامي تقييم كامل المنظومة من خلال بيانات محاكاة و كذلك من خلال بيانات العالم الحقيقي المستقاة من قاعدة بيانات (KITTI) وقد أظهرت نتائج اختبار الطريقة من خلال البيانات المولدة للمحاكاة أنه باستخدام فرضية الحدود الميكانيكية للحركة لضبط الشروط الابتدائية للمرشح و تقويم ضوضاء النموذج الديناميكي فإن الطريقة قادرة بشكل دقيق ومستقر وسريع على استنباط المتغيرات المذكورة في حالات أصعب من الواقع العملي للمركبات على الطرق، كما أظهرت نتائج الاختبار من خلال بيانات العالم الحقيقي أن الطريقة قادرة وبشكل موثوق على الاستنباط الدقيق للمتغيرات المذكورة في العديد من السيناريوهات العملية ، أخيراً تم تبيان حدود عمل النظام والمشاكل العملية كضبط الشروط الابتدائية لعمل المرشحات و الأخطاء العددية البرمجية.

Dedication

To my beloved parents...

...brothers and sisters...

...My wife and my beloved son and daughters

Acknowledgement

I would like to dedicate the first page of the thesis to express my warmest greetings and gratitude to those without whom this thesis would not have seen the light:

First, all my thanks and gratitude go to our God and the God of all worlds ALLAH whose sincere guidance was being felt through every single step of preparing and writing up this thesis.

The second “thank you” goes to my parents, who never hesitated to provide me with all the psychological and materialistic helps in order to achieve success in my life.

A big "thank you" is presented to the loves of my life, my wife, and my son and daughters who walked me through the road of sacrifice and patience until me graduation and the successful submission of this thesis.

Finally, I would like to deeply thank my supervisors Dr. Hatem Elaydi and Dr. Iyad Abuhadrous for their patience and sincere support, guidance, and advices without which this thesis would not have been submitted in the present manner.

Table of Contents

List of Tables

List of Figures

Nomenclature

$\boldsymbol{\delta_s}$	The steering angle of the front wheel
$\boldsymbol{L}$	The distance between the front and the rear wheel
$\boldsymbol{L_r}$	The distance between rear wheel and center of mass
$\boldsymbol{\beta_C}$	The side slip angle
$\boldsymbol{\chi}$	The moving direction with in a global world coordinate system
$\boldsymbol{R_r, R_f, R_C}$	The radius of the rear, front and center of mass wheel's circular path
$\boldsymbol{\Psi}$	The yaw angle
$\boldsymbol{s}$	The arc length
$\boldsymbol{f_x, f_y}$	The focal length of the camera in the x and y direction (pixels)
$\boldsymbol{x_0, y_0}$	The coordinates of the principal point in the x and y direction (pixels)
$\boldsymbol{u, v}$	The coordinates of the projected point in the x and y direction (pixels)
$\boldsymbol{b}$	The stereo baseline
$\boldsymbol{ul, ur}$	The horizontal projection of world point on left, right stereo camera
$\boldsymbol{d}$	The stereo disparity
$\boldsymbol{x, z}$	The observed vehicle position in the horizontal plane by meters
$\boldsymbol{v}$	The polar velocity of the observed vehicle by (m/s)
$\boldsymbol{a}$	The polar acceleration of the observed vehicle by (m/s2).
$\boldsymbol{J}$	The polar jerk of the observed vehicle by (m/s3).
$\boldsymbol{h}$	The heading angle of the observed vehicle from the X-axis by (rad)
$\boldsymbol{\omega}$	The counterclockwise turn rate of the observed vehicle by (rad/s)
$\boldsymbol{\alpha}$	The turn acceleration of the observed vehicle (rad/s^2)
$\Delta\boldsymbol{x_e}, \Delta\boldsymbol{z_e}$	The ego-vehicle translational displacement at 1 time instant (m)
$\Delta\boldsymbol{h_e}$	The ego-vehicle rotational displacement at one time instant (rad)
$\boldsymbol{Q}$	the process model noise covariance matrix
$\boldsymbol{R}$	The measurement model noise covariance matrix
$\boldsymbol{\sigma_a^2}$	The variance of the process model polar acceleration by (m/s^2)
$\boldsymbol{\sigma_J^2}$	The variance of the process model forward jerk by (m/s^3)
$\boldsymbol{\sigma_\alpha^2}$	The variance of the process model turn acceleration by (rad/s^2)
$\boldsymbol{\sigma_x^2, \sigma_x^2}$	The variance of the linear measurement model measured position $\boldsymbol{x, z}$ respectively by (meters)
$\boldsymbol{\sigma_d^2, \sigma_{ul}^2}$	The variance of the nonlinear measurement model measured disparity and lateral projection respectively (pixels)
$\boldsymbol{\hat{x}_{k+1\|k}}$	Predicted (a priori) state estimate
$\boldsymbol{P_{k+1\|k}}$	Predicted (a priori) covariance estimate
$\boldsymbol{\tilde{y}_k}$	Innovation or measurement pre-fit residual
$\boldsymbol{S_k}$	Innovation (or pre-fit residual) covariance
$\boldsymbol{K_k}$	Optimal Kalman gain
$\boldsymbol{\hat{x}_{k+1\|k+1}}$	Updated (a posteriori) state estimate
$\boldsymbol{P_{k+1\|k+1}}$	Updated (a posteriori) estimate covariance

List of Abbreviations

ACC	Adaptive Cruise Control
ASIRT	Association for Safe International Road Travel
BSD	Blind Spot Detection
CSAV	Constant Steering Angle and Velocity
CCA	Constant Curvature and Acceleration
CTRA	Constant Turn Rate and Acceleration
CTRPV	Constant Turn Rate and Velocity
CT	Continuous Time
DAS	Driver Assistance Systems
DSS	Driver Support System
DT	Discrete Time
EKF	Extended Kalman Filter
ESP	Electronic Stability Program
FCW	Forward Collision Warning
ITS	Intelligent Transportation Systems
IVI	Intelligent Vehicle Initiative
KF	Kalman Filter
KITTI	Karlshure Institute of Technology and Toyota Technologies Institute
LDW	Lane departure Warning
LTI	Linear Time-Invariant
RMS	Root Mean Square
RTK	Real Time Kinematics
TSR	Traffic Sign Recognition
UKF	Unscented Kalman Filter

Chapter 1

Introduction

Chapter 1
Introduction

1.1 Motivation

According to Association for Safe International Road Travel (ASIRT) road traffic crashes rank as the 9th leading cause of death and account for 2.2% of all deaths globally since nearly 1.3 million people die and about 50 million are injured or disabled in road crashes each year (ASIRT, 2017). Therefore, the development of crashes avoidance systems, road-safety, in-vehicle information system (IVIS) and driver support systems (DSS) became a wide-open research area in the past decades. Until now there are hundreds of active projects in industry, universities, and research centers include adaptive cruise control (ACC), forward collision warning (FCW), lane departure warning (LDW), adaptive light control (ALC), traffic Sign recognition (TSR), blind spot detection (BSD), driver drowsiness detection (DDD), in-vehicle navigation system, intelligent speed adaptation (ISA), vehicle-to-vehicle (V2V) communication, on-road object recognition, and night vision etc. (Kim, S., Kang, J., Oh, S., Ryu, Y., Kim, K., Park, S., 2008). The two large projects in the literature are Intelligent vehicle initiative (IVI) funded by US Department of Transportation (1997–2005) and intelligent car initiative project (i2010) funded by European Commission. IVI aimed at preventing driver distraction, introducing of crash avoidance systems, and studying the effects of in-vehicle technologies on driver performance while i2010 project aimed to encourage smart, safe and green system for transportation and promotes cooperative research in intelligent vehicle systems (M. Akhlaq· Tarek R. Sheltami· Bo Helgeson· Elhadi M. Shakshuki, 2011). All of those systems are considered intelligent transportation systems that consists a very interesting and vital part of the smart city systems revolution.

In parallel many road environment perception modalities were developed like radio detection and ranging (Radar), light detection and ranging (Lidar), Laser scanners, sound navigation and ranging (Sonar), global positioning system (GPS) and computer vision. Although the GPS allows to reference the position of the on-road vehicles within a global coordinate system accurately, they lose this benefit in a lot on on-road situations where the satellite signals are loosed such as in confined areas. So among the above modalities the vision-based systems are becoming the most popular because of their independence from the urban infrastructure and low-cost since the cameras become

cheaper, smaller, and of higher quality than ever before (Sayanan Sivaraman,Mohan Manubhai Trivedi, 2013).

1.2 Literature Review

On-road vehicles detection and tracking has been explored by many researchers in the computer vision and intelligent transportation systems (ITS) community over the past two decades. In this section the proceeding proposed approaches in the literature will be divided into vehicle detection approaches and vehicle tracking approaches, the vehicle tracking approaches will be further divided into tracking approaches from stationary sensor platform and from moving platform, the moving platform approaches will be further divided into monocular and stereoscopic systems.

1.2.1 Vehicle Detection Approaches

The vehicle detection approaches is divided into the appearance-based approaches and the motion-based approaches that require a sequence of images for vehicle recognition. Appearance-based approaches are common in the monocular vehicle detection literature since they recognize vehicles directly from the images while motion-based approaches are common in the monocular because stereo sequences provide 3-D depth measurements. The extremely used features for appearance-based in the literature are the histogram of oriented gradient (HOG) features and Haar-like features. HOG features are descriptive image features, exhibiting good detection performance in a variety of computer vision tasks. (M. Cheon, W. Lee, C. Yoon, and M. Park,, 2012) use the symmetry of the HOG features extracted in a given image patch, along with the HOG features themselves for vehicle detection, The main drawback of HOG features is that they are quite slow to compute. Haar-like features are composed of sums and differences of rectangles over an image patch. They are well suited for real-time vehicles detection and high efficient for vehicles detection. (S. Sivaraman and M. Trivedi,, 2010) use Haar-like features to detect the rear faces of preceding vehicles using a forward-facing camera, there are other appearance-feature used in the literature like the edges, the symmetry, the scale invariant feature transform (SIFT) features, Gabor features, the principal component analysis (PCA). Although It is often more direct to use motion-based approaches in stereo vision, the motion-based approached used for monocular vision in the literature. The main used motion-based approaches are the background modeling and the optical flow.

Adaptive background models have been used in some studies, in an effort to adapt surveillance methods to the dynamic on-road environment. (A. Broggi, A. Cappalunga, S. Cattani, and P. Zani, 2008) constructed an adaptive background model with vehicles detected based on motion that differentiated them from the background. The optical flow is a fundamental machine vision tool. In the literature optical flow is used for ego-motion estimation, detection of overtaking vehicles in the blind spot, classification of the scene as either intersection or non-intersection and segmentation of the on-road scene using video (Sayanan et.al.2013).

1.2.2 Vehicle Tracking from Stationary Cameras

The vehicle tracking approaches in the literature is divided into two categories; the approaches of tracking from stationary camera and the approaches of tracking from moving platform. In the former category (Koller,D.,K. Daniilidis, and H. Nagel, 1993) proposed vision-based vehicles tracking system for surveillance of highway sections traffic using stationary cameras placed at elevated position. Koller et. al. (1993) discriminated moving objects from the background on the basis of image flow, where clusters of image positions showing mainly translational displacements between consecutive frames, were assumed to belong to single vehicles, then a parametrized 3D vehicle shape model was projected onto the image plane and aligned to edges, the detected vehicles were tracked by means of an extended Kalman filter using a 3D vehicle motion model. (Kamijo, S., Y. Matsushita, K. Ikeuchi, and M. Sakauchi, 2000) segmented moving objects from a static or adaptive background model using background subtraction, while (Mosabbeb, E., M. Sadeghi, M. Fathy, and M. Bahekmat, 2007) depends on deviations from the background model in order to group the connected foreground pixels, yielding a binary image where each pixel represents either foreground or background are further analyzed. (Buch,N.,F. Yin,J. Orwell,D. Makris, andS. A. Velastin, 2009) introduced a model free object representation based on groups of corner features to yield more stable tracking results in dense traffic situations based on the law of common fate concept of Gestalt psychologists. The idea was that a group of points moving rigidly together was assumed to belong to the same vehicle. (Leotta, M.andJ. Mundy, 2007) tracked a set of contour segments instead of corner features in order to estimate the 3D translational motion of vehicles from low camera angle.

1.2.3 Vehicle Tracking from Moving Platforms

In the category of vehicle tracking approaches from moving platforms (Badino, 2004) proposed image-based method to distinguish static from independently moving points in the scene using compensating the ego-motion; the vehicle speed and yaw rate is provided by inertial sensors; that achieve additional robustness.

1.2.4 Monocular Systems

Most publications in single camera based vision addresses tracking leading vehicles on highways using various techniques such as using image statistics (Zeng, Z.and S. Ma, 2002), using symmetry (Liu,M.,C. Wu, andY. Zhang, 2007); and using optical flow, contours and template-matching (Dahlkamp, H., A. Pece, A. Ottlik, and H. Nagel, 2004). A good survey on different vehicle detection methods from a moving platform using optical sensors is given in (Sun,Z.,G. Bebis, andR. Miller, 2004). (Leibe,B.,N. Cornelis,K. Cornelis, andL. Van Gool, 2007) utilized the combination of depth and appearance and trained local classifiers to detect characteristic objects parts in the 2D image.

1.2.5 Stereoscopic Systems

(Mark, W. van der and D. M. Gavrila, 2006) provided a good overview on stereo vision in the intelligent vehicle domain, including an extensive evaluation of different real-time stereo implementations. (Mark, W. van der and D. M. Gavrila, 2006) modeled objects as upright planes on a ground plane, such planes can be identified based on an accumulation of equal distances within an image region, where the ground plane does not necessarily have to be flat. (Labayrade,R.,D. Aubert, andJ.-P. Tarel, 2002) proposed a solution for dealing with non-flat roads using v-disparity images. (Barrois, B., S. Hristova, C. Woehler, F. Kummert, and C. Hermes, 2009) proposed fitting the stereo vision 3D point cloud data to approximate cuboid model of the vehicle shape. (Hahn,M.,C. Wöhler,J. Einhaus,C. Hermes, and F. Kummert, 2010) proposed an approach for object tracking and motion estimation based on stereo vision, optical flow, and mean shift clustering techniques, (Dang, T., C. Hoffmann, and C. Stiller, 2002) proposed method for fusing the depth information from stereo with motion.

1.2.6 Tracking Strategies

The Kalman filter (KF) is the most popular tracking technique that assumes a Gaussian probability distribution of the estimated parameters, it has several variants and

extensions, including the Extended Kalman filter (EKF), The Unscented Kalman filter, or multi-filter approaches. Kalman filters are used in combination with a linear motion model in (Dang, T., C. Hoffmann, and C. Stiller, 2002), or with particular vehicle motion models incorporating specific properties of vehicle movements (Leibe,B.,N. Cornelis,K. Cornelis, andL. Van Gool, 2007).

Unlike KF the particle filter represents the posterior probability density function of a state estimate by a set of (random) sample state vectors drawn from this distribution (particles) that allows for modeling more complex distributions than Gaussians as well as nonlinear transformations of random variables (THRUN, Sebastian, 2005). The evolution of the particle set can be steered via a proper motion model. Hahn et. al. (2010) used particle filter with a linear motion model in or with constant turn models for tracking the 3D pose of vehicles. Although one can observe an increase in publications that utilize a particle filter, the drawback of this filter is that it is non-deterministic and, depending on the problem, computationally much more complex than the Kalman filter, even if capabilities for parallel computing are exploited. In the case of a linear Gaussian system, the particle filter can never yield a better result than the Kalman filter (Barth, 2010). However, even the suboptimal EKF, which will play a key role in this thesis, yields very promising results in many practical situations at much lower computational costs.

1.3 Problem Formulation

Consider an observed vehicle that is moving on flat road as shown in figure (1.1), which is captured through sequence from forward-facing stereo vision system from the ego vehicle, and consider a coordinate frame system that is originated at the optical center of the left camera such that the z-axis is in the direction of the ego vehicle forward direction, the x-axis is in the right direction of the ego vehicle. The observed vehicle is moving in the horizontal plane *X-Z*, with the following states:

- x, z denotes the observed vehicle position in the horizontal plane by meters
- v denotes the polar velocity of the observed vehicle that is the magnitude of the velocity vector measured by (meter/second), note that it is assumed in the same direction of the vehicle forward neglecting the side slip angle.
- a denotes the acceleration that is the time derivative of the polar velocity of the measured by (meter/second^2).
- h is the heading angle of the observed vehicle, from the X-axis to the velocity

vector measured by (radian), counterclockwise for positive angles.

- ω denotes the time derivative of the heading angle (the turn rate), measured by (radian/second), counterclockwise for positive rate.

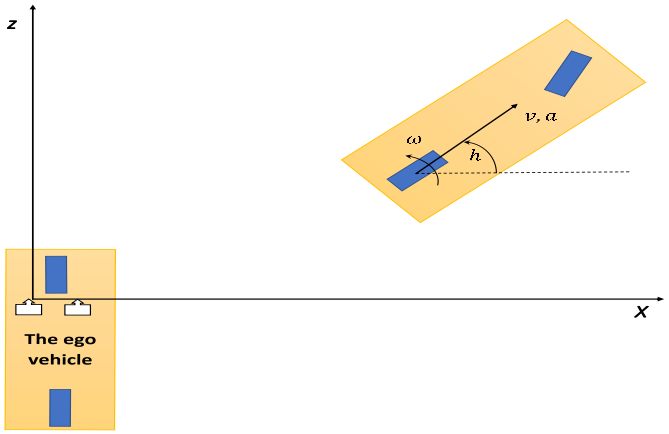

Figure (1.1): The observed vehicle in the coordinate frame of the ego-vehicle

The projection of the object on the adjacent image planes is a stream of noisy measurements of the lateral projection UL_m on the left camera and the disparity d_m for that projected point

$$\begin{bmatrix} \boldsymbol{UL_m} \\ \boldsymbol{d_m} \end{bmatrix}_{\boldsymbol{0}}, \begin{bmatrix} \boldsymbol{UL_m} \\ \boldsymbol{d_m} \end{bmatrix}_{\boldsymbol{1}}, \dots, \begin{bmatrix} \boldsymbol{UL_m} \\ \boldsymbol{d_m} \end{bmatrix}_{\boldsymbol{k}}, \begin{bmatrix} \boldsymbol{UL_m} \\ \boldsymbol{d_m} \end{bmatrix}_{\boldsymbol{k+1}}, \dots . : \ \boldsymbol{k \ is \ the \ time \ instant}$$

We will estimate the true states of the observed vehicle (x, z, v, a, h, ω) , which are constrained by the following dynamic model f and the noisy the measurement model h

$$[\boldsymbol{x, z, v, a, h, \omega}]_{\boldsymbol{k+1}} = \boldsymbol{f}([\boldsymbol{x, z, v, a, h, \omega}]_{\boldsymbol{k}}) + \boldsymbol{q_k}$$

$$\begin{bmatrix} \boldsymbol{UL_m} \\ \boldsymbol{d_m} \end{bmatrix}_{\boldsymbol{k}} = \boldsymbol{h}(\boldsymbol{x, z, v, a, h, \omega, k}) + \boldsymbol{r_k}$$

Where q_k, r_k parameterize the dynamic model and measurement model noises

1.4 Thesis Contribution

In this thesis we deployed two famous dynamic motion models; the constant turn rate and polar velocity (CTRPV), and the constant turn rate and acceleration (CTRA); in real stereo vision measurements based estimation. This study inspects the observability of the proposed approach analytically and numerically, also extends CTRPV, CTRA from global frame coordinates to a moving frame coordinates of the Karlshure Institute of Technology and Toyota Technologies Institute (KITTI) dataset ego vehicle and augment

the dataset environment parameters such that the estimator is compatible with the dataset objects motion estimation problem. An analysis of the stereo vision measurement noise was introducing, such that an adaptive measurement noise variance filters we proposed and evaluated. This study proposes reliable initialization and quantization models for noise variance of the filters using the knowledge of the mechanical limitation of the observed vehicle. The proposed approach was formulated to be extendable for deployment of any other estimation algorithms like unscented Kalman filter, interacting multiple models, particle filter, etc.

1.5 Thesis Outline

The remainder of this thesis will be organized as follows. Chapter 2 introduces the over whole architecture of our system components, also it gives the fundamental concepts of image formation and a comprehensive mathematical derivation of the on-road vehicles motion and the stereo vision. Chapter 3 introduces the notation of state estimation by EKF to be applied in later sections, then it systemizes the equations in the form of stochastic state estimation problem, manipulating the numerical instability issues and analyzing the measurement noise, ended by the demonstration of KITTI sensors processing, data extraction and coordinates reassigning. Chapter 4 addresses the observability problem analytically and numerically. The proposed system is systematically evaluated in Chapter 5 both on simulated and KITTI real-world data addressing the practical issues such as initialization measurement and system model noise characterization. An outlook on future research as well as the conclusions of this contribution is given in Chapter 6.

1.6 Research objectives

The research aims to develop a reliable and an accurate estimation algorithm of the motion of the participant on-road vehicles that are located in the recognition range of forward lateral stereo vision system, considering the realistic on-road environment challenges.

Chapter 2

System Architecture and Modeling

Chapter 2
System Architecture and Modeling

2.1 The System Development Environment

Surely it is unpractical to build the real environment for research purposes because of the high cost, unavailability of some components, installation time, and consuming efforts; instead the researchers work on well acquired datasets. In the past few years an increasing number of benchmarks were developed to push forward the performance of visual recognition systems, e.g., Caltech and Middlebury (Sayanan et. al. 2013). However, the results from state-of-the-art algorithms revealed that methods ranking high on established datasets such as Middlebury performed below average when being moved outside the laboratory to the real world since most of these datasets are simplistic and were taken in a controlled environment. Table(2.1) compares between the current State-of-the-Art Stereo-vision Benchmarks and Datasets So (Andreas Geiger and Philip Lenz and Christoph Stiller and Raquel Urtasun, 2013) developed KITTI dataset in order to reduce this bias by providing challenging benchmarks with novel difficulties to the computer vision community include non-Lambertian surfaces (e.g., reflectance, transparency), large displacements (e.g., high speed), a large variety of materials (e.g., matte vs. shiny), as well as different lighting conditions (e.g., sunny vs. cloudy). KITTI was developed as a novel challenging benchmark for the tasks of stereo, optical flow, visual odometry, simultaneous localization and mapping (SLAM) and 3D object detection (Geiger et. al. 2012).

Table (2.1): Comparison of current State-of-the-Art Benchmarks and Datasets

dataset	type	setting	#sequences	length	#frames	resolution
EISATS	synthetic	-	1	-	498	0.3 Mpx
Middlebury	laboratory	-	1	-	38	0.2 Mpx
TUM RGB-D	real	indoor	27	0.4 km	65k	0.3 Mpx
New College	real	outdoor	1	2.2 km	51k	0.2 Mpx
Malaga 2009	real	outdoor	6	6.4 km	38k	0.8 Mpx
Ford Campus	real	outdoor	2	5.1 km	7k	1.0 Mpx
KITTI	real	outdoor	22	39.2 km	41k	0.5 Mpx

2.2 System Architecture

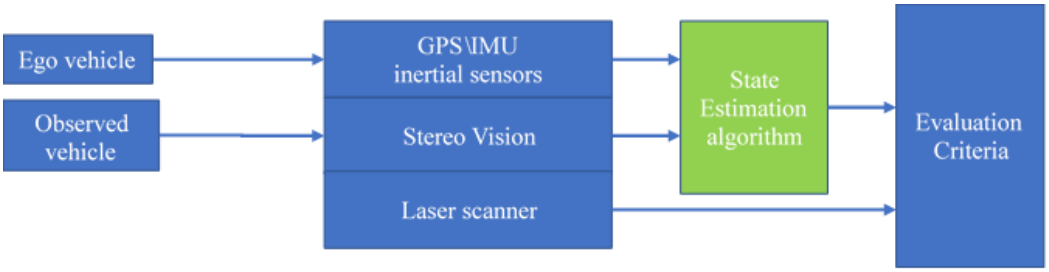

Figure (2.1): Diagram of the interacted components of the system

The system architecture is demonstrated in Figure (2.1), the system consists of a moving ego-vehicle precepted its own motion by GPS/IMU inertial sensors and equipped by stereo vision system and laser scanner. Figure (2.2) shows KITTI ego-vehicle; VW Passat station wagon as recording platform, it recognizes the motion of the observed vehicle within the stereo vision sensor field of view distant less than 120 meters that is the laser scanner range. The state estimation algorithm is 1st order extended Kalman filter provided by the ego motion data from the inertial sensors, and the observed vehicle motion from the stereo vision measurements. The evaluation criteria of the estimation algorithms performance and efficiency is the root mean square RMS of the estimation error referred to the trusted data that are the relative position and heading of the observed vehicle measured by the laser scanner. In the case of synthesized data that provides all the true states so we compute the RMS for all the states for evaluation purpose.

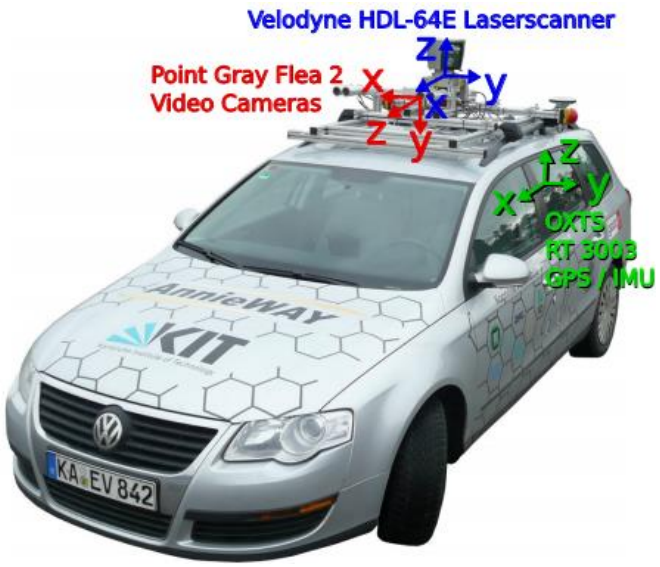

Figure (2.2): Ego-vehicle of KITTI dataset equipped by the sensory package

KITTI stereo vision system specifications are summarized in Table (2.2), it consists of two high resolution (1.4 Megapixels) grayscale cameras (FL2-14S3M-C) provided by 4mm Edmund Optics lenses with opening angle of 90deg, vertical opening angle of

35deg, while the rotating 3D laser scanner (Velodyne) is 10 Hz, 0.09 deg angular resolution, 120m range, 2 cm distance accuracy, 360 deg horizontal, 26.8 deg vertical field of view.

Table (2.2): KITTI dataset stereo system specifications

Image resolution	1382*512 pixels
# cars per image	up to 15
# pedestrians per image	up to 30
Shutter speed	2 ms
Frame rate	10 FPS
Stereo baseline	54 cm

Figure (**2.3**) shows the point cloud of 3D laser scanner projected on the corresponding stereo image. KITTI inertial and GPS navigation system is OXTS RT3003, 6 axes, 100 Hz, L1/L2 RTK, resolution 0.02m / 0.1°, localization system which combines GPS, GLONASS, an IMU and RTK correction signals. The cameras, laser scanner and localization system were calibrated and synchronized, providing accurate ground truth. (Geiger et. al. 2013).

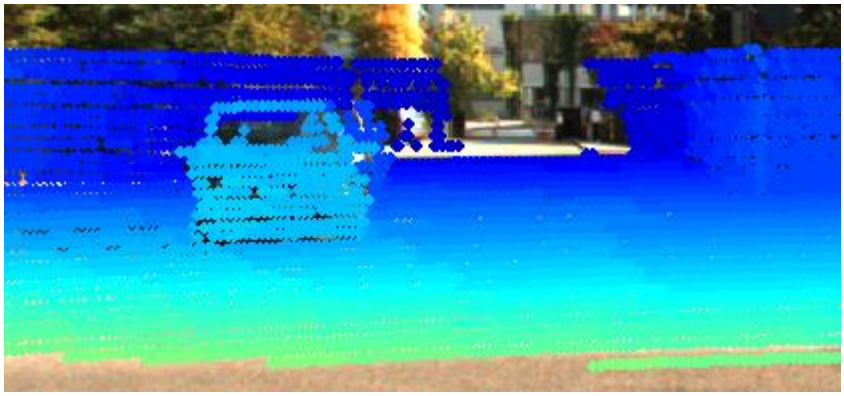

Figure (2.3): KITTI 3D laser scanner point cloud projected on its corresponding image

2.3 Vision System Model

2.3.1 Pinhole Camera Model

We start with the most specialized and simplest camera model, which is the basic pinhole camera. The geometry of pinhole camera is shown in Figure (**2.4**). The center of projection is called *the camera center* or *the optical center* **C**. The line from the camera center perpendicular to the image plane is called *the principal axis* or *principal ray* of the camera ***z***-axis, and the point where the principal axis meets the image plane is called *the*

principal point **P** and the length from the optical center to the principal point is called the focal length f.

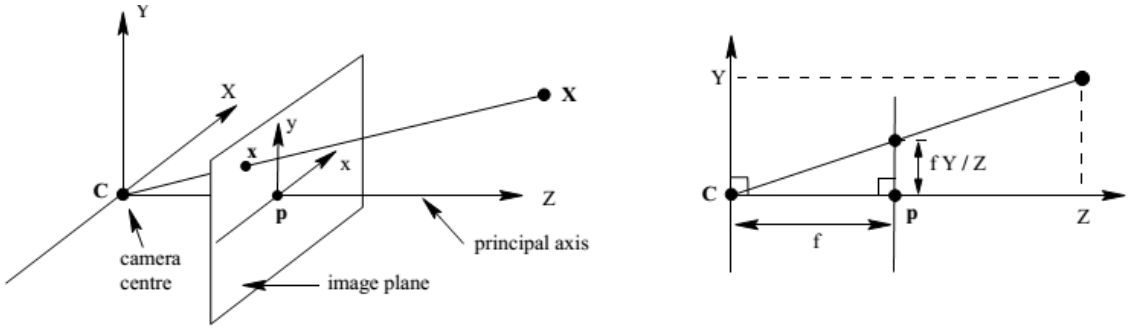

Figure (2.4): Pinhole Camera Geometry & the vertical triangulation of the pinhole Camera (Hartley et. al. 2004).

The central projection mapping from world point to image coordinates is described by the following equation (Richard Hartley, Andrew Zisserman, 2004)

$$\begin{bmatrix} u \\ w \end{bmatrix} = \begin{bmatrix} \frac{f_x . x}{z} + x_0 \\ \frac{f_y . y}{z} + y_0 \end{bmatrix} \qquad (2.1)$$

Where f_x, f_y represent the focal length of the camera in terms of pixel dimensions in the x and y direction respectively. (u, w) represent the projected point on the image plane x and y axes respectively in terms of pixel dimensions. (x, y, z) represents the world point position in the coordinate frame of the camera as shown in Figure (2.4). (x_0, y_0) are the coordinates of the principal point in terms of pixel dimensions in Figure (2.5).

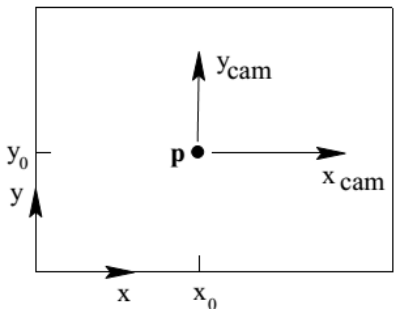

Figure (2.5): Image x_y and camera xcam_ycam coordinate systems (Hartley et. al. 2004).

Note that under the assumption of flat road, we considered that the observed vehicle in the same altitude of the ego vehicle, so we neglect the vertical projection (w).

2.3.2 Stereoscopic Vision Model

The stereoscopic system consists of either one optical sensor which can be moved so that its relative positions at different times are known, or two (or more) optical sensors always maintaining the same known position with respect to each other. If more than one sensor

is utilized, it will be assumed that they are all identical, and the effect of each optical sensor (e.g., a camera) will be modeled as though it were an ideal pinhole camera (Nicolas Alvertos, 1989). Figure (2.6) shows the bird view of the lateral stereoscopic model where the two cameras are perfectly parallel have the same focal length f_x and separated by a translation in the x-direction between the left and right camera optical centers, this translation is called baseline *b*. In Figure (2.6) the *x-z* axis of the stereo cameras corresponds to the ego longitudinal, lateral axis respectively. Given a real-world point (*X,Y,Z*) in frame coordinates originated at the left camera optical center, *ul, ur* are the horizontal projection of (*X,Y,Z*) on the left and right camera image planes respectively as demonstrated in Figure (2.6), Applying equations (2.1) to get the horizontal projections:

$$ul = \frac{f_x . x}{z} + x_0 \qquad (2.2)$$

$$ur = \frac{f_x . (x - b)}{z} + x_0 \qquad (2.3)$$

The distance between those two projected points is known as "disparity",

$$d = ul - ur \qquad (2.4)$$

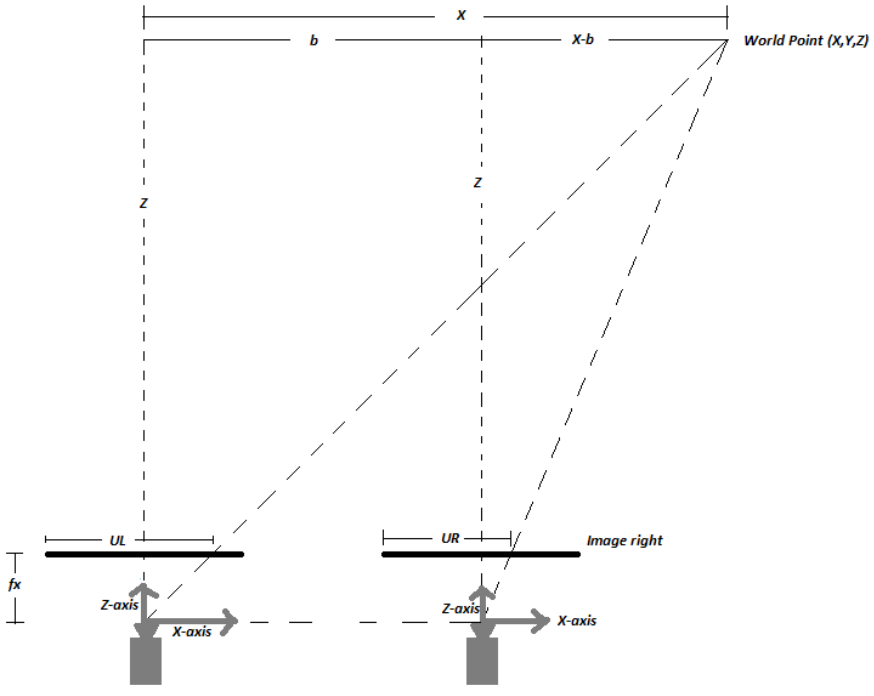

Figure (2.6): The lateral stereoscopic disparity and depth

Substituting equations (2.2), (2.3) in equation (2.4) we get

$$d = \frac{f_x . b}{z} \qquad (2.5)$$

For known disparity, it's possible to calculate the depth of the projected point:

$$z = \frac{f_x . b}{d} \qquad (2.6)$$

Substituting equation (2.6) in (2.2), and isolating x in the left side we get

$$x = \frac{(ul - x_0).z}{f_x} = \frac{(ul - x_0).b}{d} \qquad (2.7)$$

Equations (2.2,4) forms the nonlinear measurement model while equations (2.6,7) forms the linear measurement model of the stereo vision.

2.4 Dynamic System Modeling

The development of appropriate dynamic model that accurately describe the evolution of the tracked object status and efficiently handles the uncertainty of the excitation and disturbances is the most challenging issue in tracking problems. There are many models that were developed in the last decades for on-road vehicles. This thesis deals with the curvilinear models that theoretically could describe the motion of road vehicles very accurately, errors may result from highly dynamic effects such as drifting or skidding. While models which are able to cope with such effects do exist like the realistic model proposed in (R. Pepy, A. Lambert, and H. Mounier, 2006), they will not be considered here for two reasons, most Intelligent Transportation Systems applications (ITS) are designed for scenarios with non-critical dynamics. Furthermore, the information which are necessary for estimating the additional parameters (e.g. slip from every tire, lateral acceleration) are not observable by exteroceptive sensors. Thus, such models can be used for estimating the ego vehicle's motion only (Robin Schubert, Eric Richter, Gerd Wanielik, 2012).

2.4.1 Simplified Bicycle Model

The vehicle driving dynamics under normal conditions are approximated by a single-lane model of the Ackermann Steering Geometry in Figure (2.7), where the left and right wheels are merged at the axle's center, yielding two-wheel model steering geometry usually referred to as bicycle model. (D. Schramm, M. Hiller, R. Bardini, 2014).

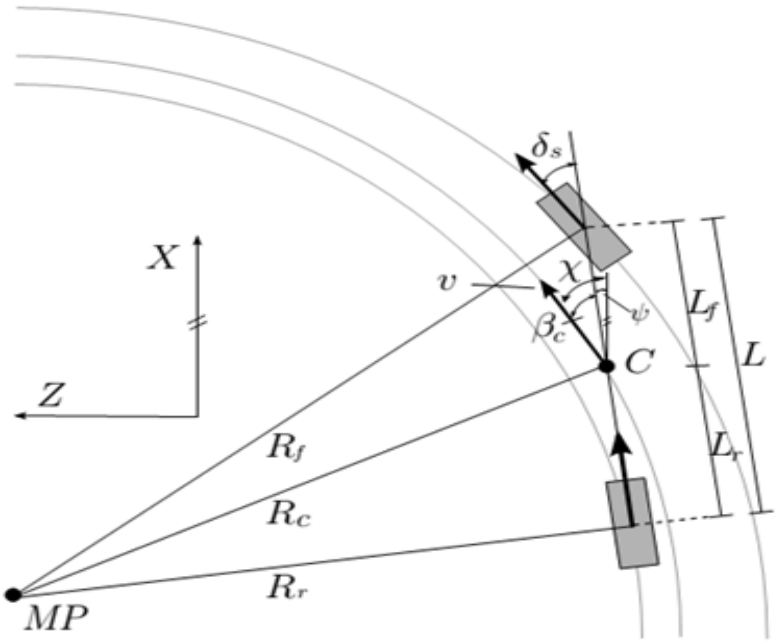

Figure (2.7): Ackermann Steering Geometry simplified bicycle model (Barth, 2010)

The vehicle moving direction χ with respect to a global world coordinate system is composed of the yaw angle ψ, and the side slip angle β_C, as

$$\chi = \psi + \beta_C \qquad (2.8)$$

The x-z plane translation of the center of mass C whose position is (x_C, z_C) with respect to a static world coordinate system results from the following observations

$$\frac{dx_C}{ds} = cos(\psi + \beta_C), \qquad \frac{dz_C}{ds} = \sin(\psi + \beta_C) \qquad (2.9)$$

with velocity $v = \mathrm{ds/dt}$, where s represents the arc length,

$$\frac{dx_C}{ds} = \frac{dX_C}{dt}.\frac{dt}{ds} = \frac{\dot{X}_C}{v}, \qquad \frac{dz_C}{ds} = \frac{dZ_C}{dt}.\frac{dt}{ds} = \frac{\dot{Z}_C}{v} \qquad (2.10)$$

$$\dot{x}_C = v\cos(\psi + \beta_C), \qquad \dot{z}_C = v\sin(\psi + \beta_C) \qquad (2.11)$$

At normal conditions, the side slip angle β_C becomes negligible at the center of the rear wheel.

$$\dot{X}_r = v\cos(\psi), \qquad \dot{Z}_r = v\sin(\psi) \qquad (2.12)$$

equation (2.12) represents the principal simplified on-road vehicles motion that form the basic background for all bicycle model based advanced variants, so now we are ready to develop two of those variants called Constant turn rate and constant polar velocity model (CTRPV) Constant turn rate and constant acceleration model (CTRA), through the following systematic procedure:

1. Statement the motion assumptions interpreted into differential equations and

deriving the continuous-time state space model for static ego vehicle.

2. Discretizing the state space model using the impulse discretization and zero order hold (ZOH) discretization.
3. Augmenting the ego vehicle motion to get the discrete-time state space model for moving ego attached coordinate frame system.

The dynamic models CTRPV, CTRA would be developed for the observed vehicle that is moving in the horizontal plane X-Z in Figure (2.8).

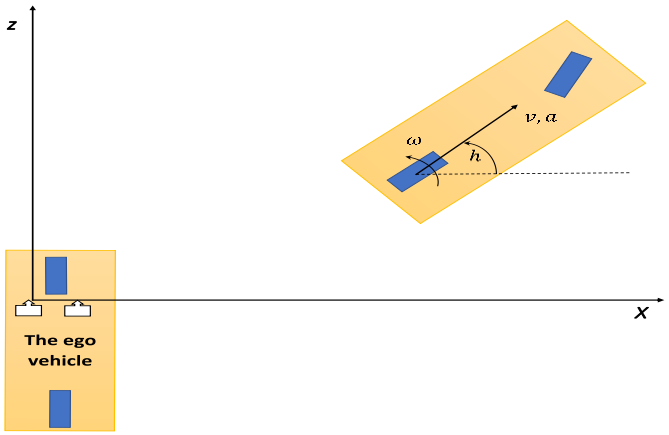

Figure (2.8): The observed vehicle in the coordinate frame of the ego-vehicle

Consider a coordinate frame system that is originated at the optical center of the left camera such that the z-axis is in the direction of the ego vehicle forward direction, the x-axis is in the right direction of the ego vehicle.

2.4.2 CTRPV: Constant turn rate and constant polar velocity model

the state vector of CT-CTRPV and DT-CTRPV models consists of the relative position, velocity, heading angle and heading turn rate of the observed vehicle as following:

$$X_{CTRPV} = [x, z, v, h, \omega]^T$$

2.4.2.1 The continuous-time state space model

In CTRPV modeling its assumed that the object is moving at constant polar velocity v and constant turn rate ω perturbed by zero mean gaussian white noises a, α respectively

$$\dot{v} = a = q_a(t) \qquad (2.13)$$

$$\dot{\omega} = \alpha = q_\alpha(t) \qquad (2.14)$$

So, by coupling the differential equations (2.12-14) and seperating exitation inputs $a\ and\ \alpha$ from the state transition function, we get continuous-time state space model of the CTRPV:

$$\dot{X}_{CTRPV}(t) = \begin{bmatrix} \dot{x} \\ \dot{z} \\ \dot{v} \\ \dot{h} \\ \dot{\omega} \end{bmatrix} = f\left(X_{CTRPV}(t)\right) + q(t) = \begin{bmatrix} v\cos(h) \\ v\sin(h) \\ 0 \\ \omega \\ 0 \end{bmatrix} + \begin{bmatrix} 0 \\ 0 \\ a \\ 0 \\ \alpha \end{bmatrix} \qquad (2.15)$$

2.4.2.2 The discrete-time state space model

CT- CTRPV model could by discretized by the following exact solution

$$X_{CTRPV}(t+T) = X_{CTRPV}(t) + \int_{t}^{t+T} \left(f\left(X_{CTRPV}(\tau)\right) + q(\tau)\right) d\tau \qquad (2.16)$$

where T is the sample time period from $k\ to\ k+1$ instants (F. Gustafsson and A. Isaksson, 1996), the solution could be rewritten as

$$X_{k+1} = f_{CTRPV}(X_k) + G_{CTRPV}(X_k) q_k \qquad (2.17)$$

where k denotes sampling instants, q_k is the process model stationary zero mean Gaussian noise, $f_{CTRPV}: R^5 \rightarrow R^5$ is the CTRPV model nonlinear state transition vector function

$$f_{CTRPV} = \begin{bmatrix} x + \frac{2v}{\omega}\sin\left(\frac{\omega T}{2}\right)\cos\left(h + \frac{\omega T}{2}\right) \\ z + \frac{2v}{\omega}\sin\left(\frac{\omega T}{2}\right)\sin\left(h + \frac{\omega T}{2}\right) \\ v \\ h + \omega T \\ \omega \end{bmatrix} \qquad (2.18)$$

$G_{CTRPV}: R^{5*2}$ is the affine model noise matrix formulated as input matrix, by zero-order-hold and impulse input discretizing we get two variant input matrices,

$$G_{z.o.h.}^{CTRPV} = \begin{bmatrix} 0 & 0 \\ 0 & 0 \\ T & 0 \\ 0 & 0 \\ 0 & T \end{bmatrix}_k, \quad G_{imp.}^{CTRPV} = \begin{bmatrix} \frac{T^2}{2}\cos(h) & 0 \\ \frac{T^2}{2}\sin(h) & 0 \\ T & 0 \\ 0 & \frac{T^2}{2} \\ 0 & T \end{bmatrix} \qquad (2.19)$$

the characteristics of the process noise

$$E[q_k^T] = E[q_a q_\alpha] = [0\ 0] \qquad (2.20)$$

$$Q = cov[q_k^T] = cov[q_a q_\alpha]^T = DIAG[\sigma_a^2 \sigma_\alpha^2]^T \qquad (2.21)$$

Such that σ_a^2 is the variance of the forward acceleration by (m/s^2), σ_α^2 is the variance of the turn acceleration by (rad/s^2). (Robin Schubert, Eric Richter, Gerd Wanielik, 2012)
Note that $E[\,]$ denotes for the expected value mathematical operator or the mean, $cov[\,]$ denotes for the covariance mathematical operator, $DIAG[\,]$ denotes for the diagonal matrix mathematical operator, those operators would be used in the rest of the thesis.

2.4.3 CTRA: Constant turn rate and constant acceleration model

the state vector of CT-CTRA and DT-CTRA models consists of the relative position, velocity, acceleration, heading angle and heading turn rate of the observed vehicle as following:

$$X_{CTRA} = [x, z, v, a, h, \omega]^T$$

2.4.3.1 The continuous-time state space model

We assume that the object is moving at constant polar acceleration perturbed by zero mean Gaussian white noise, J, and constant turn rate ω perturbed by zero mean Gaussian white noise, α,

$$\dot{a} = J = q_J(t) \qquad (2.22)$$

$$\dot{\omega} = \alpha = q_\alpha(t) \qquad (2.23)$$

So, by coupling the differential equations (2.12,22,23), and seperating of exitation inputs J, α from the state transition function we get CT state space model of the CTRA
we get:

$$\dot{X}_{CTRA}(t) = \begin{bmatrix} \dot{x} \\ \dot{z} \\ \dot{v} \\ \dot{a} \\ \dot{h} \\ \dot{\omega} \end{bmatrix} = f\big(X_{CTRA}(t)\big) + q(t) = \begin{bmatrix} v\cos(h) \\ v\sin(h) \\ \mathrm{a} \\ 0 \\ \omega \\ 0 \end{bmatrix} + \begin{bmatrix} 0 \\ 0 \\ 0 \\ J \\ 0 \\ \alpha \end{bmatrix} \qquad (2.24)$$

2.4.3.2 The discrete-time state space model

Similar to the CTRPV, the discretization model of CTRA is

$$X_{k+1} = f_{CTRA}(X_k) + G_{CTRA}(X_k)q_k \qquad (2.25)$$

where k denotes sampling instants, q_k is the process model stationary zero mean Gaussian noise, $f_{CTRA}: R^6 \rightarrow R^6$ is the CTRA model nonlinear state transition vector function

$$f_{CTRA} = \begin{bmatrix} x + \frac{1}{\omega^2}[(v\omega + a\omega T)sin(h + \omega T) + a * cos(h + \omega T) - v\omega sin(h) - a * \cos(h)] \\ z + \frac{1}{\omega^2}[(-v\omega - a\omega T)cos(h + \omega T) + a * sin(h + \omega T) + v\omega cos(h) - a * \sin(h)] \\ v + aT \\ a \\ h + \omega T \\ \omega \end{bmatrix} \quad (2.26)$$

$G_{CTRA}: R^{6*2}$ is the affine model noise matrix formulated as input matrix, by zero-order-hold and impulse input discretizing we get two variant input matrices,

$$G_{zoh}^{CTRA} = \begin{bmatrix} 0 & 0 \\ 0 & 0 \\ 0 & 0 \\ T & 0 \\ 0 & 0 \\ 0 & T \end{bmatrix}, \quad G_{imp}^{CTRA} = \begin{bmatrix} \frac{T^3}{6}\cos(h) & 0 \\ \frac{T^3}{6}\sin(h) & 0 \\ \frac{T^2}{2} & 0 \\ T & 0 \\ 0 & \frac{T^2}{2} \\ 0 & T \end{bmatrix} \quad (2.27)$$

the process noise is characterized by σ_J^2 the variance of the forward jerk by (m/s^3), σ_α^2 the variance of the turn acceleration by (rad/s^2). (Schubert et. al. 2012)

$$E[q_k^T] = E[q_J q_\alpha] = [0\ 0] \quad (2.28)$$

$$Q = cov[q_k^T] = cov[q_J q_\alpha]^T = DIAG[\sigma_J^2 \sigma_\alpha^2]^T \quad (2.29)$$

2.4.4 Th ego vehicle motion Augmentation

Now, the system dynamic model for moving ego vehicle would be derived through the augmentation for the motion of the ego-vehicle through two consecutive stereo sequences. First note that equations (2.17-19,2.25-27) infers the x, z, h at $k+1$instant of the observed vehicle in coordinate frame of the ego at k instant. If we know the ego-motion from k to $k+1$ time instants, as translational displacements $\Delta x_e, \Delta z_e$, and rotational displacements $\Delta h_e$with respect to coordinate frame of the ego at k instant as shown in Figure (2.9) we simply could derive the x, z, h at $k+1$ instant of the observed vehicle in coordinate frame of the ego at k+1 instant, by applying the translational displacement $\Delta x_e, \Delta z_e$ and we get the translated observed vehicle position

$$\begin{bmatrix} x_{k+1} \\ z_{k+1} \end{bmatrix}_{translated} = \begin{bmatrix} x_{k+1} - \Delta x_e \\ z_{k+1} - \Delta z_e \end{bmatrix} \quad (2.30)$$

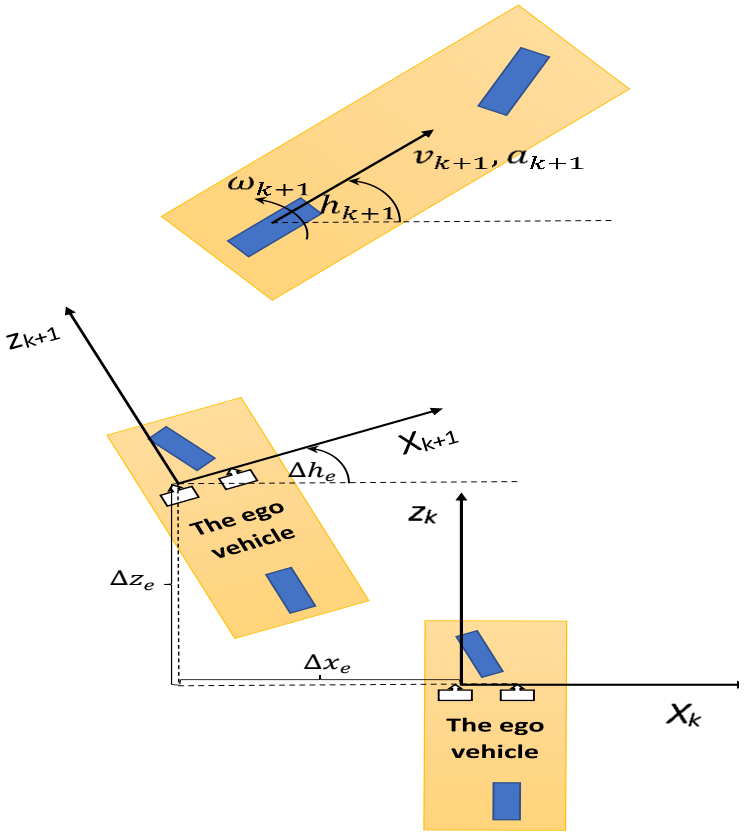

Figure (2.9): The translational and rotational motion of the ego vehicle

Then, by applying the rotational displacement Δh_e transformation, we get the rotated observed vehicle position and heading.

$$\begin{bmatrix} x_{k+1} \\ z_{k+1} \end{bmatrix}_{augmented} = \begin{bmatrix} \cos(\Delta h_e) & \sin(\Delta h_e) \\ -\sin(\Delta h_e) & \cos(\Delta h_e) \end{bmatrix} \begin{bmatrix} x_{k+1} \\ z_{k+1} \end{bmatrix}_{translated} \quad (2.31)$$

$$(h_{k+1})_{augmented} = h_{k+1} - \Delta h_e \quad (2.32)$$

In KITTI dataset ego-motion information $\Delta h_e, \Delta x_e, \Delta z_e$ is incorporated from inertial navigation system.

Chapter 3

System Filter Design

and Implementation

Chapter 3
System Filter Design and Implementation

Filtering basically means the process of filtering out the noise in the measurements and providing an optimal estimate for the state given the observed measurements and the assumptions made about the dynamic system (Jouni Hartikainen, Arno Solin, and Simo Särkkä, 2011), the Kalman filter (KF) is considered the basic method for recursively solving the linear state space estimation problems. For nonlinear dynamic system model or nonlinear measurement model or both are nonlinear the Extended Kalman filter (EKF) which is the classical extension of KF is often used.

EKF has a few serious drawbacks, which should be kept in mind when it's used:

1. the linear and quadratic transformations produce reliable results only when the error propagation can be well approximated by a linear or a quadratic function. If this condition is not met, the performance of the filter can be extremely poor. At worst, its estimates can diverge altogether.
2. The Jacobian matrices (and Hessian matrices with second order filters) need to exist so that the transformation can be applied. However, there are cases, where this isn't true. For example, the system might be jump-linear, in which the parameters can change abruptly.

In many cases the calculation of Jacobian and Hessian matrices can be very difficult process, and it's also prone to human errors (both derivation and programming). These errors are usually very hard to debug, as it's hard to see which parts of the system produces the errors by looking at the estimates, especially as usually we don't know which kind of performance we should expect.

In this chapter we review a systematic framework of the 1st order Extended Kalman Filter (EKF) then the equations of vehicle motion and stereo vision in chapter 2 are reformulated compatibly with the EKF framework.

3.1 Extended Kalman Filter

The general model of the discrete time nonlinear dynamic system with nonlinear measurement mode is:

$$x_{k+1} = f(x_k, k) + Gq_k \qquad (3.1)$$

$$y_k = h(x_k) + r_k \qquad (3.2)$$

where $x_{k+1} \in R^n$ is the state, $y_k \in R^m$ is the measurement, $q_k \sim N(0, Q_k)$ is the process noise, $r_k \sim N(0, R_k)$ is the measurement noise on the time step k. f is the nonlinear transition function of the dynamic model, G is the noise matrix, h is the measurement model function. the prior distribution for the state is $x_0 \sim N(\hat{x}_0, P_0)$, where parameters $\hat{x}_0, P_0$ are set using the information known about the system under the study Like KF, also the first order EKF is separated to two steps: the prediction step, where the next state of the system is predicted given the previous measurements, and the update step, where the current state of the system is estimated given the measurement at that time step. Figure (2.10) presents the flowchart of 1st order EKF for one cycle

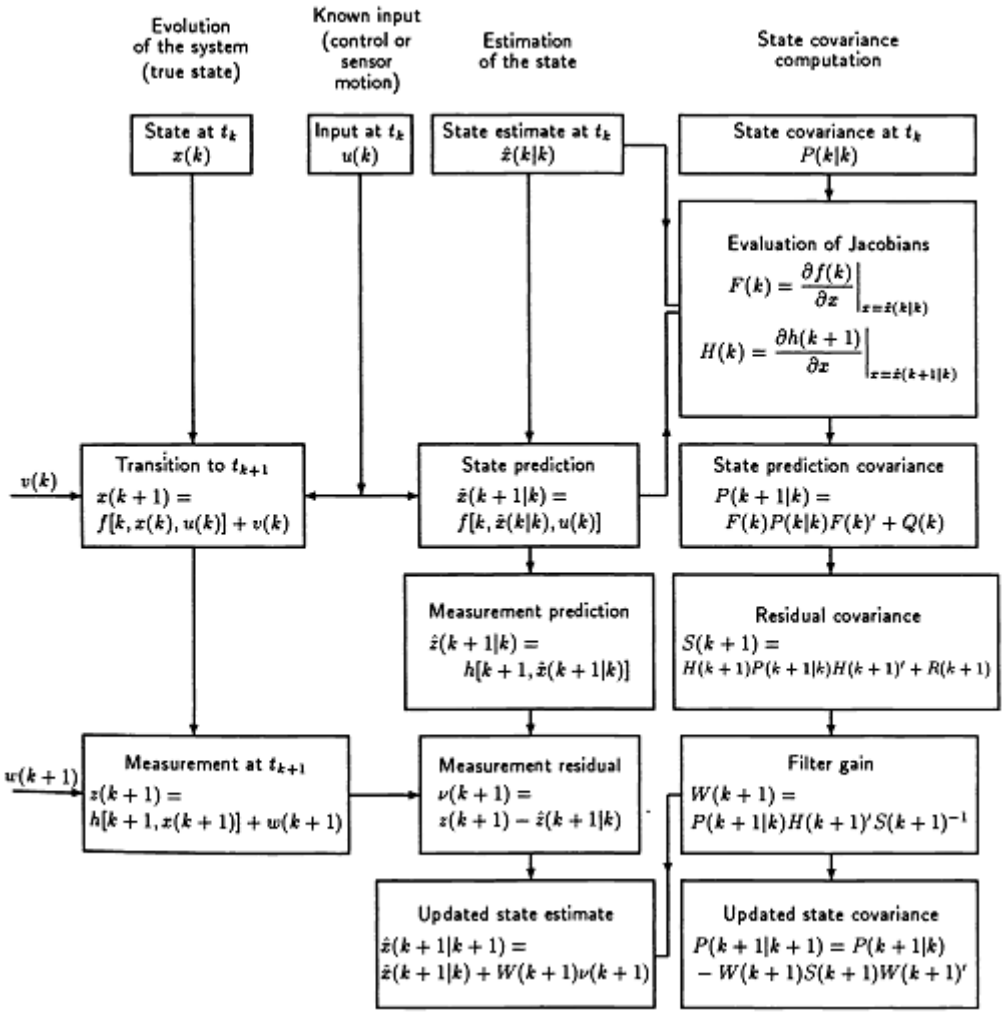

Figure (2.10): Flowchart of 1st order EKF (one cycle) (Bar-Shalom, Y., Li, X.-R., and Kirubarajan, T., 2001)

The two steps of KF is formatted as the following equations, (Särkkä, 2007);

Prediction step:

Predicted (*a priori*) state estimate $$\hat{x}_{k+1|k} = f(\hat{x}_{k|k}, k) \quad (3.3)$$

Predicted covariance estimate $$P_{k+1|k} = F_x(\hat{x}_{k|k}, k) P_{k|k} F_x^T(\hat{x}_{k|k}, k) + G Q_k G^T \quad (3.4)$$

Update step:

Innovation or measurement pre-fit residual $$\tilde{y}_k = y_k - h\left(\hat{x}_{k+1|k}, k+1\right) \quad (3.5)$$

Innovation (or pre-fit residual) covariance $$S_{k=} H_x P_{k+1|k} H_x^T + R_k \quad (3.6)$$

Optimal Kalman gain $$K_{k=} P_{k+1|k} H_x^T S_k^{-1} \quad (3.7)$$

Updated (*a posteriori*) state estimate $$\hat{x}_{k+1|k+1} = \hat{x}_{k+1|k} + K_k \tilde{y}_k \quad (3.8)$$

Updated (*a posteriori*) estimate covariance $$P_{k+1|k+1} = (I - K_k H_x) P_{k+1|k} \quad (3.9)$$

Measurement post-fit residual $$\tilde{y}_k = y_k - H_x \hat{x}_{k+1|k+1} \quad (3.10)$$

3.2 Model Equations

Now we would reformulate the equations of vehicle motion in the form of equation (3.1), by combining the equations (2.17-21) and (2.31) we get the augmented CTRPV model:

$$\begin{bmatrix} x \\ z \\ v \\ h \\ \omega \end{bmatrix}_{k+1} = \begin{bmatrix} \cos(\Delta h_e)\left[x + \frac{2v}{\omega}\sin\left(\frac{\omega T}{2}\right)\cos\left(h + \frac{\omega T}{2}\right) - \Delta x_e\right] + \sin(\Delta h_e)\left[z + \frac{2v}{\omega}\sin\left(\frac{\omega T}{2}\right)\sin\left(h + \frac{\omega T}{2}\right) - \Delta z_e\right] \\ -\sin(\Delta h_e)\left[x + \frac{2v}{\omega}\sin\left(\frac{\omega T}{2}\right)\cos\left(h + \frac{\omega T}{2}\right) - \Delta x_e\right] + \cos(\Delta h_e)\left[z + \frac{2v}{\omega}\sin\left(\frac{\omega T}{2}\right)\sin\left(h + \frac{\omega T}{2}\right) - \Delta z_e\right] \\ v \\ h + \omega T - \Delta h_e \\ \omega \end{bmatrix}_k$$

$$+ \left(\begin{bmatrix} \frac{T^2}{2}\cos(h) & 0 \\ \frac{T^2}{2}\sin(h) & 0 \\ T & 0 \\ 0 & \frac{T^2}{2} \\ 0 & T \end{bmatrix}_k \boldsymbol{OR} \begin{bmatrix} 0 & 0 \\ 0 & 0 \\ T & 0 \\ 0 & 0 \\ 0 & T \end{bmatrix}_k \right) \begin{bmatrix} q_a \\ q_\alpha \end{bmatrix}_k \quad (3.11)$$

and combining the equations (2.25-29) and (2.31) we get the augmented CTRA model:

$$\begin{bmatrix} x \\ z \\ v \\ a \\ h \\ \omega \end{bmatrix}_{k+1} = \begin{bmatrix} \cos(\Delta h_e) * x_{translated} + \sin(\Delta h_e) * x_{translated} \\ -\sin(\Delta h_e) * z_{translated} + \cos(\Delta h_e) * z_{translated} \\ v + aT \\ a \\ h + \omega T - \Delta h_e \\ \omega \end{bmatrix}_k$$

$$+ \left(\begin{bmatrix} \frac{T^3}{6}\cos(h) & 0 \\ \frac{T^3}{6}\sin(h) & 0 \\ \frac{T^2}{2} & 0 \\ T & 0 \\ 0 & \frac{T^2}{2} \\ 0 & T \end{bmatrix} \mathbf{OR} \begin{bmatrix} 0 & 0 \\ 0 & 0 \\ 0 & 0 \\ T & 0 \\ 0 & 0 \\ 0 & T \end{bmatrix} \right) \begin{bmatrix} q_J \\ q_\alpha \end{bmatrix}_k \quad (3.12)$$

where

$$x_{translated} = x + \frac{1}{\omega^2}[(v\omega + a\omega T)sin(h + \omega T) + a * cos(h + \omega T) - v\omega sin(h) - a * \cos(h)] - \Delta x_e$$

$$z_{translated} = z + \frac{1}{\omega^2}[(-v\omega - a\omega T)cos(h + \omega T) + a * sin(h + \omega T) + v\omega cos(h) - a * \sin(h)] - \Delta z_e$$

Such that for both models we have two input matrices (G) according to the discretization (ZOH and impulse respectively). In the prediction step the Jacobean of the transition function is required to be computed, So the Jacobean of the CTRPV augmented model is:

$$F_X = \left|\frac{\partial X_{k+1}}{\partial X_k}\right| = \begin{bmatrix} \mathrm{c}(\Delta h_e) & \mathrm{s}(\Delta h_e) & A_{1,3} & A_{1,4} & A_{1,5} \\ -\mathrm{s}(\Delta h_e) & \mathrm{c}(\Delta h_e) & A_{2,3} & A_{2,4} & A_{2,5} \\ 0 & 0 & 1 & 0 & 0 \\ 0 & 0 & 0 & 1 & T \\ 0 & 0 & 0 & 0 & 1 \end{bmatrix} \quad (3.13)$$

Where

$$A_{1,3} = \mathrm{c}(\Delta h_e)\frac{\partial x_{k+1}}{\partial v_k} + \mathrm{s}(\Delta h_e) * \frac{\partial z_{k+1}}{\partial v_k}, \qquad A_{2,3} = -\mathrm{s}(\Delta h_e)\frac{\partial x_{k+1}}{\partial v_k} + \mathrm{c}(\Delta h_e) * \frac{\partial z_{k+1}}{\partial v_k}$$

$$\frac{\partial x_{k+1}}{\partial v_k} = \frac{2}{\omega}\mathrm{s}\left(\frac{\omega T}{2}\right)\mathrm{c}\left(h + \frac{\omega T}{2}\right), \qquad \frac{\partial z_{k+1}}{\partial v_k} = \frac{2}{\omega}\mathrm{s}\left(\frac{\omega T}{2}\right)\mathrm{s}\left(h + \frac{\omega T}{2}\right)$$

$$A_{1,4} = \mathrm{c}(\Delta h_e)\frac{\partial x_{k+1}}{\partial h_k} + \mathrm{s}(\Delta h_e) * \frac{\partial z_{k+1}}{\partial h_k}, \; A_{2,4} = -\mathrm{s}(\Delta h_e)\frac{\partial x_{k+1}}{\partial h_k} + \mathrm{c}(\Delta h_e) * \frac{\partial z_{k+1}}{\partial h_k}$$

$$\frac{\partial x_{k+1}}{\partial h_k} = \frac{-2v}{\omega}\mathrm{s}\left(\frac{\omega T}{2}\right)\mathrm{s}\left(h + \frac{\omega T}{2}\right), \qquad \frac{\partial z_{k+1}}{\partial h_k} = \frac{2v}{\omega}\mathrm{s}\left(\frac{\omega T}{2}\right)\mathrm{c}\left(h + \frac{\omega T}{2}\right)$$

$$A_{1,5} = \mathrm{c}(\Delta h_e)\frac{\partial x_{k+1}}{\partial \omega_k} + \mathrm{s}(\Delta h_e) * \frac{\partial z_{k+1}}{\partial \omega}, \qquad A_{2,5} = -\mathrm{s}(\Delta h_e)\frac{\partial x_{k+1}}{\partial \omega_k} + \mathrm{c}(\Delta h_e) * \frac{\partial z_{k+1}}{\partial \omega_k}$$

$$\frac{\partial x_{k+1}}{\partial \omega_k} = \frac{vT}{\omega}c\left(\frac{\omega T}{2}\right)\mathrm{c}\left(h + \frac{\omega T}{2}\right) - \frac{2v}{\omega^2}s\left(\frac{\omega T}{2}\right)\mathrm{c}\left(h + \frac{\omega T}{2}\right) - \frac{vT}{\omega}s\left(\frac{\omega T}{2}\right)\mathrm{s}\left(h + \frac{\omega T}{2}\right)$$
$$= \left[cos\left(h + \frac{\omega T}{2}\right) * \left[\frac{vT}{\omega}\cos\left(\frac{\omega T}{2}\right) - \frac{2v}{\omega^2}\sin\left(\frac{\omega T}{2}\right)\right]\right] - \left[\frac{vT}{\omega}\sin\left(\frac{\omega T}{2}\right)\sin\left(h + \frac{\omega T}{2}\right)\right]$$

$$\frac{\partial z_{k+1}}{\partial \omega_k} = \frac{vT}{\omega}c\left(\frac{\omega T}{2}\right)\mathrm{s}\left(h + \frac{\omega T}{2}\right) - \frac{2v}{\omega^2}s\left(\frac{\omega T}{2}\right)\mathrm{s}\left(h + \frac{\omega T}{2}\right) + \frac{vT}{\omega}s\left(\frac{\omega T}{2}\right)\mathrm{c}\left(h + \frac{\omega T}{2}\right)$$
$$= \left[sin\left(h + \frac{\omega T}{2}\right) * \left[\frac{vT}{\omega}\cos\left(\frac{\omega T}{2}\right) - \frac{2v}{\omega^2}\sin\left(\frac{\omega T}{2}\right)\right]\right] + \left[\frac{vT}{\omega}\sin\left(\frac{\omega T}{2}\right)\cos\left(h + \frac{\omega T}{2}\right)\right]$$

The analytical expression for the Jacobean of the CTRA augmented model were obtained using the MATLAB Symbolic Math toolbox as shown in Analytic_CTRA_JAC.m in Appendix B. The expression is very complicated and long to be written textually in the thesis.

3.2.1 Numerical aspects

In the context of implementing the prediction step of the filter, the transition functions f_{CTRPV}, f_{CTRA} and their Jacobeans F_{CTRPV_X}, F_{CTRA_X} where implemented as MATLAB functions, since they contain division by ω terms which could cause filter instability in

the case of division by zero numerical error at zero ω those terms are substituted by its limit as ω tends to zero, for CTRPV transition function :

$$\lim_{\omega\to 0}\left\{\frac{2v}{\omega}\sin\left(\frac{\omega T}{2}\right)\cos(h+\frac{\omega T}{2})\right\} = vTcos(h) \qquad (3.14)$$

$$\lim_{\omega\to 0}\left\{\frac{2v}{\omega}\sin\left(\frac{\omega T}{2}\right)\sin(h+\frac{\omega T}{2})\right\} = vTsin(h) \qquad (3.15)$$

for CTRA transition function :

$$\lim_{\omega\to 0}\left\{\frac{1}{\omega^2}[(v\omega + a\omega T)sin(h+\omega T) + a*cos(h+\omega T) - v\omega sin(h) - a*\cos(h)\right\}$$
$$= (2vT + aT^2)*cos(h)/2 \qquad (3.16)$$

$$\boldsymbol{\lim_{\omega\to 0}\left\{\frac{1}{\omega^2}[(-v\omega - a\omega T)cos(h+\omega T) + a*sin(h+\omega T) + v\omega cos(h) - a*sin(h)\right\}}$$
$$\boldsymbol{= (2vT + aT^2)*sin(h)/2} \qquad (3.17)$$

And for the Jacobean of CTRPV transition function:

$$\lim_{\omega\to 0} A_{1,3} = Tcos(\Delta h_e - h), \quad \lim_{\omega\to 0} A_{1,4} = vTsin(\Delta h_e - h), \quad \lim_{\omega\to 0} A_{1,5} = \frac{vT^2 sin(\Delta h_e - h)}{2} \qquad (3.18)$$

$$\lim_{\omega\to 0} A_{2,3} = -Tsin(\Delta h_e - h), \quad \lim_{\omega\to 0} A_{2,4} = vTcos(\Delta h_e - h), \quad \lim_{\omega\to 0} A_{2,5} = \frac{vT^2 cos(\Delta h_e - h)}{2} \qquad (3.19)$$

Equations 3.11-19 are implemented in CTRPV.m, CTRA.m and JAC_CTRPV.m files. The numerical Jacobian for CTRA based on the following numerical derivative:

$$\frac{\partial x_{k+1}}{\partial \omega_k} = \frac{x_{k+1}(x_k, z_k, v_k, a_k, h_k, \omega_k + \Delta\omega) - x_{k+1}(x_k, z_k, v_k, a_k, h_k, \omega_k)}{\Delta\omega} : \Delta\omega \text{ is small enough}$$

is also implemented as function handle in num_JAC_CTRA.m file, see appendix B for all MATLAB files.

3.3 Measurement Equations

3.3.1 Nonlinear measurement model

The lateral stereoscopic vision system equations (2.3) and (2.5) is reformulated in the nonlinear measurement model of equation (3.2) as following:

$$Y_m = \begin{bmatrix} ul_m \\ d_m \end{bmatrix} = h(X) + r_k = \begin{bmatrix} \frac{f_x . x}{z} + x_0 \\ \frac{f_x . b}{z} \end{bmatrix} + \begin{bmatrix} r_{UL} \\ r_d \end{bmatrix} \qquad (3.20)$$

Where m subscript denotes measured quantity, $r_k = [r_{UL} r_d]^T$ is the measurement stationary Gaussian noise with zero mean and R covariance,

$$E[r_k] = [0\ 0]^T, R = cov[r_k] = DIAG\left[\sigma_{UL}^2 \sigma_d^2\right]^T$$

In the update step the Jacobean of the measurement model function is required to be computed, So the Jacobean of $h(X)$ is

$$H_X = \left|\frac{\partial h(X)}{\partial X}\right|_X = \begin{bmatrix} \frac{f_x}{z} & -\frac{f_x.x}{z^2} & 0 & 0 & 0 \\ 0 & -\frac{f_x.b}{z^2} & 0 & 0 & 0 \end{bmatrix} \quad (3.21)$$

3.3.2 Linear measurement model

The lateral stereoscopic vision system equations (2.6) and (2.7) extract the observed vehicle position *(x,z)* relative to the ego vehicle left camera optical center; assuming additive noise, the linear measurement model for CTRPV model becomes,

$$\begin{bmatrix} x_m \\ z_m \end{bmatrix}_k = H_{CTRPV}.x_{CTRPV\,k} + r_k = \begin{bmatrix} 1 & 0 & 0 & 0 & 0 \\ 0 & 1 & 0 & 0 & 0 \end{bmatrix} \begin{bmatrix} x \\ z \\ v \\ h \\ \omega \end{bmatrix}_k + \begin{bmatrix} r_x \\ r_z \end{bmatrix} \quad (3.22)$$

and the linear measurement model for CTRA model becomes,

$$\begin{bmatrix} x_m \\ z_m \end{bmatrix}_k = H_{CTRA}.x_{CTRA_k} + r_k = \begin{bmatrix} 1 & 0 & 0 & 0 & 0 & 0 \\ 0 & 1 & 0 & 0 & 0 & 0 \end{bmatrix} \begin{bmatrix} x \\ z \\ v \\ a \\ h \\ \omega \end{bmatrix}_k + \begin{bmatrix} r_x \\ r_z \end{bmatrix} \quad (3.23)$$

Where m subscript denotes measured quantity, $r_k = [r_x r_z]^T$ is the measurement stationary gaussian noise with zero mean and R covariance, $E[n_k] = [0\ 0]^T$, $R = cov[r_k] = DIAG[\sigma_x^2 \sigma_z^2]^T$

3.3.2.1 The Linear Measurement Noise Analysis

For the selected test data of KITTI the stereo vision parameters are (f_x 721.5 pixels, b 0.54 m, x_0 609.556 pixels), and the measurements variance was computed In chapter 5 as $\sigma_d = +0.8408\ pixel$ and $\sigma_{ul} = +13.83\ pixel$, So for these parameters the linear measurement model noise $[r_x r_z]$ is analyzed. $[r_x r_z]$ is depending on nonlinear measurement model noise $[r_{UL} r_d]$ according to the following relations:

$$\sigma_x = \left[\frac{\partial x}{\partial d}\right]_d . \sigma_d + \left[\frac{\partial x}{\partial ul}\right]_{ul} . \sigma_{ul} = -\frac{(ul - x_0).b}{d^2}\sigma_d + \frac{b}{d}\sigma_{ul} \quad (3.24)$$

$$\sigma_z = \left[\frac{\partial z}{\partial d}\right]_d . \sigma_d + \left[\frac{\partial z}{\partial ul}\right]_{ul} . \sigma_{ul} = -\frac{f_x.b}{d^2}\sigma_d \quad (3.25)$$

Figure (3.1) depicts σ_z vs. σ_d for disparity in the range [5-35pixels]. For positive fixed σ_d as d decreasing σ_z increasing dramatically because d^{-2} term.

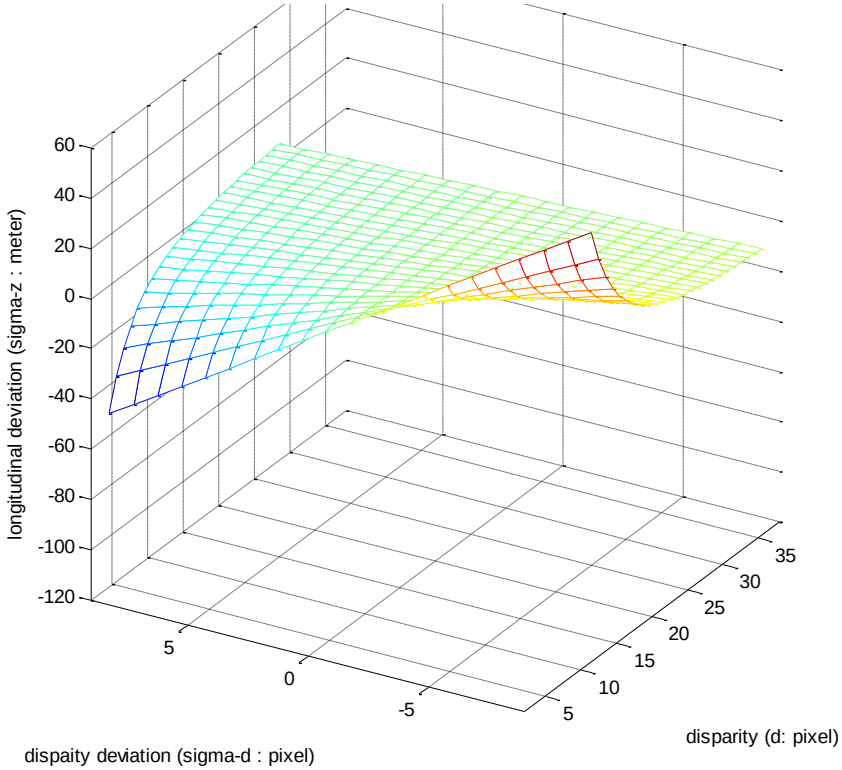

Figure (3.1): σ_z vs. d and σ_d

Figure (3.2) plots σ_z vs. z in the range [10m, 80m] its noted that point far 60m suffers -7.952m error in longitudinal position due to σ_d.

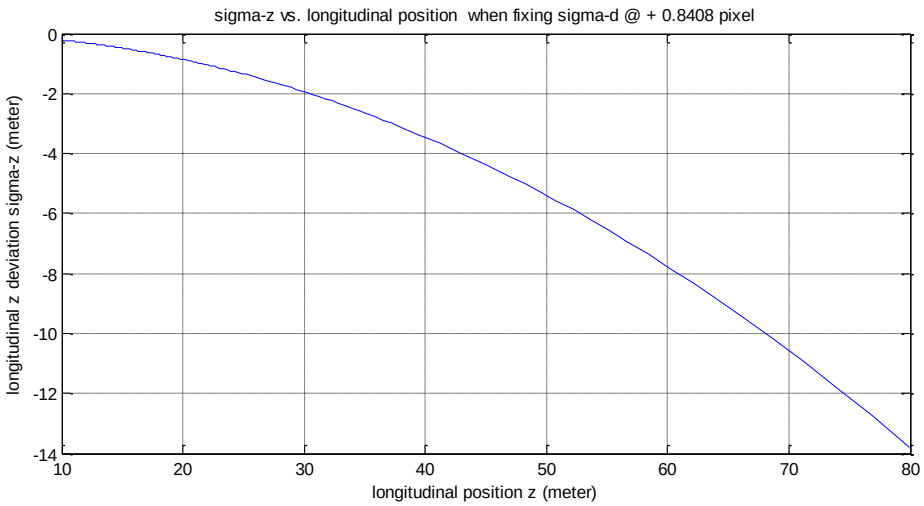

Figure (3.2): σ_z vs. z for test data nominal σ_d

Figure (3.3) depicts σ_x vs. σ_{ul} for disparity in the range [4,39] pixels equivalent to longitudinal position z in the range [97.4, 9.99] meters respectively, for KITTI stereo vision parameters, to be able represents the relation graphically we are fixing σ_d at +0.8404 pixels and ul at 800 pixels as the our work in KITTI, as the disparity d decreasing (z increasing) so σ_x changes dramatically because d^{-2} term.

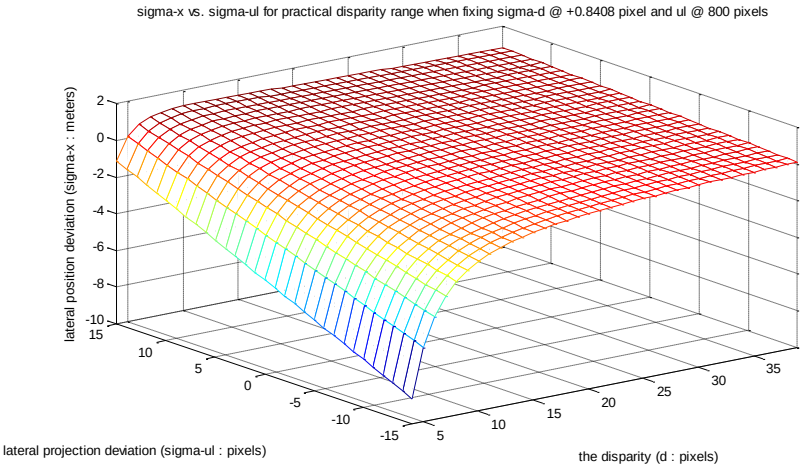

Figure (3.3): σ_x vs. σ_{ul} and σ_d

Figure (3.4) shows σ_x vs. the depth z in the range [10,90m] at KITTI nominal $ul, \sigma_{ul}\ and\ \sigma_d$, it's clear that at z ~74.5m we have $\sigma_{ul} = 0$ introducing chance of noise-by noise cancellation in the linear measurement model for future deep analysis.

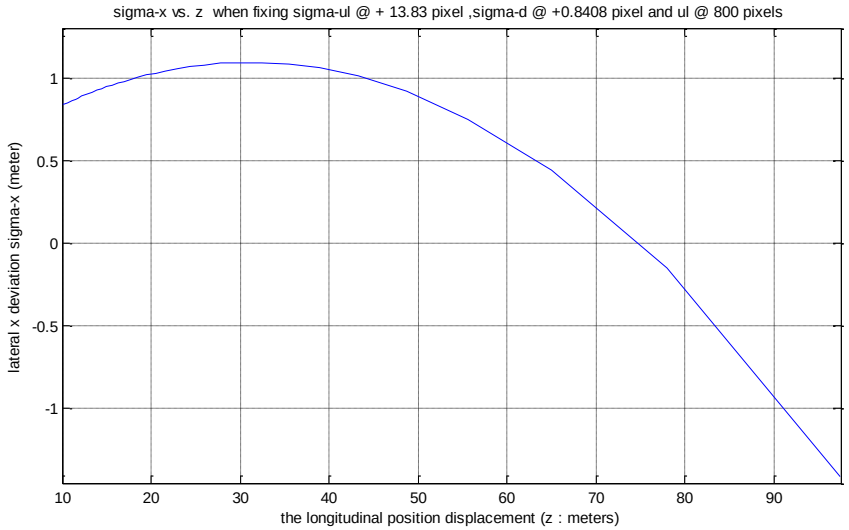

Figure (3.4): $\sigma_x$vs. z at KITTI nominal $ul, \sigma_{ul}, \sigma_d$

Figure (3.5) depicts σ_x vs. σ_{ul} at fixed $z = 74m$ for ul in the range [700,1200 pixels] at nominal σ_d for $d = 5.2653$ pixels its clear that as ul increasing (z increasing) σ_x decreasing linearly.

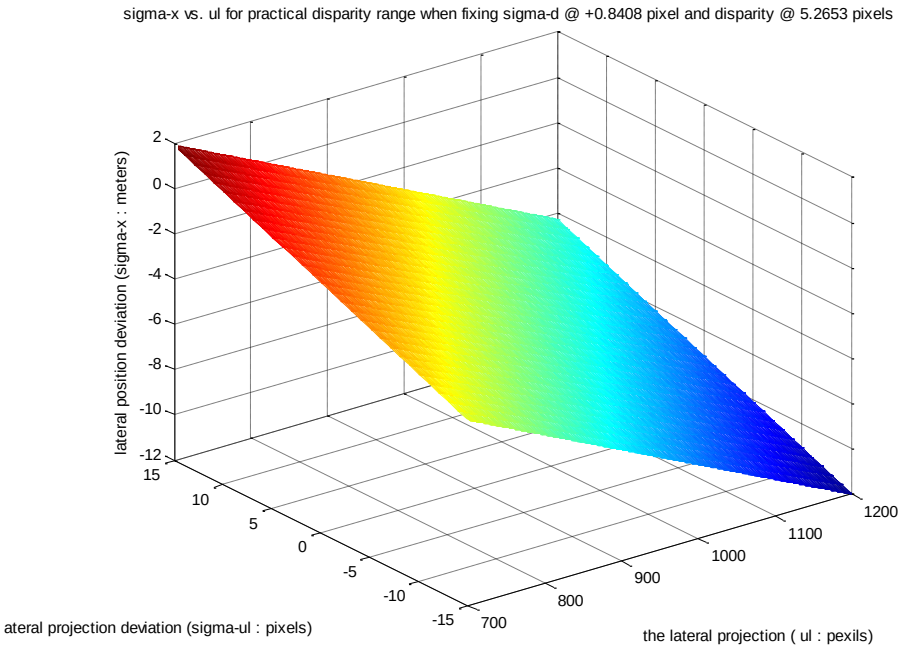

Figure (3.5): σ_x vs. σ_{ul}, ul for KITTI nominal d, σ_d

Figure (3.6) shows σ_x vs. x in the range [10m, 60m] for KITTI nominal disparity, σ_d and σ_{ul}. also, when $x = 19.74m$ we have $\sigma_x \sim 0$, introducing chance of noise-by noise cancellation in the linear measurement model for future deep analysis.

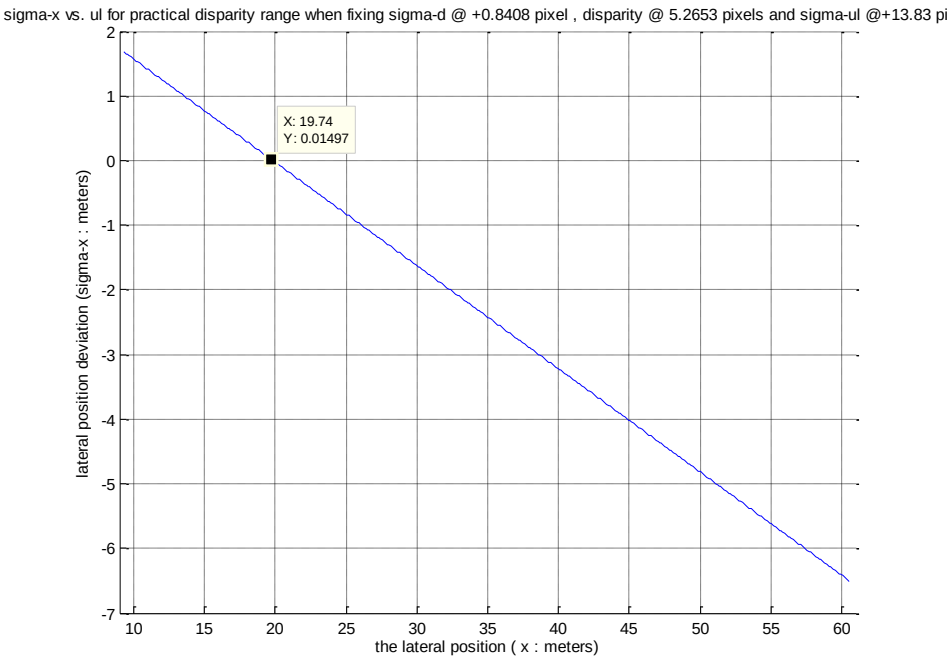

Figure (3.6): σ_x vs. x for KITTI nominal d, σ_d, σ_{ul}

3.4 Real Data Processing

All sensor readings of a sequence are zipped into a single file named by its recording date and number as shown in Figure (3.7). Timestamps are stored in timestamps.txt per frame and sensor readings are provided in the corresponding sub-folders. For each sequence, the dataset provides the object annotations in form of 3D bounding box tracklets and a calibration file (Geiger et. al. 2012).

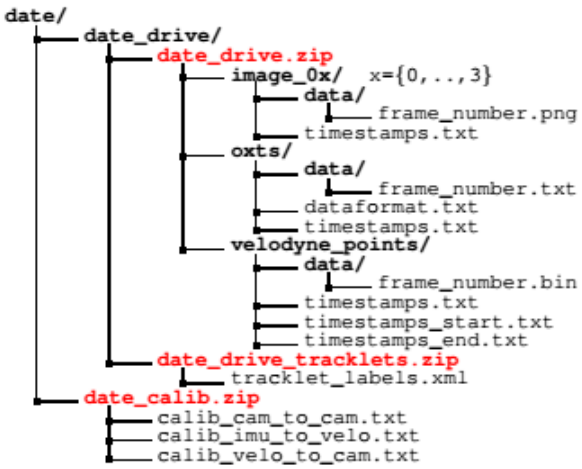

Figure (3.7): Structure of the provided Zip-Files that stores all KITTI sequences (Geiger et. al. 2012).

The sensors are prepared for the estimation algorithm as the following diagram

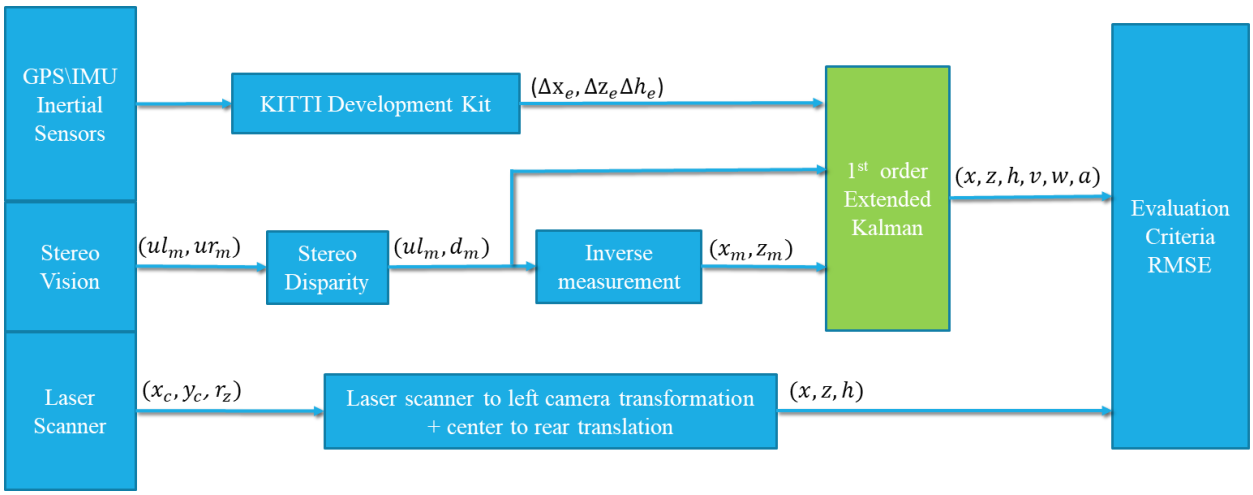

Figure (3. 8) The sensors data flow diagram

Inertial Sensors data: The information of the ego vehicle motion between each two successive stereo frames $(\Delta x_e, \Delta z_e \Delta h_e)$ are extracted from OXTS (GPS/IMU) data that provides 30 different GPS/IMU values in a text file in the geographic coordinates including altitude, global orientation, velocities, accelerations, angular rates, accuracies and satellite information.

Laser scanner data: The Laser scans are stored as floating-point binaries where each point is stored with its (*x-y-z*) coordinate and an additional reflectance value

Figure (3.9): extraction of the observed point image position (u, v) for frame no. 45

As shown in Figure (3.9) the laser scanner frame data were projected on the corresponding left camera image, the position of the interested point in the image plane *(u,w)* were extracted manually, its corresponding position in the laser scanner coordinate system was retrieved then transformed into the stereo coordinate system using the transformation matrices in the calibration file of the interested sequence.

Stereo vision sequences data: since the rectified images are available in the dataset, so we could use disparity function in MATLAB which returns the disparity map of two equi-dimensional rectified images, such that the disparity of pixel located in *(u, v)* in the left camera image is the u^{th} row, v^{th} column element of the disparity map. So, we extract the disparity of the observed point over all the frames that capture the vehicle and using the lateral stereoscopic model equations we measure the *(x, z) position* of the observed point in the ego stereo vision left camera coordinates frame system. For each dynamic object within the left camera's field of view, KITTI provide annotations in the form of 3D bounding box tracklets. Represented in Laser scanner coordinates, the tracklets are stored in date_drive_tracklets.xml. Each object is assigned a class and its 3D size (height, width, length). As illustrated in Figure (3.10), the level of occlusion and truncation is specified.

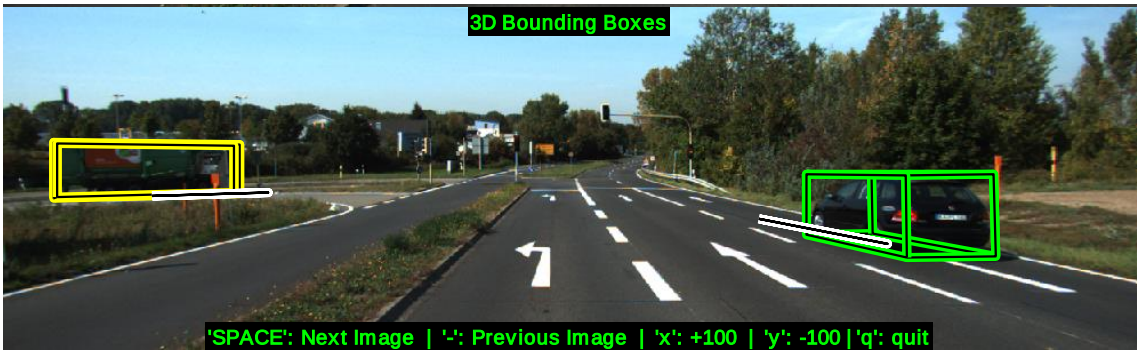

Figure (3.10): KITTI annotations: 3D bounding box tracklets in Laser scanner coordinates (Geiger et. al. 2012)..

As shown in Figure (3.11) the position data by KITTI bounding box is for the center of the observed vehicle. Since we are interested in the position of the center of the rear or the front (the visible and measured points by the stereo vision), it is derived in equations 3.26-3.27

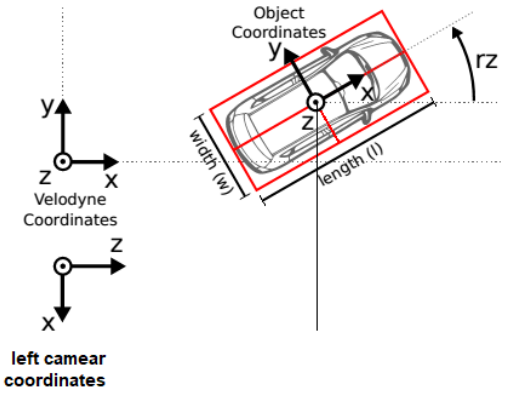

Figure (3.11): The position and yaw of annotated 3D bounding boxes in velodyne, left camera coordinate system (Geiger et. al. 2013).

$$x_{rear} = x_{center} - \frac{l}{2}cos(rz), \quad x_{front} = x_{center} + \frac{l}{2}cos(rz) \qquad (3.26)$$

$$y_{rear} = y_{center} - \frac{l}{2}sin(rz), \quad y_{front} = y_{center} + \frac{l}{2}sin(rz) \qquad (3.27)$$

Where l is the length of the observed vehicle, rz is its heading from velodyne x-axis. So in order to convert rz from left camera x-axis h we apply eq. 3.28

$$h = rz + \frac{\pi}{2} \qquad (3.28)$$

3.4.1 Assigning the coordinate frames/Matrix transformations

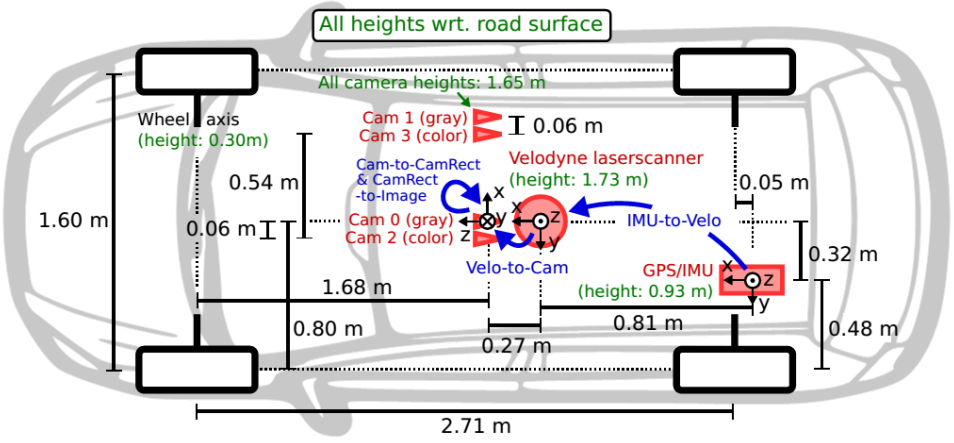

Figure (3.12): The Sensory Package Setup (Geiger et. al. 2013).

Figure (3.12) illustrates the dimensions and mounting positions of the sensors (red) with respect to the ego vehicle body. Heights above ground are marked in green and measured with respect to the road surface. Transformations between sensors are shown in blue. The coordinate systems are defined as illustrated in Figure (2.2) and Figure (3.11), i.e.:

- Camera: x = right, y = down, z = forward
- Velodyne: x = forward, y = left, z = up
- GPS/IMU: x = forward, y = left, z = up

The rigid body transformation from Laser scanner coordinates to left camera coordinates is given by KITTI for every day of recording in calib_velo_to_cam.txt in terms of 3*3 rotation matrix and 3 translation column vectors. The transformation (2011_09_26_drive_0029_sync) sequence of test data no. 1 rigid body by the dataset is given by:

$$\begin{bmatrix} x \\ y \\ z \end{bmatrix}_{left\ camera} = \begin{bmatrix} 0.0075 & -1 & -0.0006 \\ 0.0148 & 0.0007 & -0.9999 \\ 0.9999 & 0.0075 & 0.0148 \end{bmatrix} \begin{bmatrix} x \\ y \\ z \end{bmatrix}_{velodyne} + \begin{bmatrix} 0.0041 \\ -0.0763 \\ -0.2718 \end{bmatrix} \quad (329)$$

Chapter 4

Observability

Chapter 4
Observability

In this chapter we discuss the observability property of our system. The number of observable states of linear time-invariant (LTI) system equales the rank of the observability matrix which can be formulated from the system matrix A, and the output matrix C. Thus, the output matrix in the measurement model and the system matrix can be derived from the CTRPV and the CTRA models.

4.1 Observability of CT-CTRPV model

Look at CT-CTRA model in equation (2.15) in the form $\dot{X} = f(X) + U$, we got the linearized system matrix A_{CTRPV} via computing the Jacobean of the state transition function $f(X)$

$$A_{CTRPV} = \left|\frac{\partial f(X)}{\partial X}\right|_{X(t)} = \begin{bmatrix} \frac{\partial \dot{x}_1}{\partial x_1} & \cdots & \frac{\partial \dot{x}_1}{\partial \omega} \\ \vdots & \ddots & \vdots \\ \frac{\partial \dot{\omega}}{\partial x_1} & \cdots & \frac{\partial \dot{\omega}}{\partial \omega} \end{bmatrix} = \begin{bmatrix} 0 & 0 & \cos(h) & -v\sin(h) & 0 \\ 0 & 0 & \sin(h) & v\cos(h) & 0 \\ 0 & 0 & 0 & 0 & 0 \\ 0 & 0 & 0 & 0 & 1 \\ 0 & 0 & 0 & 0 & 0 \end{bmatrix} \quad (4.1)$$

A_{CTRPV} depends only on $h, and\ v,$. For the linear measurement model in equation (3.22), the observability matrix O is

$$O = \begin{bmatrix} H \\ HA_{CTRPV} \\ \vdots \\ HA_{CTRPV}^{n-1} \end{bmatrix} = \begin{bmatrix} 1 & 0 & 0 & 0 & 0 \\ 0 & 1 & 0 & 0 & 0 \\ 0 & 0 & c(h) & -vs(h) & 0 \\ 0 & 0 & s(h) & vc(h) & 0 \\ 0 & 0 & 0 & 0 & 0 \\ 0 & 0 & 0 & 0 & -vs(h) \\ 0 & 0 & 0 & 0 & vc(h) \\ 0 & 0 & 0 & 0 & 0 \\ \vdots & \ddots & & & \vdots \\ 0 & \ldots & & & 0 \end{bmatrix}_{10*5} \quad (4.2)$$

From analytical review of O, we say that:

1. The zero polar velocity $(v = 0)$, yields last two columns to be zeros reducing the rank to 3 (which means that there are two states unobservable, that are related to the zero columns which are the last two states: the heading angle h and the angle change rate ω)
2. The 3rd and 4th columns are identical if
    a. $c(h) = -vs(h)$

b. $s(h) = vc(h)$

$which\ yields\ \frac{-c(h)}{s(h)} = \frac{s(h)}{c(h)} \xrightarrow{yields} c^2(h) + s^2(h) = 0\ which\ is\ impossible,$. Therefore, the CT-CTRPV model is observable for all of its state space unless *(v = 0)*. Using MATLAB, we numerically examine the observability on the space and the results were typical.

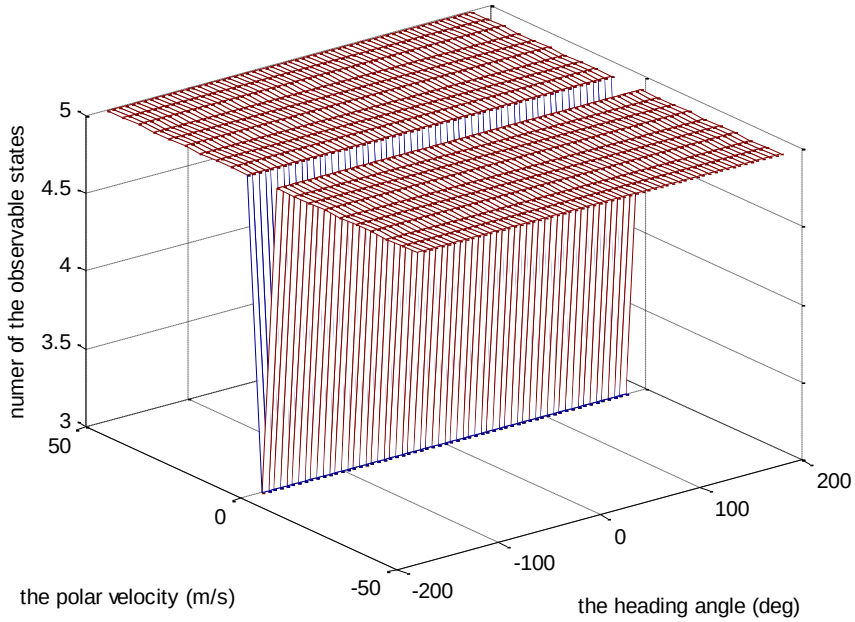

Figure (4.1): The observability surface of CT-CTRPV model

4.2 Observability of CT-CTRA model

Looking at CT-CTRA model in equation (2.24) in the form $\dot{X} = f(X) + U$, we get the linearized system matrix A_{CTRA} via computing the Jacobean of the state transition function$f(X)$ such as

$$A_{CTRA} = \left|\frac{\partial f(X)}{\partial X}\right|_{X(t)} = \begin{bmatrix} 0 & 0 & \cos(h) & 0 & -v\sin(h) & 0 \\ 0 & 0 & \sin(h) & 0 & v\cos(h) & 0 \\ 0 & 0 & 0 & 1 & 0 & 0 \\ 0 & 0 & 0 & 0 & 0 & 0 \\ 0 & 0 & 0 & 0 & 0 & 1 \\ 0 & 0 & 0 & 0 & 0 & 0 \end{bmatrix} \quad (4.3)$$

As in CT-CTPRV analysis, A_{CTRA}depends only on $h, and\ v$. For the linear measurement model in equation (3.23) the observability matrix O is such as

$$O_{CTRA} = \begin{bmatrix} H \\ HA_{CTRA} \\ \vdots \\ HA_{CTRA}^{n-1} \end{bmatrix} = \begin{bmatrix} 1 & 0 & 0 & 0 & 0 & 0 \\ 0 & 1 & 0 & 0 & 0 & 0 \\ 0 & 0 & c(h) & 0 & -vs(h) & 0 \\ 0 & 0 & s(h) & 0 & vc(h) & 0 \\ 0 & 0 & 0 & c(h) & 0 & -vs(h) \\ 0 & 0 & 0 & s(h) & 0 & vc(h) \\ 0 & 0 & 0 & 0 & 0 & 0 \\ 0 & 0 & 0 & 0 & 0 & 0 \\ \vdots & \ddots & \vdots & \vdots & & \vdots \\ 0 & \dots & \dots & \dots & & 0 \end{bmatrix}_{10*6} \quad (4.4)$$

From analytical review of O_{CTRA},we say that:

1. The zero polar velocity ***(v = 0)***, yields last two columns to be zeros reducing the rank to 4 (which means that there are two states unobservable, that are related to the zero columns which are the last two states: the heading angle ***h*** and the angle change rate ω).
2. The 3rd and 5th columns or the 4th and 6th columns are identical if both
   a. $c(h) = -vs(h)$
   b. $s(h) = vc(h)$

$which\ yields\ \frac{-c(h)}{s(h)} = \frac{s(h)}{c(h)} \xrightarrow{yields} c^2(h) + s^2(h) = 0\ which\ is\ impossible$, Thus, the CT-CTRA model is observable for all of its state space unless ***(v = 0)***. Using MATLAB, we numerically examine the observability on the space and the results were typical.

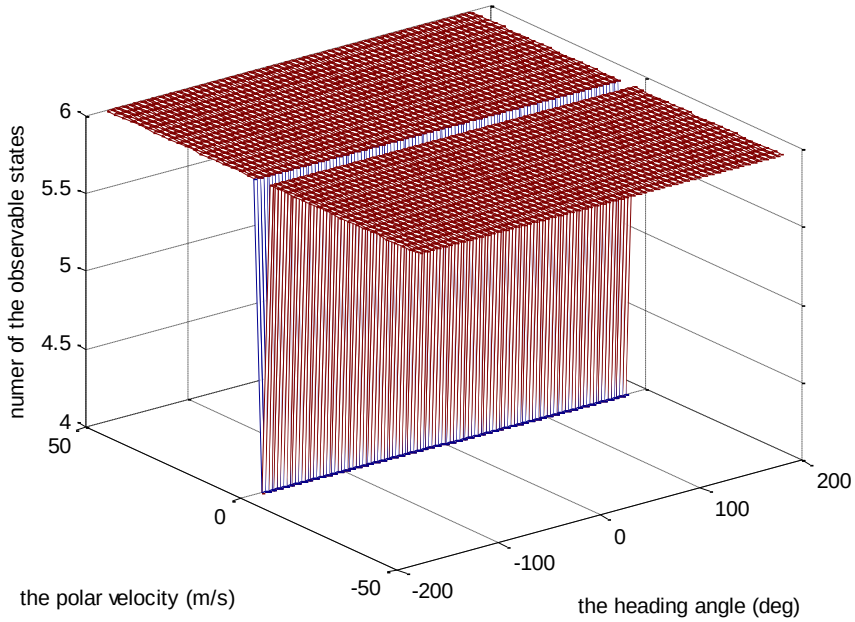

Figure (4.2): The observability surface of CT-CTRA model

4.3 Observability of DT-CTRPV model

Discrete time CTRPV nonlinear model where the input part seperated from the state transition part is

$$\begin{bmatrix} x \\ z \\ v \\ h \\ \omega \end{bmatrix}_{k+1} = \begin{bmatrix} x + \frac{2v}{\omega}\sin\left(\frac{\omega T}{2}\right)\cos\left(h + \frac{\omega T}{2}\right) \\ z + \frac{2v}{\omega}\sin\left(\frac{\omega T}{2}\right)\sin\left(h + \frac{\omega T}{2}\right) \\ v \\ h + \omega T \\ \omega \end{bmatrix}_k + \begin{bmatrix} 0 & 0 \\ 0 & 0 \\ T & 0 \\ 0 & 0 \\ 0 & T \end{bmatrix} w_k \qquad (4.5)$$

By first order linearization, we get the system matrix $\boldsymbol{A}$ via computing the Jacobean of the state transition part.

$$A = \left|\frac{\partial f(x)}{\partial x}\right|_{x(t)} = \begin{bmatrix} 1 & 0 & \frac{2}{\omega}\mathrm{s}\left(\frac{\omega T}{2}\right)\mathrm{c}\left(h + \frac{\omega T}{2}\right) & \frac{-2v}{\omega}\mathrm{s}\left(\frac{\omega T}{2}\right)\mathrm{s}\left(h + \frac{\omega T}{2}\right) & \frac{\partial x_{k+1}}{\partial \omega_k} \\ 0 & 1 & \frac{2}{\omega}\mathrm{s}\left(\frac{\omega T}{2}\right)\mathrm{s}\left(h + \frac{\omega T}{2}\right) & \frac{2v}{\omega}\mathrm{s}\left(\frac{\omega T}{2}\right)\mathrm{c}\left(h + \frac{\omega T}{2}\right) & \frac{\partial z_{k+1}}{\partial \omega_k} \\ 0 & 0 & 1 & 0 & 0 \\ 0 & 0 & 0 & 1 & T \\ & & 0 & 0 & 1 \end{bmatrix} \qquad (4.6)$$

Where

$$\frac{\partial x_{k+1}}{\partial \omega_k} = \frac{vT}{\omega}c\left(\frac{\omega T}{2}\right)\mathrm{c}\left(h + \frac{\omega T}{2}\right) - \frac{2v}{\omega^2}s\left(\frac{\omega T}{2}\right)\mathrm{c}\left(h + \frac{\omega T}{2}\right) - \frac{vT}{\omega}s\left(\frac{\omega T}{2}\right)\mathrm{s}\left(h + \frac{\omega T}{2}\right)$$

$$\frac{\partial z_{k+1}}{\partial \omega_k} = \frac{vT}{\omega}c\left(\frac{\omega T}{2}\right)\mathrm{s}\left(h + \frac{\omega T}{2}\right) - \frac{2v}{\omega^2}s\left(\frac{\omega T}{2}\right)\mathrm{s}\left(h + \frac{\omega T}{2}\right) + \frac{vT}{\omega}s\left(\frac{\omega T}{2}\right)\mathrm{c}\left(h + \frac{\omega T}{2}\right)$$

It's clear that the matrices $\boldsymbol{A}$ and $\boldsymbol{O}$ only depends on $v, h, \omega, and\ T$, such that they are very complicated to be analyzed mathematically.

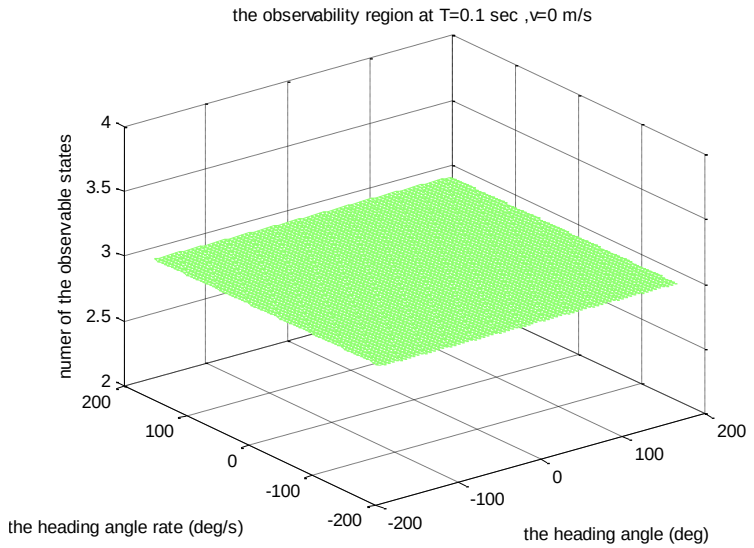

Figure (4.3): DT-CTRPV observability surface at 0.1sT, 0 m/s v

Thus, we use Matlab for visual examination with fixed T at the nominal sampling time (0.1 sec) in KITTI dataset and draw the rank of $\mathcal{O}$ as a function of heading angle $h\ from\ -180$ to 180 deg , $and\ \omega$ from -180 to 180 deg/sec for some meaningful values of v (0 m/s , 10 m/s and 1e+10 m/s). The results are shown in figures (4.3 and 4.5). At zero velocity, the observable states are reduced to three that is exactly matching the CT-CTRPV analysis.

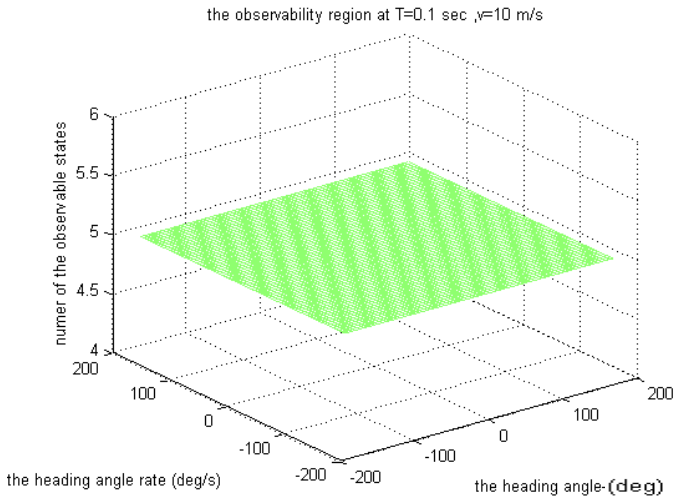

Figure (4.4): DT-CTRPV observability surface at 0.1 sampling time and 10 m/s polar velocity

At 10 m/s velocity the model is fully observable in the space of heading angle (-180 deg to 180 deg), and for large scale angle rate. Since we concern the on-road vehicles motion, this range is very good.

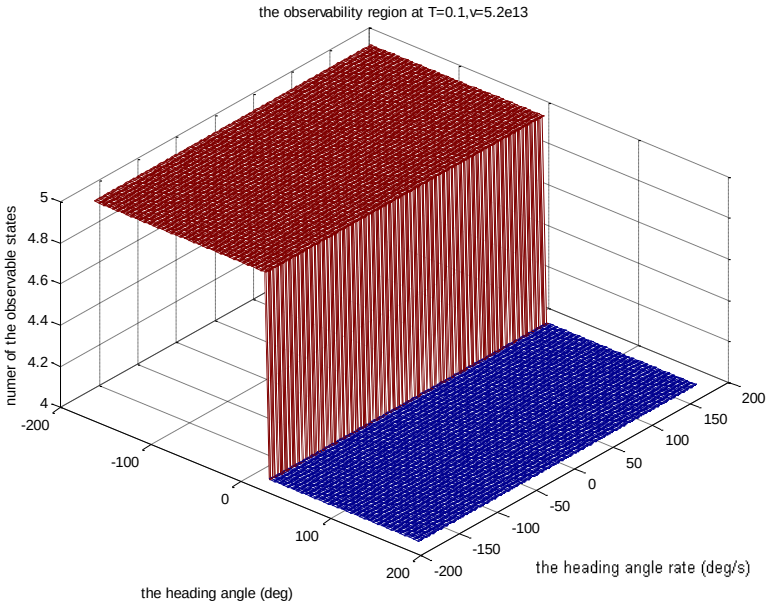

Figure (4.5): DT-CTRPV observability surface @ 0.1s T,1e+06 m/s v

By increasing the velocity exponentially and drawing the rank of O. we noticed that the model was fully observable in the stated range. Until the velocity reached 5.2e+13 m/s, the observable states are reduced to four for $h \notin [-180^{\circ}, 15^{\circ}]$. This is because numerical errors related to the numbers conditioning in MATLAB; however, on-road vehicles motion don't reach this high velocity. Therefore, the DT model of CTRPV is fully observable for all practical state-subspace.

4.4 Observability of DT-CTRA model

The discrete time CTRA nonlinear model state transition part is

$$\begin{bmatrix} x \\ z \\ v \\ a \\ h \\ \omega \end{bmatrix}_{k+1} = \begin{bmatrix} x + \frac{1}{\omega^2}[(v\omega + a\omega T)s(h + \omega T) + a * c(h + \omega T) - v\omega s(h) - a * \mathrm{c}(h)] \\ z + \frac{1}{\omega^2}[(-v\omega - a\omega T)c(h + \omega T) + a * s(h + \omega T) + v\omega c(h) - a * \mathrm{s}(h)] \\ v + aT \\ a \\ h + \omega T \\ \omega \end{bmatrix}_k \quad (4.7)$$

It is very complicated to get the analytical solution for the Jacobean. however, we could say analytically that linearized system matrix depends on $(v, a, h, \omega, and\ T)$ but doesn't ever depends on the position x, z.

MATLAB is used for numerical computation of the Jacobean and for visual examination. Again fixing T at the nominal sampling time (0.1 sec) in KITTI dataset, then drawing the rank of O as a function of heading angle $h\ from\ -180$ to 180 deg , ω from -180 to 180 deg/sec for some meaningful values of v (0 m/s , 10 m/s and 1e+06 m/s) and a (0 m/s^2, 10 m/s^{2}and 1e+06 m/s^2), the obtained results are shown in Figure (4.6-8).

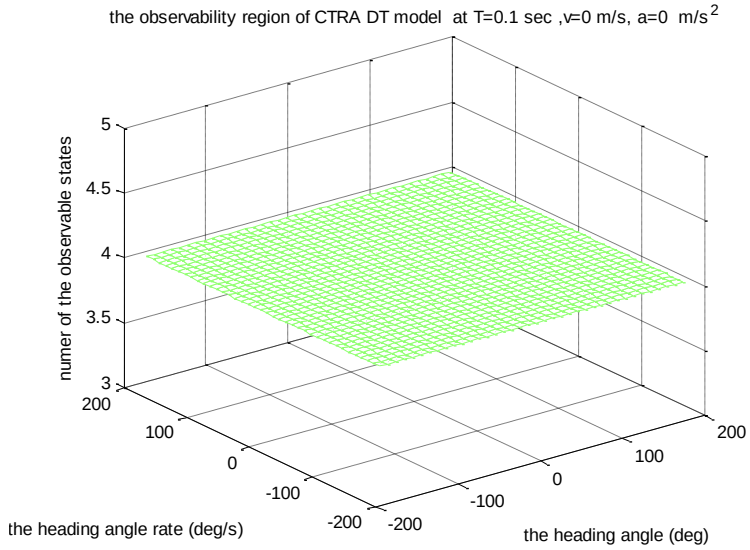

Figure (4.6): DT-CTRA observability surface @ 0.1s T,0 m/s v,0 m/s^2 a

AS shown in Figure (4.6) the zero velocity reduces the observable states to four which is exactly matching the CT-CTRA analysis, while from Figure (4.7) and Figure (4.8) , we could considered that the DT model of CTRA is fully observable for on-road vehicles practical motion range (the velocity less than 2.5e0+7m/s and the acceleration less than 2.5e0+7m/s2).

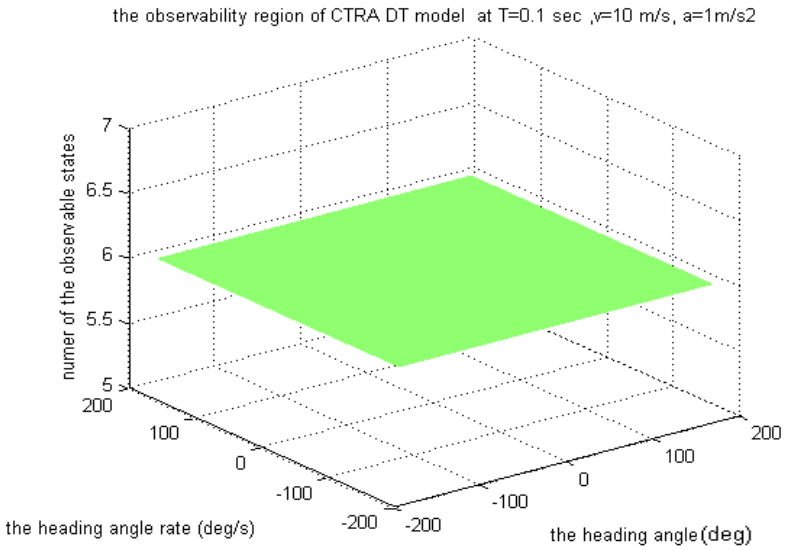

Figure (4.7): DT-CTRA observability surface @ 0.1s T,10 m/s v,1 m/s^2 a

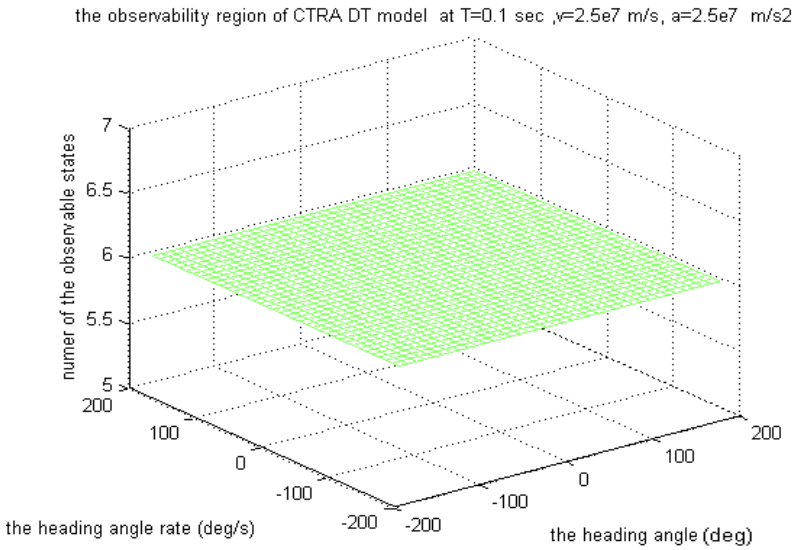

Figure (4.8): DT-CTRA observability surface @ 0.1s T,2. e7 m/s v,2.57e7 m/s^2 a

4.5 Summary

The observability property for the proposed approach was inspected in this chapter through the analytical and the numerical calculation of the observability matrix O rank. Table (4.1) summarizes the results since it depicts the number of observable states by the variant models, the unobservable states are stated in {} brackets

The model	$v = 0$	$\|v\| \gg 0$	$\omega \in [-\pi, \pi]$
CT-CTRPV	3 $\{h,\omega\}$	5	5
CT-CTRA	4 $\{h,\omega\}$	6	6
DT-CTRPV	3 $\{h,\omega\}$	4	5
DT-CTRA	4 $\{h,\omega\}$	5	6

Table (4.1): The system observability property summary

It's found that for nonmoving observed vehicle ($v = 0$) all the continuous and discrete time models could not estimate the heading and the turn rate. The continuous time models are full observable over the rest state space. The discrete time models discretized by KITTI dataset sampling time (0.1 s) are full observable for all practical vehicles speeds for the observed vehicles turn rate in the range $\omega \in [-\pi, \pi] rad/s$, also they are full observable for very high speeds that exceeds 1e+6 m/s, that is because through the observability test its assumed that the observed vehicle position observations (x, z) are available and unlimited, that is could not be achieved by a real stereo vision system because its limited range. So, for limited range observations of the observed vehicle position the maximum observable speed v_{max} is limited by the least distance that the observed vehicle travel in the stereo vision field of view (FOV) divided by the period required for sufficient number of the observed vehicle position observations.

Figure (4.9) shows that the least distance *dist* that the observed vehicle could interpret through the stereo field of view FOV achieved if the observed vehicle intersects FOV perpendicular on stereo z-axis with zero turn rate. From simple triangulation for KITTI stereo horizontal FOV of 90 deg the least distance is $[dist = 2 * z]$, where z represents the longitudinal distance of the observed trajectory from the stereo.

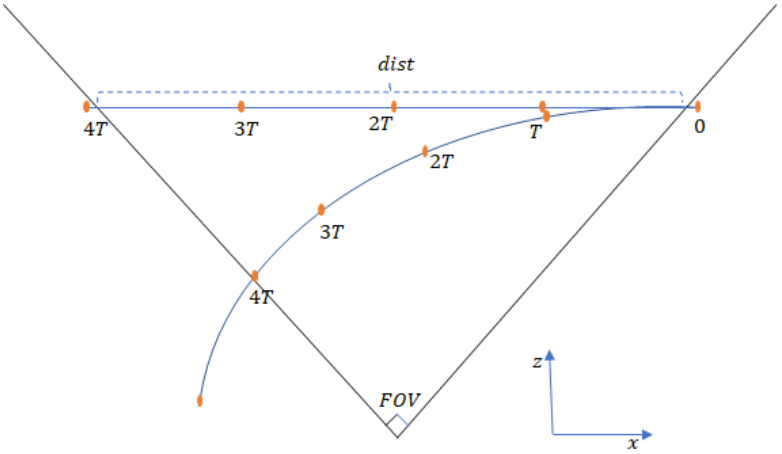

Figure (4.9): the trajectory of vehicle interpreted the ego stereo FOV

In order to measure the polar velocity or heading it's required that the stereo vision system could capture at least two position observations which require three time samples at worst case, while the measurement of acceleration or turn rate require three captured position observations which require four time samples at worst case, so the maximum allowable speed for KITTI stereo system is

$$v_{max} = \frac{dist}{4 * T} = \frac{2 * z}{4 * 0.1} = 5 * z$$

Practically the on-road vehicles maximum speed of 200 km/h could be recognized if the observed vehicle inters FOV farther than 11m longitudinally.

Chapter 5

Results and Discussions

Chapter 5
Results and Discussions

The proposed approach was implemented using MATLAB. The performance of the EKF depends mainly on the initial estimated state vector $\hat{X}_{0|0}$, initial estimated state covariance matrix $P_{0|0}$, the process noise covariance matrix Q, and the measurement noise covariance matrix R. In the following sections, the results of applying the developed models would be shown, the impact of the listed factors would be discussed. The evaluation metric of the estimation performance is the root mean square of the estimation error.

5.1 Synthesized Data Set

The data of the observed vehicle motion were generated using CT-CTRA model, which is implemented using Simulink model as shown in figure (5.1).

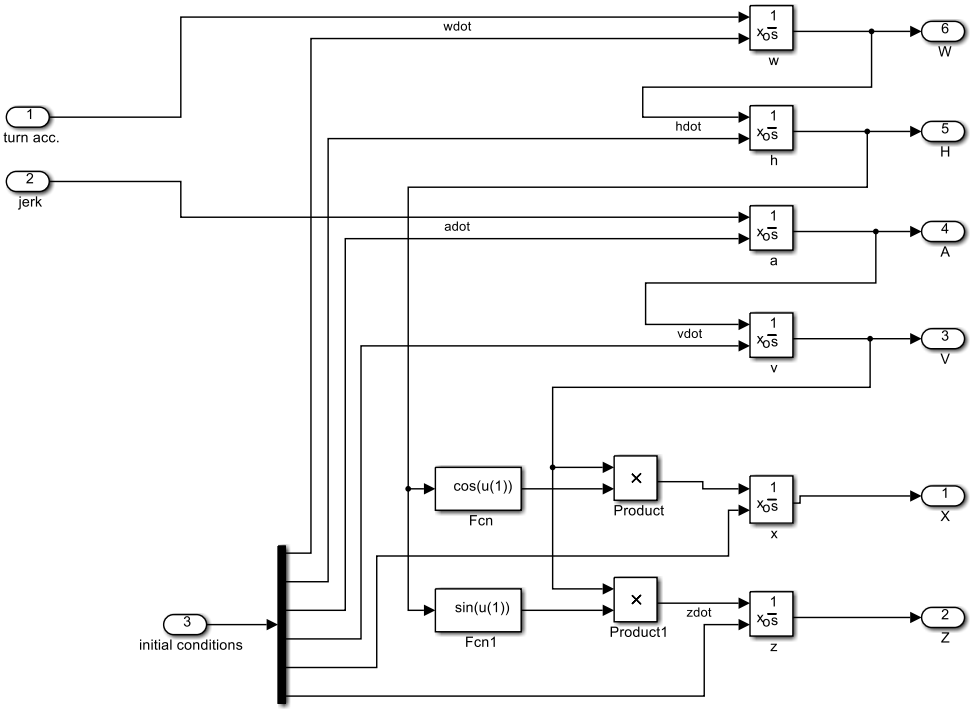

Figure (5.1): The synthesized data generation simulink model

The model was excited by the initial conditions, the jerk and the turn acceleration inputs. Then, the data of the observed vehicle position x, z were corrupted by predetermined additive white noise to be used for the purpose of testing the linear measurement model based filters. The nonlinear measurements (the left camera projection and the disparity)

were generated using the parameters of our practical stereo vision system (baseline b of 54 cm, focal length f of 721 pixels, image plane center $[x_0, y_0]$ of [610,132] pixels), also were corrupted by predetermined additive white noise to be used for the purpose of testing the nonlinear measurement model based filters. Data were classified into two categories: free motion test data and practical on-road designed situations test data.

5.1.1 Free motion test data

In this category, the CT-CTRA model is excited by Gaussian white noise inputs jerk ~N(0, σ_J^2 m/s^3) and turn acceleration ~N(0, σ_α^2 rad/s^2). While the initial states were determined arbitrarily, no constraints were assumed on the position, heading, polar velocity, acceleration or turn rate, The EKF is provided by the true initial conditions $\hat{X}_{0|0}, P_{0|0}$, the true model noise characteristics $\sigma_J^2, \sigma_a^2, \sigma_\alpha^2$, and the true measurement noise characteristics $\sigma_x^2, \sigma_z^2, \sigma_d^2, \sigma_{ul}^2$, the initial states could be fully deterministic, partially deterministic or fully stochastic. In this section, the performance of the filters with fully stochastic initial conditions would be inspected, since it is the more realistic situation, interested in the asymptotic convergence of the filter from wrong and far initial states.

5.1.1.1 Known stochastic initial conditions

This is the situation where the initial estimate variance $P_{0|0}$ is known, but the initial states $\hat{X}_{0|0}$ are unknown, First we inspect the filter performance of the known fully stochastic initial conditions for zero initial states, So the initial estimate covariance should be the square of the true initial state for DT-CTRPV EKF:

$$\hat{X}_{0|0} = \begin{bmatrix} \hat{x} \\ \hat{z} \\ \hat{v} \\ \hat{h} \\ \hat{\omega} \end{bmatrix}_{0|0} = \begin{bmatrix} 0 \\ 0 \\ 0 \\ 0 \\ 0 \end{bmatrix}, P_{0|0} = cov \begin{bmatrix} \hat{x} \\ \hat{z} \\ \hat{v} \\ \hat{h} \\ \hat{\omega} \end{bmatrix}_{0|0} = \begin{bmatrix} x_0^2 & 0 & 0 & 0 & 0 \\ 0 & z_0^2 & 0 & 0 & 0 \\ 0 & 0 & v_0^2 & 0 & 0 \\ 0 & 0 & 0 & h_0^2 & 0 \\ 0 & 0 & 0 & 0 & \omega_0^2 \end{bmatrix} \quad (5.1a)$$

And for DT-CTRA EKF :

$$\hat{X}_{0|0} = \begin{bmatrix} \hat{x} \\ \hat{z} \\ \hat{v} \\ \hat{a} \\ \hat{h} \\ \hat{\omega} \end{bmatrix}_{0|0} = \begin{bmatrix} 0 \\ 0 \\ 0 \\ 0 \\ 0 \\ 0 \end{bmatrix}, P_{0|0} = cov \begin{bmatrix} \hat{x} \\ \hat{z} \\ \hat{v} \\ \hat{h} \\ \hat{\omega} \end{bmatrix}_{0|0} = \begin{bmatrix} \sigma_x^2 & 0 & 0 & 0 & 0 & 0 \\ 0 & \sigma_z^2 & 0 & 0 & 0 & 0 \\ 0 & 0 & v_0^2 & 0 & 0 & 0 \\ 0 & 0 & 0 & a_0^2 & 0 & 0 \\ 0 & 0 & 0 & 0 & h_0^2 & 0 \\ 0 & 0 & 0 & 0 & 0 & \omega_0^2 \end{bmatrix} \quad (5.1b)$$

Figure (5.2) shows the filter configuration of known stochastic initial conditions with known process, measurement variance and initial conditions of (5.1a)

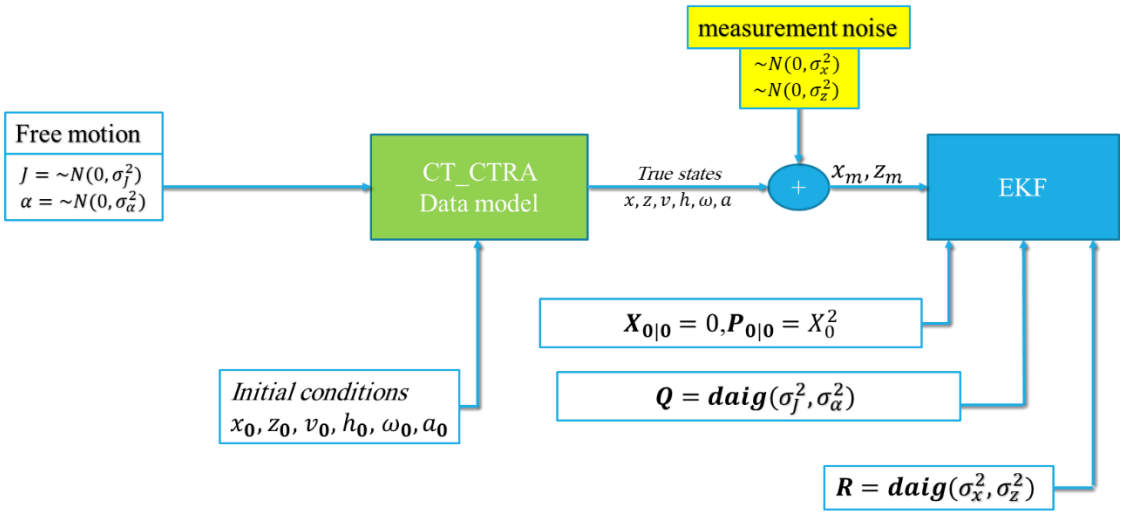

Figure (5.2): The filter configuration of known stochastic initial conditions with known process, measurement variance and initial conditions of (5.1)

Table (5.1) depicts the RMS estimation error of the distance, v, h, ω for 250 sec simulation time of data generated by CT-CTRA model with initial conditions of $(x_0, z_0, v_0, h_0, a_0, \omega_0)$ and Gaussian noise jerk, turn acceleration of ~N(0, σ_J^2 m/s^3), ~N(0, σ_α^2 rad/s^2) provided by the measured position corrupted by Gaussian noise of ~N(0, σ_x^2 m),~N(0, σ_z^2 m/s^3), where the empty *a* row represents CTRPV_EKF results, while the nonempty *a* row represents CTRA_EKF results.

Table (5.1): The RMS estimation error of CTRPV_EKF, CTRA_EKF with known process, measurement variance and initial conditions of (5.1a)

CT-CTRA synthesizing data model parameters											The RMS estimation error				
x_0	z_0	v_0	h_0	a_0	ω_0	σ_α^2	σ_J^2	σ_x^2	σ_z^2	σ_a^2	$dist$	v	h	ω	a
50	50	20	0	2	15	2^2	2^2	2^2	2^2	31.6^2	1.8	6.13	5.96	9.04	
50	50	20	0	2	15	2^2	2^2	2^2	2^2	31.6^2	1.67	6.12	2.16	7.3	0.43

Figure (5.3) shows that the estimated trajectories converge to the true trajectory with RMS estimation error of 1.8m ,1.67m of CTRPV_EKF, CTRA_EKF respectively.

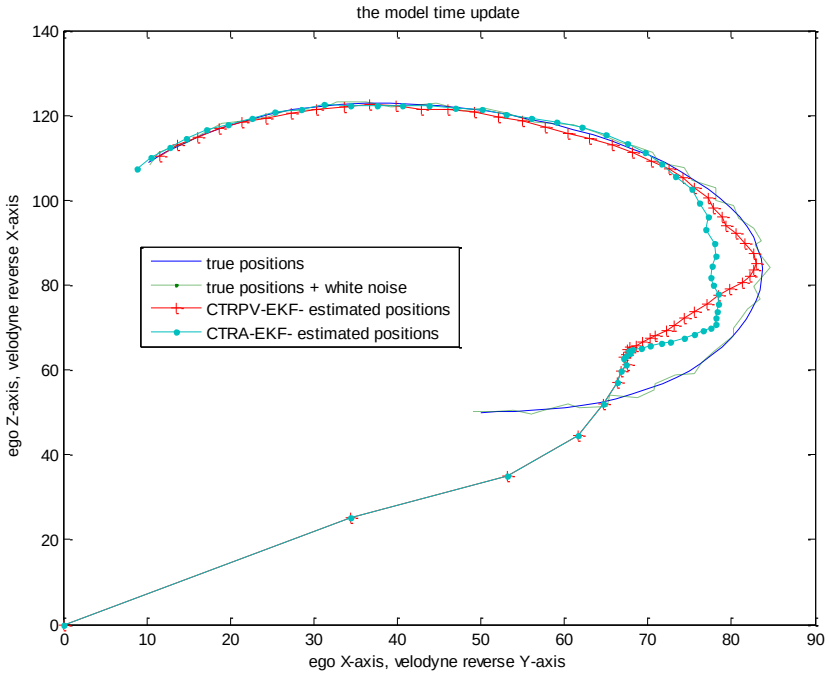

Figure (5.3): Estimated trajectory by EKF configured as in Table (5.1)

Figure (5.4) shows very good polar velocity estimation with RMS estimation error of 6.13m/s, 6.12m/s of CTRPV_EKF, CTRA_EKF respectively over the whole estimation period (250 seconds). However, the CTRPV converges in 5s while CTRA in 6s. CTRPV is biased by about 2.65m/s steady error with less undershoot than CTRA.

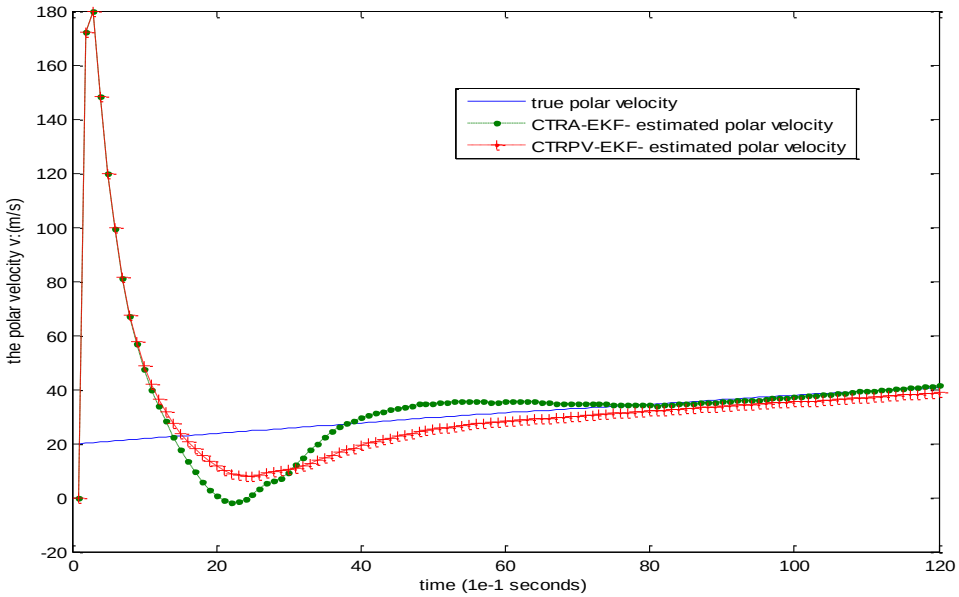

Figure (5.4): Estimated polar velocity by EKF configured as in Table (5.1)

Figure (5.5) shows that the estimated heading by converges to the true heading in less than 5 seconds with RMS RMS estimation error of 5.96 deg, 2.16 deg for CTRPV, CTRA

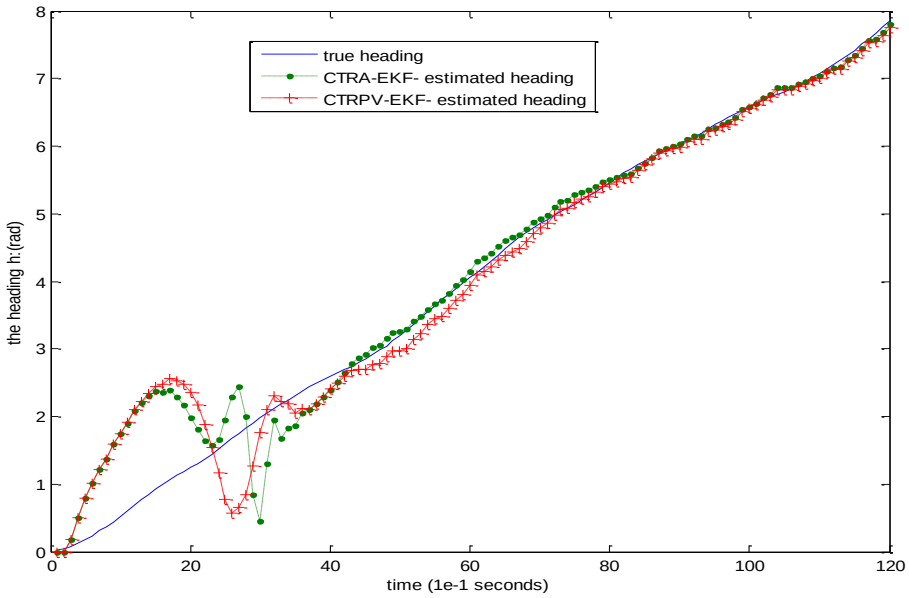

Figure (5.5): Estimated heading by EKF configured as in Table (5.1)

Figure (5.6) shows that the estimated turn rate converges fluctuating about the true state in less than 8 seconds with RMS estimation error of 9.04 deg/s, 7.3 deg/s for CTRPV, CTRA respectively.

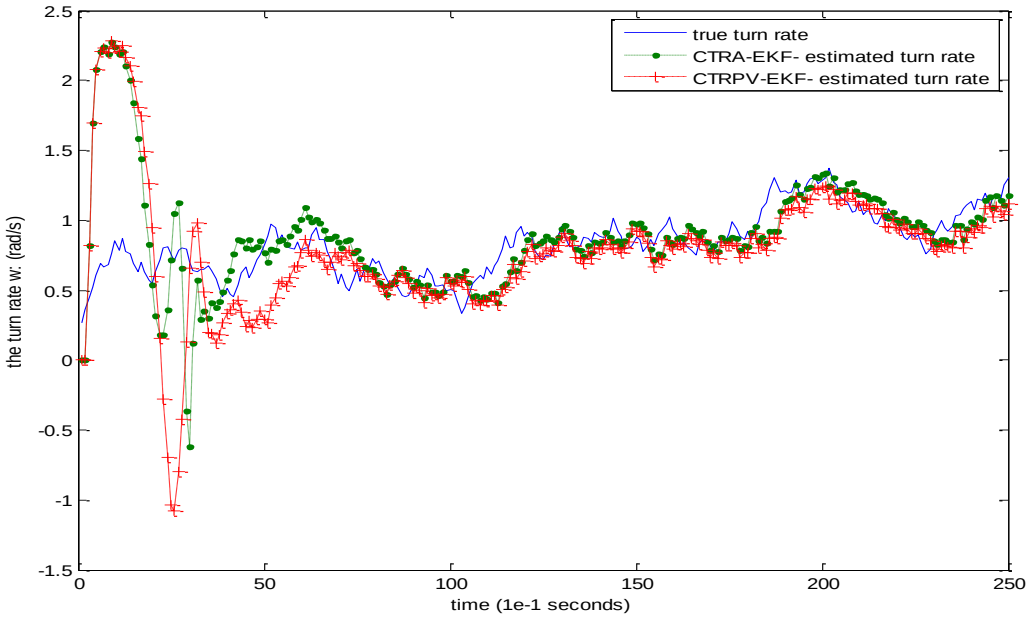

Figure (5.6): Estimated turn rate by EKF configured as in Table (5.1)

Figure (5.7) shows the convergence of the filter for the forward acceleration in 5 seconds with noise fluctuating about the true with RMS estimation error of 0.43 m/s^2 for 250 sec simulation due the far initial conditions.

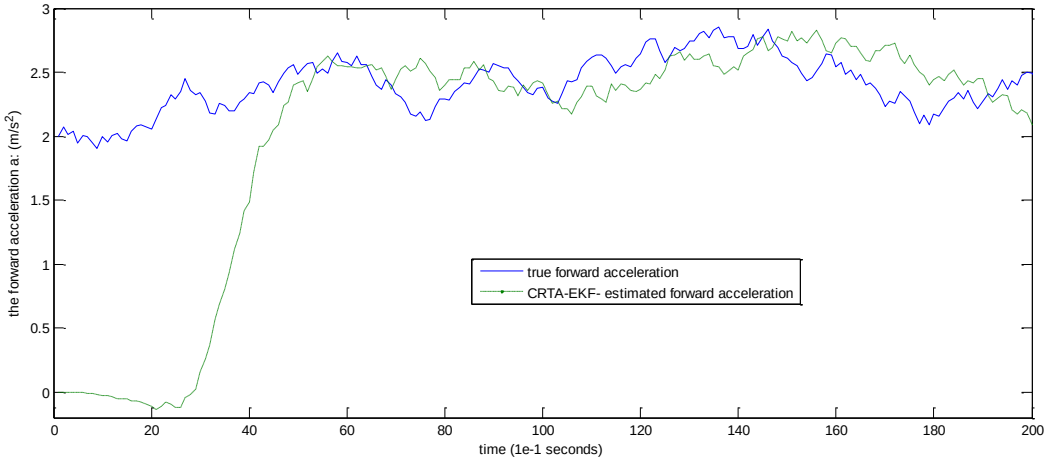

Figure (5.7): Estimated acceleration by EKF configured as in Table (5.1)

The RMS estimation error listed in Table (5.1) doesn't indicate steady error since all the estimated stated converges to true states as shown in figures (5.3-7), the error RMS is due to the pre-convergence error caused by the far filter initial conditions and the high variance of the excitation.

Table (5.2) also depicts the RMS estimation error for 250 sec simulation time of data generated with the same initial conditions and excitation as in Table (5.1), with variant initial heading, where the empty *a* row represents CTRPV_EKF results, while the nonempty *a* row represents CTRA_EKF results

Table (5.2): The RMS estimation error of CTRPV_EKF , CTRA_EKF with known process and measurement variance and initial conditions of (5.1a,b) for variant initial heading

CT-CTRA synthesizing data model parameters										The estimation error RMS				
x_0	z_0	v_0	h_0	a_0	ω_0	σ_α^2	σ_J^2	σ_x^2	σ_z^2	$dist$	v	h	ω	a
50	50	20	90	2	15	2^2	2^2	2^2	2^2	1.7	5.33	3.15	6.3	
										1.695	6.03	6.3	9.4	0.327
			270							1.675	5.8	0.25	6.88	
										1.68	6.06	0.1	9.45	0.4
			270							1.762	5.2	0.35	9.11	
										1.89	5.9	0.5	9.7	3.4

As shown in Table (5.1) and Table (5.2) at zero deg and 90 deg initial heading, both CTRPV_EKF, CTRA_EKF estimated heading converges only near 0 deg with steady error. And both filters at 270 deg initial heading, the filter heading converges with 2 possibilities near 180 deg with steady error (reverse trap) or near 360 deg steady error,

noting that the reverse estimation trap does not always occur; we could say it has 50% chance with the true estimation.

Table (5.3): the RMS estimation error of CTPV_EKF with variant known process and measurement variances and initial conditions of (5.1a)

CT-CTRA synthesizing data model parameters											The estimation error RMS			
x_0	z_0	v_0	h_0	a_0	ω_0	σ_α^2	σ_j^2	σ_x^2	σ_z^2	σ_a^2	$dist$	v	h	ω
50	50	20	90	2	15	2^2	2^2	10^2	10^2	31.6^2	3.05	3.531	4.79	8.38
50	50	20	90	2	15	6^2	8^2	2^2	2^2	126.5^2	1.68	5.58	5.92	25.3
50	50	20	90	2	15	0.1^2	0.1^2	2^2	2^2	1.85^2	2.85	6.1	3.13	1.73

The experiments in Table (5.3) presents convergent estimation along all the simulation period (250 seconds). It's clear that the filter is still valid for very high measurement noise variance, with increasing estimation error due to increased measurement noise. It's also clear that the filter is still valid for very high excitation inputs noise variance, with increasing estimation error due to increased measurement noise such that's results are the more important since it proves the reliability of the estimator for practical high noisy excitation of the synthesizing dynamic model dominant in generation the states.

Table (5.4): The RMS estimation error of CTRA_EKF with variant known process and measurement variance and initial conditions of (5.1b)

CT-CTRA synthesizing data model parameters										The estimation error RMS				
x_0	z_0	v_0	h_0	a_0	ω_0	σ_α^2	σ_j^2	σ_x^2	σ_z^2	*dist.*	v	h	ω	a
50	50	20	90	2	15	2^2	2^2	10^2	10^2	2.43	1.33	2.74	7.82	0.4
50	50	20	90	2	15	6^2	8^2	2^2	2^2	3.35	6.6	7.89	18.26	1.5
50	50	20	90	2	15	0.1^2	0.1^2	2^2	2^2	1.4	13.6	4.1	11.5	0.3

The experiments in Table (5.4) are convergent estimation along all the simulation period (250 seconds). It's clear that the filter is still valid for very high measurement noise variance, with increasing estimation error due to increased measurement noise. It is also still valid for very high excitation inputs noise variance with increasing estimation error due to increased measurement noise. That results are more important since it proves the reliability of the estimator for practical purposes since the high noisy excitation of the synthesizing dynamic model dominant in generating the states. The closure of the estimation model with the synthesizing model is passed while the estimator is still able to converge the true states.

Reverse Estimation Trap:

A critical situation of our filter which is called the reverse estimation trap is explained in Table (5.5)

Table (5.5): The RMS estimation error of reverse trapped CTRPV_EKF with known process, measurement variance and initial conditions of (5.1a)

CT-CTRA synthesizing data model parameters											The RMS estimation error			
x_0	z_0	v_0	h_0	a_0	ω_0	σ_α^2	σ_j^2	σ_x^2	σ_z^2	σ_a^2	Dist.	v	h	ω
50	50	20	180	2	15	2^2	2^2	2^2	2^2	31.6^2	1.7	148.5	179.85	10.3
50	50	20	180	2	15	2^2	2^2	2^2	2^2	31.6^2	1.75	5.121	8.25	8.88

since the true initial heading is 180 deg while it was initialized in the filter in opposite direction (0 deg), the estimated heading converged to the true heading with shift of -3.14 rad (-180 deg) in less than 5 seconds as shown in Figure (5.8).

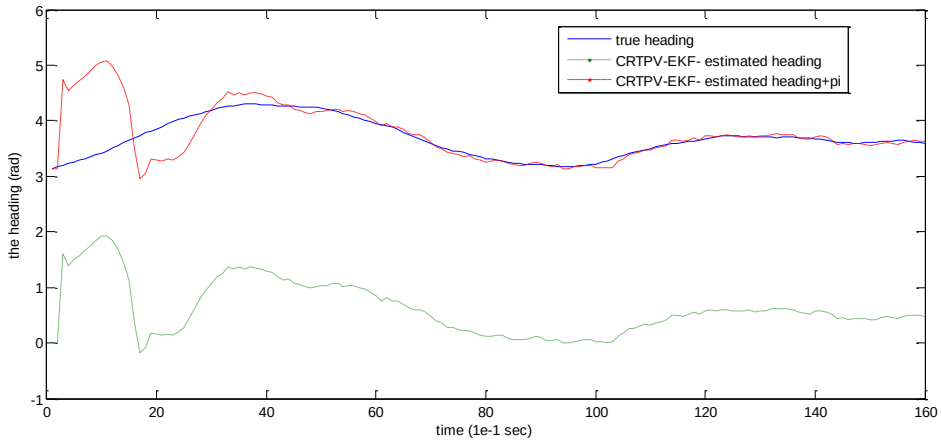

Figure (5.8): Estimated trajectory by EKF configured as in 1st row of Table (5.5)

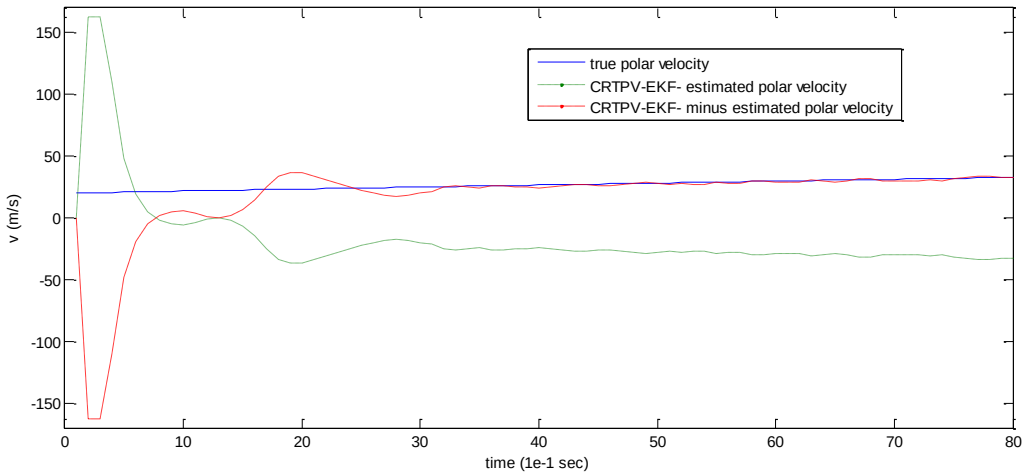

Figure (5.9): Estimated polar velocity by EKF configured as in 1st row of Table (5.5)

While the estimated velocity converges to minus the true velocity in less than 4 seconds as in Figure (5.9) and in Table (5.5). The rms of the estimation error is 148.5 m/s for the estimated but the rms for the minus estimated is 6.2 m/s, which is not steady estimation error since the estimation error dies but is generated in the first 4 seconds.

The position trajectory converges in 2 seconds with rms of 1.7 m for 250 sec simulation time, the reverse estimation trap for CTRA_EKF is illustrated in 1st row of Table (5.6).

Table (5.6): The RMS estimation error of reverse trapped CTRA_EKF with known process, measurement variance and initial conditions of (5.1b)

CT-CTRA synthesizing data model parameters										The estimation error RMS				
x_0	z_0	v_0	h_0	a_0	ω_0	σ_α^2	σ_f^2	σ_x^2	σ_z^2	Dist.	v	h	ω	a
50	50	20	180	2	15	2^2	2^2	2^2	2^2	1.67	496.63	180	6.3	3.13
50	50	20	180	2	15	2^2	2^2	2^2	2^2	1.71	5.481	8.4	8.7	0.347

since the true inital heading is 180 deg while it was initialized in the filter in opposite direction (0 deg), the estimated heading in less than 2 seconds converged to the true heading with shift of -179.85 deg (-3.139 rad). That is the rms of the estimation error for 250 sec simulation time as shown in Figure (5.10).

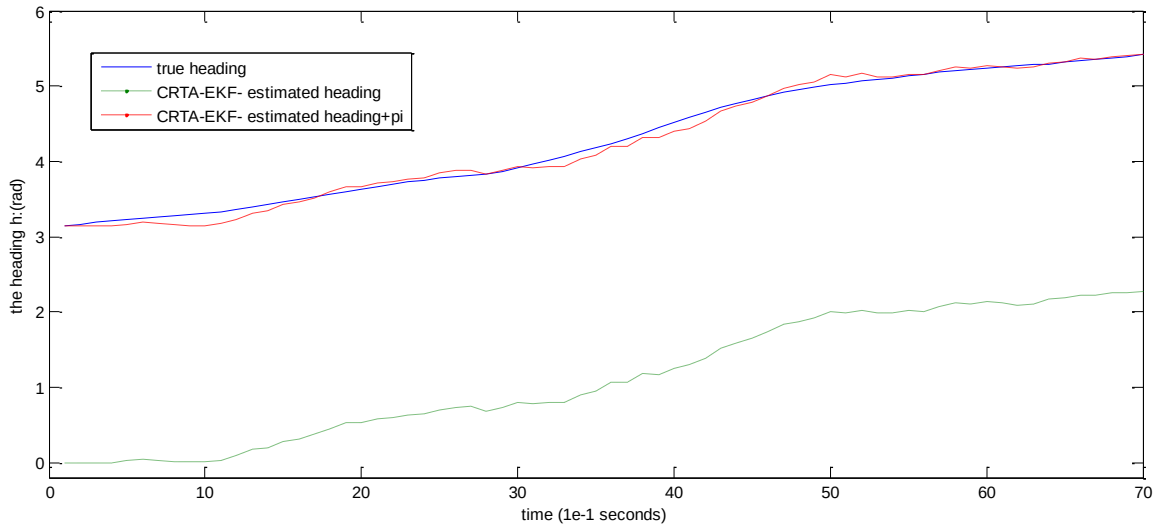

Figure (5.10): Estimated heading by EKF configured as in 1st row of Table (5.6)

The estimated velocity converges to minus the true velocity in less than 4 seconds as in Figure (5.11). Table (5.6) shows the rms of the estimation error as 496.63 m/s while the rms for the minus estimated is 7.606 m/s, which is not steady estimation error since the estimation error dies but is generated after the first 2 seconds. Thus, it is concluded that it is faster than CTRPV convergence.

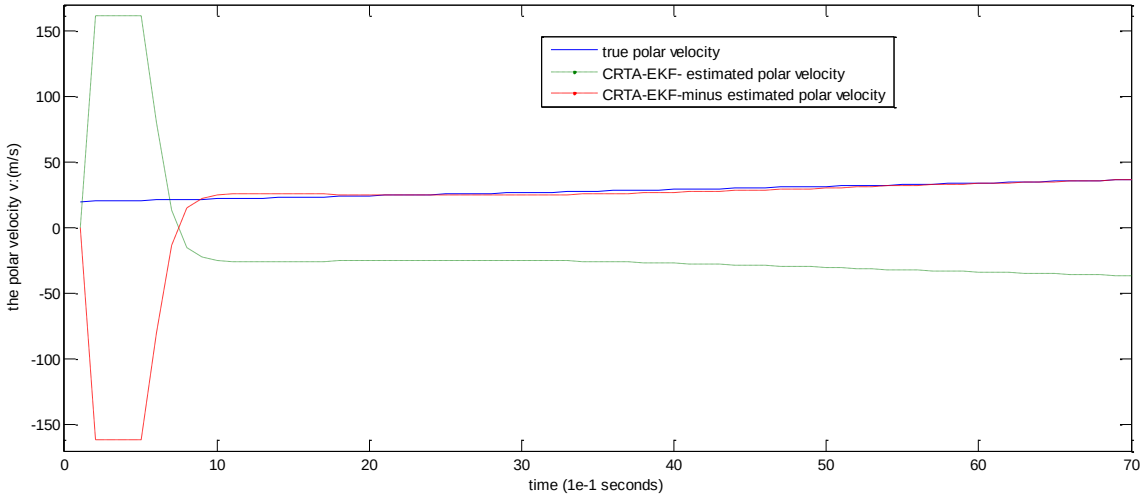

Figure (5.11): Estimated polar velocity by EKF configured as in 1st row of Table (5.6)

Also, the estimated acceleration converges to minus the true acceleration in 7 seconds as in Figure (5.12). Table (5.6) shows the rms of the estimation error is 3.13 m/s^2 while the rms for the minus estimated is 0.33 m/s^2. There is noise about true acceleration

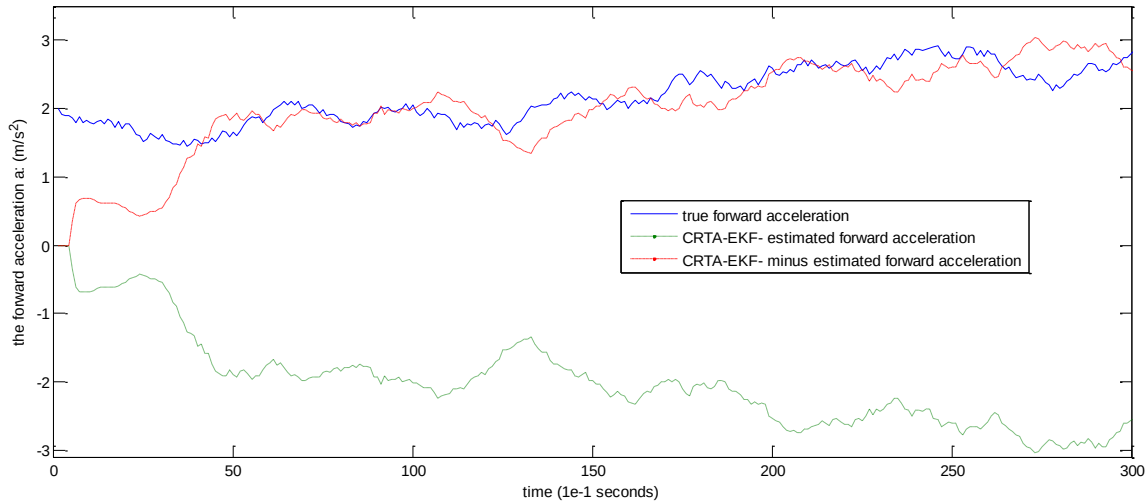

Figure (5.12): Estimated acceleration by EKF configured as in 1st row of Table (5.6)

The position trajectory converges in less than1.5 seconds with rms of 1.6704 m for 250 sec simulation time.

Its concluded that for known fully stochastic initial conditions with zero initial state estimate and known noise characteristics, the CTRPV-EKF converges very quickly (in 6 seconds at worst case) to the true states of the system. Noting that the estimated heading surely converges to the true heading or the true heading shifted by (pi rad) (the reverse direction) because of the farness of the initial estimates. If we have a near initial heading estimate, it would converge to the true heading without any shift.

5.1.1.2 Unknown stochastic initial conditions

In this case the filters have no information about the true initial states of the system model but have a knowledge of the system model and measurement noise characteristics. Thus, the filter performance is inspected with deterministic zero states initialization and deterministic zero states with the mechanical limits uncertainty initialization.

5.1.1.2.1 Zero initial conditions

The deterministic zero states initialization of the CTRPV-EKF filter are:

$$\hat{X}_{0|0} = \begin{bmatrix} \hat{x} \\ \hat{z} \\ \hat{v} \\ \hat{h} \\ \hat{\omega} \end{bmatrix}_{0|0} = \begin{bmatrix} 0 \\ 0 \\ 0 \\ 0 \\ 0 \end{bmatrix} \quad , P_{0|0} = cov \begin{bmatrix} \hat{x} \\ \hat{z} \\ \hat{v} \\ \hat{h} \\ \hat{\omega} \end{bmatrix}_{0|0} = \begin{bmatrix} 0 & 0 & 0 & 0 & 0 \\ 0 & 0 & 0 & 0 & 0 \\ 0 & 0 & 0 & 0 & 0 \\ 0 & 0 & 0 & 0 & 0 \\ 0 & 0 & 0 & 0 & 0 \end{bmatrix} \qquad (5.2a)$$

The deterministic zero states initialization of the CTRA-EKF filter are:

$$\hat{X}_{0|0} = \begin{bmatrix} \hat{x} \\ \hat{z} \\ \hat{v} \\ \hat{a} \\ \hat{h} \\ \hat{\omega} \end{bmatrix}_{0|0} = \begin{bmatrix} 0 \\ 0 \\ 0 \\ 0 \\ 0 \\ 0 \end{bmatrix} \quad , P_{0|0} = cov \begin{bmatrix} \hat{x} \\ \hat{z} \\ \hat{v} \\ \hat{a} \\ \hat{h} \\ \hat{\omega} \end{bmatrix}_{0|0} = \begin{bmatrix} 0 & 0 & 0 & 0 & 0 & 0 \\ 0 & 0 & 0 & 0 & 0 & 0 \\ 0 & 0 & 0 & 0 & 0 & 0 \\ 0 & 0 & 0 & 0 & 0 & 0 \\ 0 & 0 & 0 & 0 & 0 & 0 \\ 0 & 0 & 0 & 0 & 0 & 0 \end{bmatrix} \qquad (5.2b)$$

Figure (5.13) shows the filter configuration of zero deterministic initial conditions with known process, measurement variance and initial conditions of (5.2)

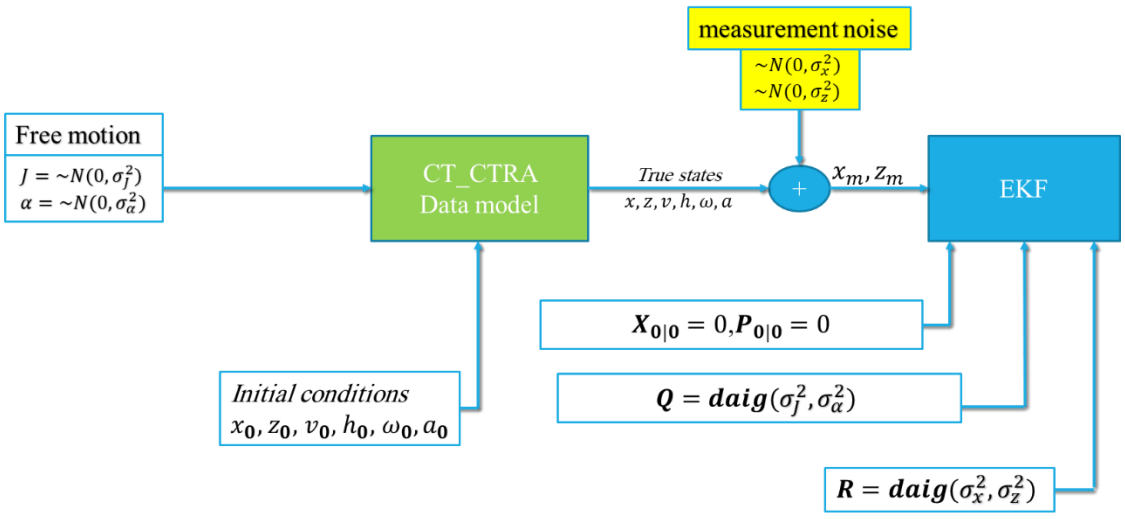

Figure (5.13): The filter configuration of zero deterministic initial conditions with known process, measurement variance and initial conditions of (5.2)

Table (5.7) inspects the performance of the deterministic zero states initialized CTRPV-EKF and CTRA-EKF for data generated by CT-CTRA model with zero initial conditions

and Gaussian noise jerk, turn acceleration of ~N(0,σ_j^2 m/s^3), ~N(0,σ_α^2 rad/s^2) provided by the measured position corrupted by Gaussian noise of ~N(0,σ_x^2 m),~N(0,σ_z^2 m/s^3), the RMS estimation error for 250 sec simulation time, where the empty *a* row represents CTRPV_EKF results, while the nonempty *a* row represents CTRA_EKF results.

Table (5.7): The RMS estimation error of CTRPV_EKF, CTRA_EKF with known variant process and measurement variance and initial conditions of (5.2a, b)

CT-CTRA synthesizing data model parameters										The estimation error RMS				
x_0	z_0	v_0	h_0	a_0	ω_0	σ_α^2	σ_j^2	σ_x^2	σ_z^2	$dist$	v	h	ω	a
0	0	0	0	0	0	3^2	3^2	3^2	3^2	1.1	1.48	6.27	11.97	
										0.79	0.94	5.96	11.88	0.4
0	0	0	0	0	0	3^2	3^2	3^2	3^2	1.59	1.9	6.4	13.4	
										0.84	1.2	2.1	11.3	4.65
0	0	0	0	0	0	1	1	3^2	3^2	1.4	1.82	18.6	6.9	
										0.63	0.3	10.3	6.2	0.16
0	0	0	0	0	0	3^2	3^2	1	1	0.69	2.23	4.6	9.37	
										0.35	0.63	4.82	9.3	0.44

For the zero initial states case, the initialization of the filters is matched with chance for trapped by reverse estimation by both filters. The estimation error's RMS is very low for the two filters. It's also noted that the CTRA-EKF estimation is closer to the true states than CTRPV-EKF especially the position trajectory and the polar velocity. In the 2nd row, the filters were trapped in reverse estimation, rms of minus v for CTRA is 0.9372 m/s, while rms of minus v for CTRPV is 3.1645 m/s.

Table (5.8): The RMS estimation error of CTRPV_EKF, CTRA_EKF with known process and measurement variance and initial conditions of (5.2a, b)

CT-CTRA synthesizing data model parameters										The estimation error RMS				
x_0	z_0	v_0	h_0	a_0	ω_0	σ_α^2	σ_j^2	σ_x^2	σ_z^2	$dist$	v	h	ω	a
10	10	5	45	0.5	3	0.05^2	0.1^2	0.8^2	1.5^2	6.69	2.45	5.82	1.56	
										6.47	2.96	10.28	2.64	0.596

Table (5.8) inspects the performance of the deterministic zero states initialization of CTRPV-EKF and CTRA-EKF for non zero initial conditions CT_CTRA generated data, figure (5.14) shows very good trajectory estimation over the whole estimation period (250 seconds) with distance error rms of 6.69 m, 6.47 m for CTRPV-EKF, CTRA-EKF respectively. To remove the pre-convergence error, the rms of the estimation error at the period from 15s to 250s is found 4.6562m, 0.8599 m for CTRPV-EKF, CTRA-EKF respectively so the CTRA is better in terms of steady error by 3.7963 m.

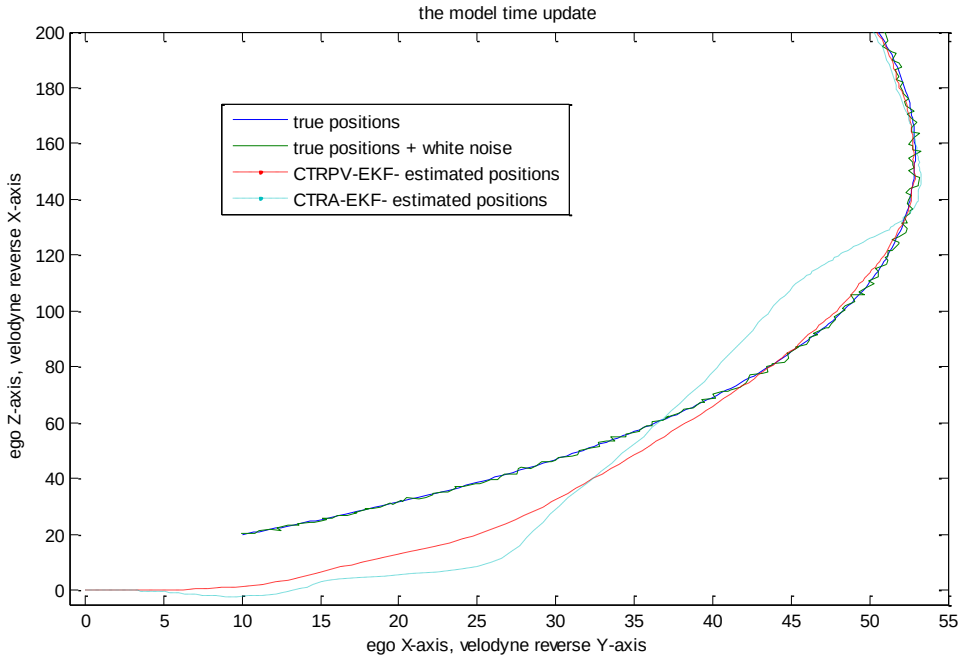

Figure (5.14): Estimated trajectory by EKF configured as in Table (5.8)

The CTRPV is faster convergent than CTRA with less overshoot for the position trajectory. Figure (5.15) shows very good heading angle estimation with RMS estimation error of 5.82 deg, 10.28 deg for CTRPV-EKF, CTRA-EKF respectively over the whole estimation period (250 seconds). That doesn't imply that CTRA-EKF is worse than CTRPV-EKF by 4.46 deg steady error. To remove the pre-convergence error, the rms of the estimation error at the period from 30s to 250s is computed as 0.9413 deg, 0.2412 deg for CTRPV-EKF, CTRA-EKF respectively. The CTRA is better in terms of steady error by 0.7001deg. However, the CTRPV is faster convergent than CTRA with less overshoot for the heading as in Figure (5.15)

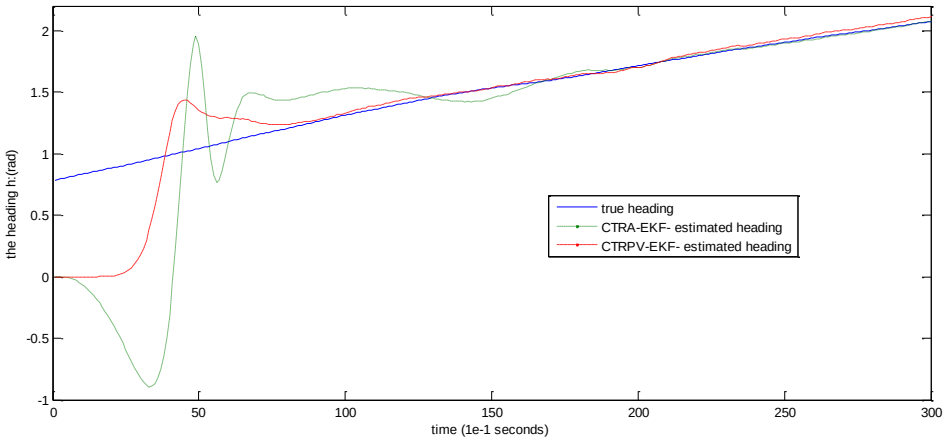

Figure (5.15): Estimated heading by EKF configured as in Table (5.8)

Figure (5.16) shows a very good polar velocity estimation with RMS estimation error of 2.45 m/s, 2.96 m/s for CTRPV-EKF, CTRA-EKF respectively over the whole estimation period (250 seconds). However, the CTRPV is faster convergent than CTRA with less overshoot but CTRPV is biased by steady error of 2.3926 m/s that is the rms of the estimation error at the period from 30s to 250s for CTRPV-EKF, while it was 0.1058 m/s for CTRA-EKF.

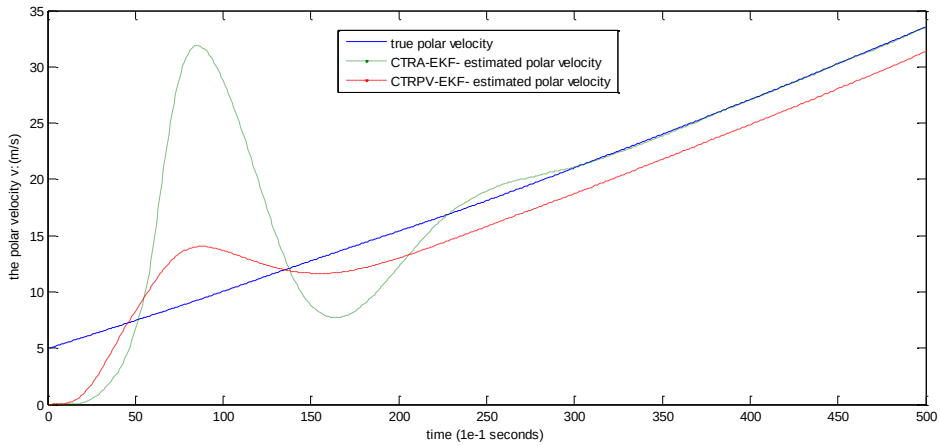

Figure (5.16): Estimated polar velocity by EKF configured as in Table (5.8)

Figure (5.17) is the estimation plot that shows very good turn rate estimation with error rms of 1.56 deg/s and 2.64 deg/s for CTRPV-EKF and CTRA-EKF respectively over the whole estimation period (250 seconds). To remove the pre-convergence error, the rms of the estimation error at the period from 30s to 250s is computed 0.393 deg/s and 0.31 deg/s. Then, the CTRPV is faster convergent than CTRA with less overshoot as shown in Figure (5.17).

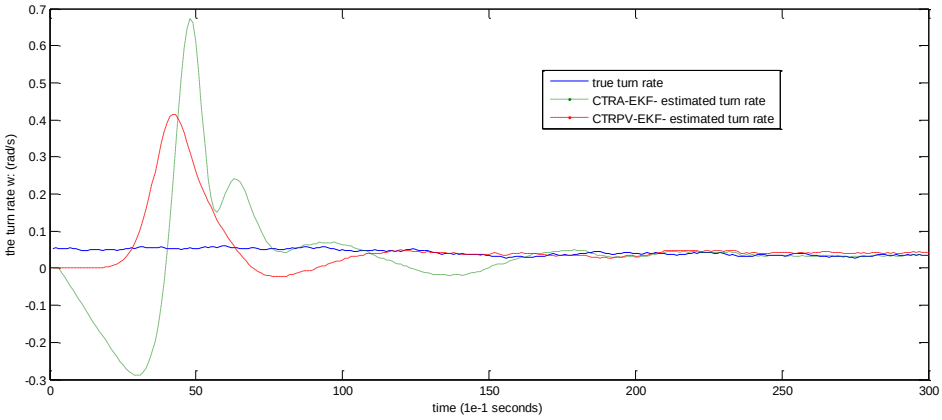

Figure (5.17): Estimated turn rate by EKF configured as in Table (5.8)

CTRA has the capability of the forward acceleration estimation as in Figure (5.18) with RMS estimation error of 0.596 m/s^2 over the whole estimation period (250 seconds). To

remove the pre-convergence error, the rms of the estimation error at the period from 30s to 250s which is compute as 0.029 m/s^2.

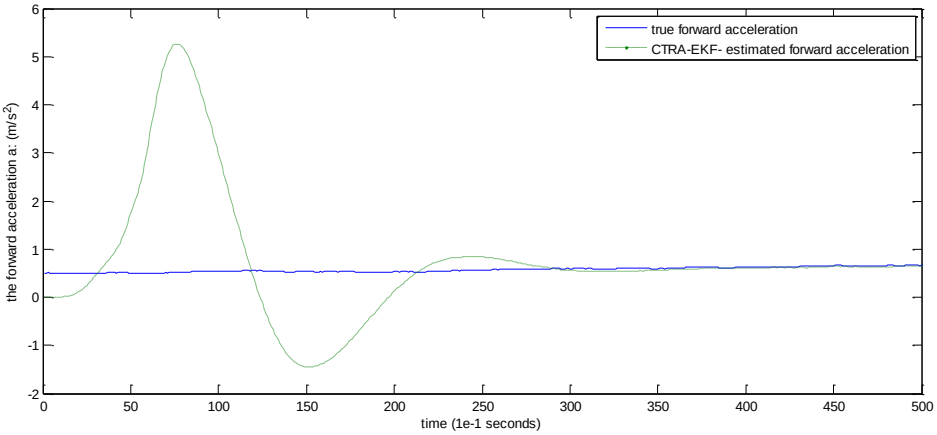

Figure (5.18): Estimated acceleration by EKF configured as in Table (5.8)

Table (5.9) shows that the filters converge well for wide range of the true initial states on the assumption of deterministic zero initial states, where the empty *a* row represents CTRPV_EKF results, while the nonempty *a* row represents CTRA_EKF results.

Table (5.9): The RMS estimation error of CTRPV_EKF, CTRA_EKF with variant known process, measurement variance and initial conditions of (5.2a, b)

CT-CTRA synthesizing data model parameters										The estimation error RMS				
x_0	z_0	v_0	h_0	a_0	ω_0	σ_α^2	σ_j^2	σ_x^2	σ_z^2	$dist$	v	h	ω	a
100	100	100	90	10	10	1	1	3^2	3^2	24.03	20.5	8.98	31.5	
										27.23	36.4	12.5	35	5.59
100	100	100	90	10	10	3^2	3^2	3^2	3^2	15.3	16	1.8	53	
										5.48	5.65	0.6	9.85	1.08
100	100	100	90	-10	-10	3^2	3^2	3^2	3^2	15.4	20.3	13.4	6.23	
										19.4	23.25	15.6	9.05	16.1

Its found that it tends to diverge for far true initial states, and when σ_x^2 *and* σ_z^2 are less than σ_α^2 *and* σ_j^2.

Its concluded that the deterministic zero states initialization is critical convergent since its stability is very sensitive for the farness of the true initial states, the system model noise, the measurement noise, and the system model noise to the measurement noise ratio. The CTRA-EKF also still proves its dominant performance especially in reduction of steady bias in the estimation of the position trajectory and the polar velocity.

5.1.1.2.2 Mechanical limitations based initial conditions

In theory, the goal of a proper stochastic model may appear to accurately model the specific types of uncertainty that exist in the system actuation and perception. Many of

the models that have proven most successful in practical applications vastly overestimate the amount of uncertainty. By doing so, the resulting algorithms are more robust to violations of the Markov assumptions, such as unmodeled state and the effect of algorithmic approximations (THRUN, Sebastian, 2005). Practically the on-road vehicles motion is mechanically limited according to the structure and the physical properties of its components, so its initial states are surely limited such that we could assume zero initial states with covariance of the square of the mechanical limits of the vehicle as the following for CTRPV

$$\hat{X}_{0|0} = \begin{bmatrix} \hat{x} \\ \hat{z} \\ \hat{v} \\ \hat{h} \\ \hat{\omega} \end{bmatrix}_{0|0} = \begin{bmatrix} 0 \\ 0 \\ 0 \\ 0 \\ 0 \end{bmatrix}, P_{0|0} = cov \begin{bmatrix} \hat{x} \\ \hat{z} \\ \hat{v} \\ \hat{h} \\ \hat{\omega} \end{bmatrix}_{0|0} = \begin{bmatrix} x_{lim}^2 & 0 & 0 & 0 & 0 \\ 0 & z_{lim}^2 & 0 & 0 & 0 \\ 0 & 0 & v_{lim}^2 & 0 & 0 \\ 0 & 0 & 0 & h_{lim}^2 & 0 \\ 0 & 0 & 0 & 0 & \omega_{lim}^2 \end{bmatrix} \quad (5.3a)$$

For CTRA

$$\hat{X}_{0|0} = \begin{bmatrix} \hat{x} \\ \hat{z} \\ \hat{v} \\ \hat{a} \\ \hat{h} \\ \hat{\omega} \end{bmatrix}_{0|0} = \begin{bmatrix} 0 \\ 0 \\ 0 \\ 0 \\ 0 \\ 0 \end{bmatrix}, P_{0|0} = cov \begin{bmatrix} \hat{x} \\ \hat{z} \\ \hat{v} \\ \hat{a} \\ \hat{h} \\ \hat{\omega} \end{bmatrix}_{0|0} \begin{bmatrix} x_{lim}^2 & 0 & 0 & 0 & 0 & 0 \\ 0 & z_{lim}^2 & 0 & 0 & 0 & 0 \\ 0 & 0 & v_{lim}^2 & 0 & 0 & 0 \\ 0 & 0 & 0 & a_{lim}^2 & 0 & 0 \\ 0 & 0 & 0 & 0 & h_{lim}^2 & 0 \\ 0 & 0 & 0 & 0 & 0 & \omega_{lim}^2 \end{bmatrix} \quad (5.3b)$$

Figure (5.19) shows the filter configuration of mechanically limited initial conditions with known process, measurement variance and initial conditions of (5.3)

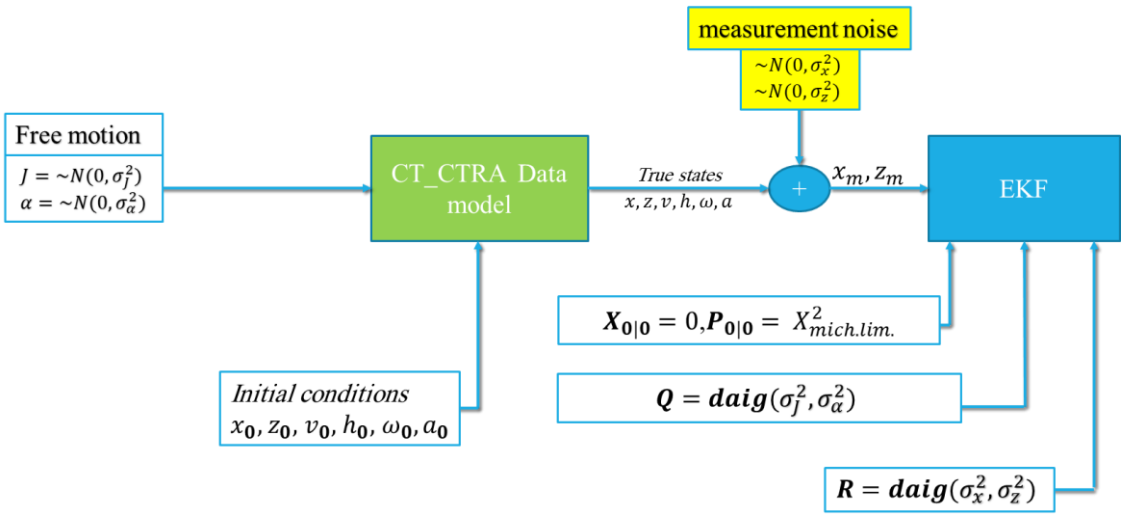

Figure (5.19): The filter configuration of mechanically limited initial conditions with known process, measurement variance and initial conditions of (5.3)

Assuming that $x_{lim}^2 = z_{lim}^2 = 100\,meter$ that is the longest distant could be efficiently recognized by the stereo system $v_{lim}^2 = 200\frac{km}{h} = 55.6^2\frac{m}{s}$ that is the maximum velocity of the observed vehicle. While assuming the vehicle motor could drive its velocity from 0 to 200 km/h in 3 seconds such $a_{lim}^2 = \left(\frac{55.6}{3}\right)^2 = 343.5\frac{m}{s^2}$, it's reasonable to set $h_{lim}^2 = \pi^2 rad = 9.8696\,rad$. Since assuming that the steering could drive the turn rate to 90 deg/s, so $\omega_{lim}^2 = \left(\frac{\pi}{2}\right)^2 rad/s = 2.4674\,rad/s$, , where the empty *a* row represents CTRPV_EKF results, while the nonempty *a* row represents CTRA_EKF results.

Table (5.10) inspects the performance of the mechanically limited full stochastic initialization of CTRPV and CTRA-EKF for zero initial state of the generation data model, where the empty *a* row represents CTRPV_EKF results, while the nonempty *a* row represents CTRA_EKF results.

Table (5.10): The RMS estimation error of CTRPV_EKF, CTRA_EKF with variant known process, measurement variance and initial conditions of (5.3a, b)

CT-CTRA synthesizing data model parameters										The RMS estimation error				
x_0	z_0	v_0	h_0	a_0	ω_0	σ_α^2	σ_f^2	σ_x^2	σ_z^2	$dist$	v	h	ω	a
0	0	0	0	0	0	3^2	3^2	3^2	3^2	1.25	2.36	13.4	12.7	
										0.88	1.07	10.9	12.24	0.73
0	0	0	0	0	0	3^2	3^2	3^2	3^2	1.11	165.7	1944	47.6	
										0.82	165.8	534.8	20.9	2.53

The RMS estimation error is very low for the both filters since the filters initial states match the true initial states. the CTRA-EKF estimation is more accurate than CTRPV-EKF especially the position trajectory and the polar velocity, with chance for trapped by reverse estimation for both filters. In the 2nd row, RMS of reversed estimated $-\hat{v}$ for CTRA is 1.124 m/s, while in CTRPV is 2.25 m/s.

Table (5.11): The RMS estimation error of CTRPV_EKF, CTRA_EKF with variant known process, measurement variance and initial conditions of (5.3a, b)

CT-CTRA synthesizing data model parameters										The RMS estimation error				
x_0	z_0	v_0	h_0	a_0	ω_0	σ_α^2	σ_f^2	σ_x^2	σ_z^2	$dist$	v	h	ω	a
10	10	5	45	0.5	3	0.05^2	0.1^2	0.8^2	1.5^2	3.01	1.57	359.6	7.6	
										2.65	1.37	8.63	1.5	0.29
50	-75	35	45	9	45	3^2	3^2	3^2	3^2	4.96	9.2	2.96	8.57	
										2.47	3.68	2.24	8.92	1.26
-50	75	-35	-45	-9	-45	3^2	3^2	3^2	3^2	5.72	11.3	2.86	9.05	
										2.1	2.05	2.48	9.99	1.05
100	100	55.6	180	18.5	90	1^2	1^2	1^2	1^2	10.7	20.4	362.1	9.19	
										4.4	7.68	359.96	11	2.75

For far nonzero initial states in

Table (**5.11**) in the 2nd and 3rd rows both filters demonstrate good estimation results with low RMS estimation error larger than twice the RMS of, where the empty *a* row represents CTRPV_EKF results, while the nonempty *a* row represents CTRA_EKF results.

Table (5.10). The results in the 1st row shows very good trajectory estimation over the whole estimation period (250 seconds) with distance error rms of 3.01 m, 2.65 m for CTRPV, CTRA-EKF respectively, indicating that CTRA-EKF is better than CTRPV-EKF by 0.36 m. To remove the pre-convergence error, the RMS estimation error at the period from 15s to 250s is computed as 2.4393 m and 0.3 m for CTRPV and CTRA-EKF respectively. Thus, the CTRA is better in terms of steady error by 2.1393m. The CTRPV is faster convergent than CTRA with less overshoot for the position trajectory as in Figure (5.20).

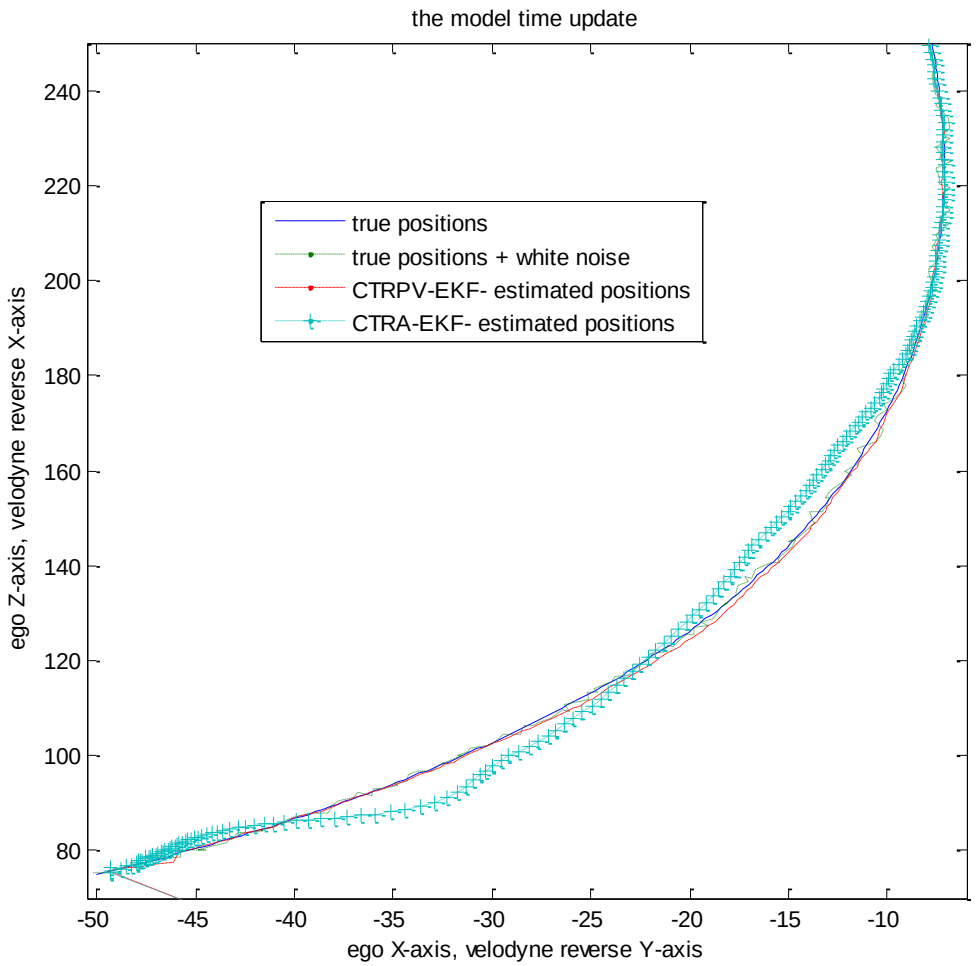

Figure (5.20): Convergence of estimated trajectory by EKF configured as in Table (5.11)

Figure (5.21) shows very good heading angle estimation with RMS estimation error of 359.6 deg and 8.63deg for CTRPV and CTRA-EKF respectively over the whole estimation period (250 seconds). To remove the pre-convergence error, the RMS estimation error at the period from 30s to 250s was compute as (359.74 = 0.26 deg) and 0.274 deg for CTRPV-EKF and CTRA-EKF respectively. The CTRA shows better steady error by 0.0119 deg. However, the CTRPV shows faster convergent than CTRA with more overshoot for the heading.

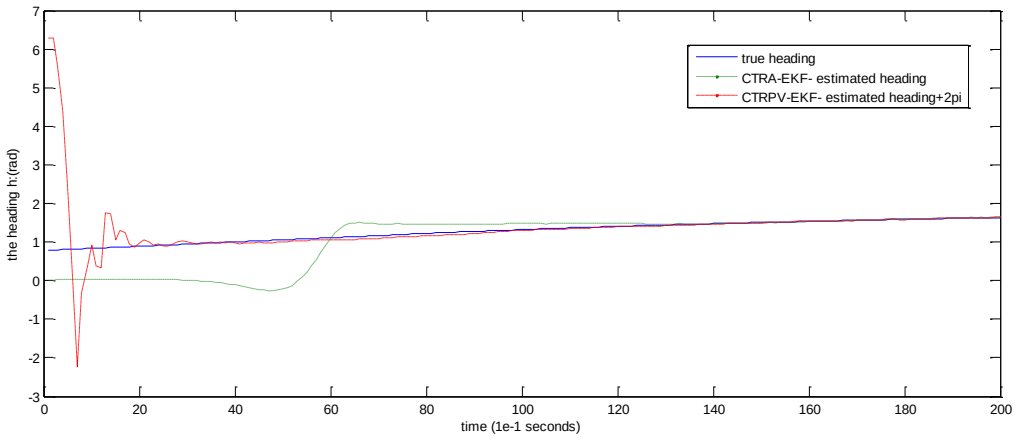

Figure (5.21): Estimated heading by EKF configured as in Table (5.11)

Figure (5.22) shows very good polar velocity estimation with RMS estimation error of 1.57m/s and 1.37 m/s for CTRPV-EKF and CTRA-EKF respectively over the whole estimation period (250 seconds). However, the CTRPV shows faster convergent than CTRA with less overshoot. CTRPV is biased by steady error of 1.5584 m/s that is the RMS estimation error at the period from 30s to 250s for CTRPV-EKF, while it was 0.0636m/s for CTRA-EKF.

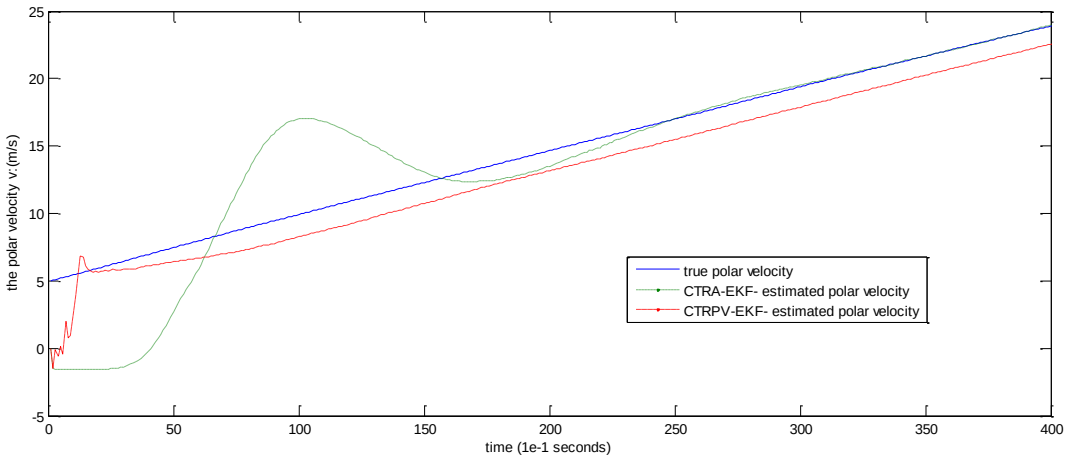

Figure (5.22): Estimated polar velocity by EKF configured as in Table (5.11)

Figure (5.23) shows very good turn rate estimation with error rms of 7.6 deg/s and 1.5 deg/s for CTRPV-EKF and CTRA-EKF respectively over the whole estimation period (250 seconds). To remove the pre-convergence error, the RMS estimation error at the period from 30s to 250s was computed as 0.3699 deg/s and 0.3137 deg/s. The CTRPV shows faster convergent than CTRA with more overshoot.

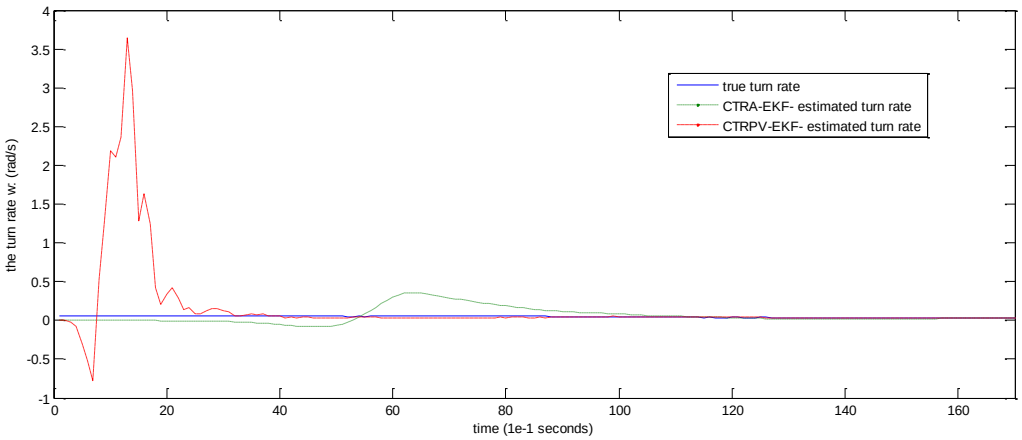

Figure (5.23): Estimated turn rate by EKF configured as in Table (5.11)

CTRA has the capability of the forward acceleration estimation as in Figure (5.24) with RMS estimation error of 0.29 m/s^2 over the whole estimation period (250 seconds). To remove the pre-convergence error, the RMS estimation error at the period from 30s to 250s was compute as 0.0195 m/s^2.

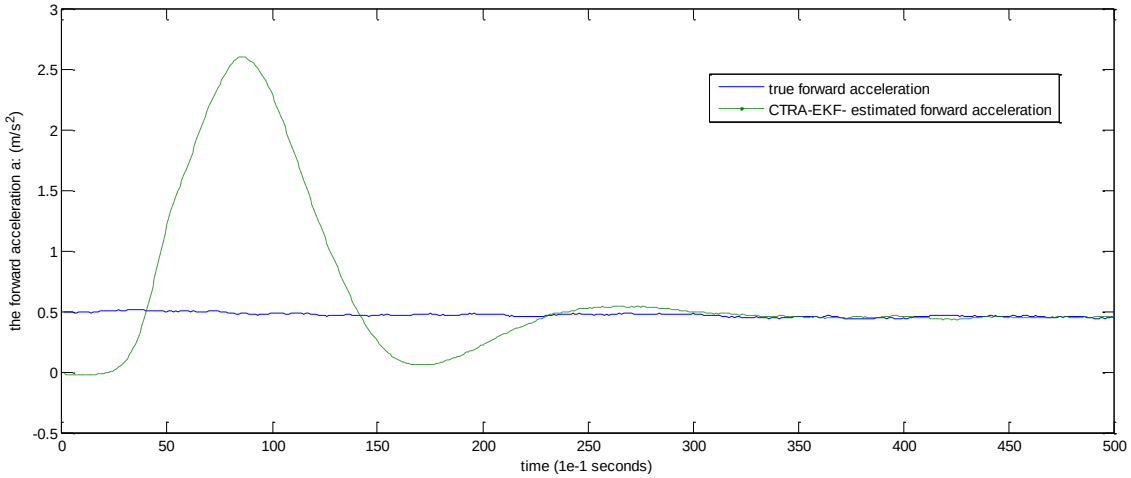

Figure (5.24): Estimated acceleration by EKF configured as in Table (5.11)

For large number of experiments for generated data in the constraint of σ_x^2, σ_z^2<100 m, σ_J^2< 15 m/s^3, σ_α^2<5 rad/s^2 , $(x_0, z_0, v_0, h_0, \omega_0, a_0) < (x_{lim}, z_{lim}, v_{lim}, h_{lim}, \omega_{lim}, a_{lim})$

Its found that the stochastic zero initial states with variance of the mechanical limitations based filters always converges to the true states, independent of the generation of the random jerk and turn acceleration.

Mechanical limited stochastic zero states initialization is clearly reliable convergent. The CTRA-EKF still proves its dominant performance especially for reduction of steady bias in the estimation of the position trajectory and the polar velocity.

5.1.2 On-road practical designed situations

In this category the motion of the observed vehicle is designed to simulate real situations of the on-road environment, by accurately choosing the model initial states and predefined jerk and turn acceleration function of time that achieve the desired motion.

So, the two major practical challenges should be faced, the first is that the period of capturing the observed vehicle through the stereo vision system is tiny doesn't succeeds few second because of the limited field of view of the stereo system (90 deg typically), and the limited recognized distance by the stereo vision system (typically 150 meters since there are not zoom), this problem needs fast convergent estimator before the vehicle departures the image plane. The second challenge is the accurate characterization of the exciting inputs $J(t), a(t), \alpha(t)$ that fits our filters process noise variances such that is the closest

$$J(t)=\sim N(0,\sigma_J^2 \text{ m/s}^3), a(t)=\sim N(0,\sigma_a^2 \text{ m/s}^2), \alpha(t) =\sim N(0,\sigma_\alpha^2 \text{ rad/s}^2)$$

For this aspect its would be discussed how to derive the maximum model variances through the analysis of mechanical limitation of the motion based on the assumption in the previous section, In order to compute the maximum σ_J^2, σ_a^2, its needed to capture the maximum positive and negative jerks and accelerations that mechanically achievable, one way to do it is to force the vehicle to achieve its acceleration limit $\left(\frac{55.6}{3}\right) m/s^2$ assharpest impulse as it could do, which could be approximated by gaussian function (3.4) in Figure (5.25)

$$a(t) = a_{lim}.e^{\frac{-(t-c)^2}{2\delta^2}} : a_{lim} = \frac{55.6}{3}, \delta = 0.5, \quad c = 5 \qquad (3.4)$$

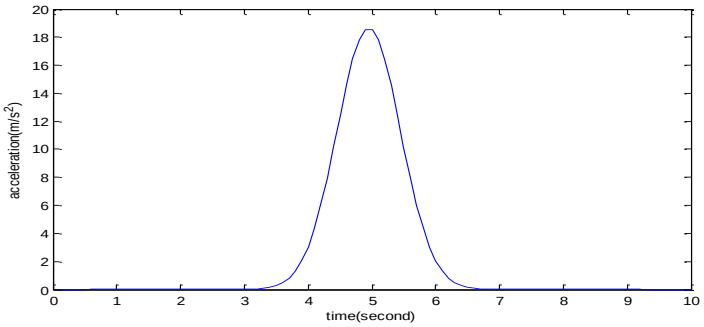

Figure (5.25): the sharpest max. achievable acceleration as in equation (3.4)

So $\sigma_a^2 = var[a(t)] = 24.85\ m/s^2$ as computed numerically by MATLAB Thus, the jerk in Figure (5.26) with computed variance $\sigma_j^2 = 61\text{m/s}^3$

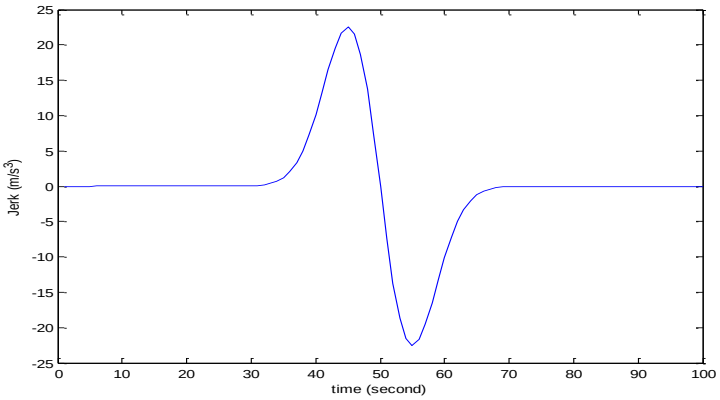

Figure (5.26): the time derivative of the acceleration in equation (3.4)

Similarly, in order to compute the maximum turn acceleration variance, it's necessary to capture the turn rate that the car could achieve its maximum turn rate as sharpest impulse which could be assumed as gaussian function (3.5) in Figure (5.27).

$$\omega(t) = \omega_{lim} * e^{\frac{-(t-c)^2}{2\delta^2}} : \delta = 0.5, \qquad c = 5 \qquad (3.5)$$

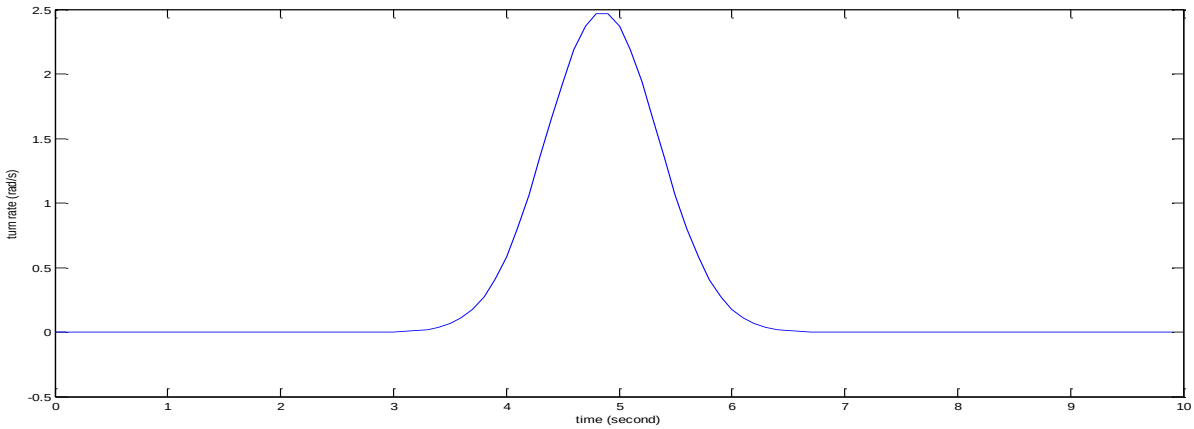

Figure (5.27): the sharpest max. achievable turn rate as in equation (3.5)

Thus, the turn acceleration function is in Figure (5.28) with variance of $\sigma_\alpha^2 == var[\alpha(t)] = 1.087\ \text{rad/s}^3$

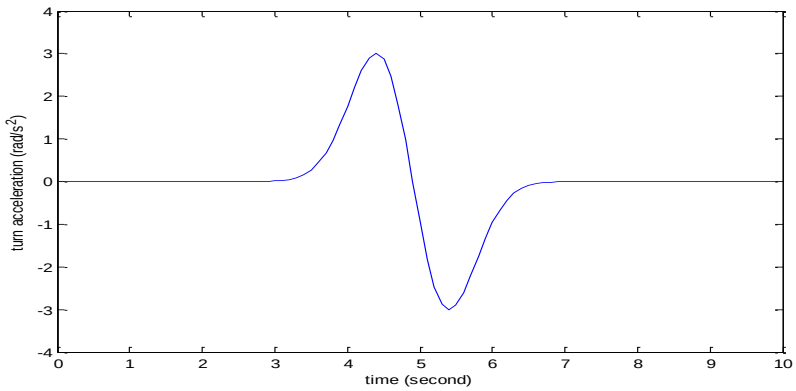

Figure (5.28): the time derivative of the turn rate as in equation (3.5)

So, the mechanically limited max. process variances for both filters are computed, and will the filters with max. process variances performance is inspected. Figure (5.29) shows the filter configuration of mechanically limited initial conditions of (5.3) with known measurement variance and unknown process variance.

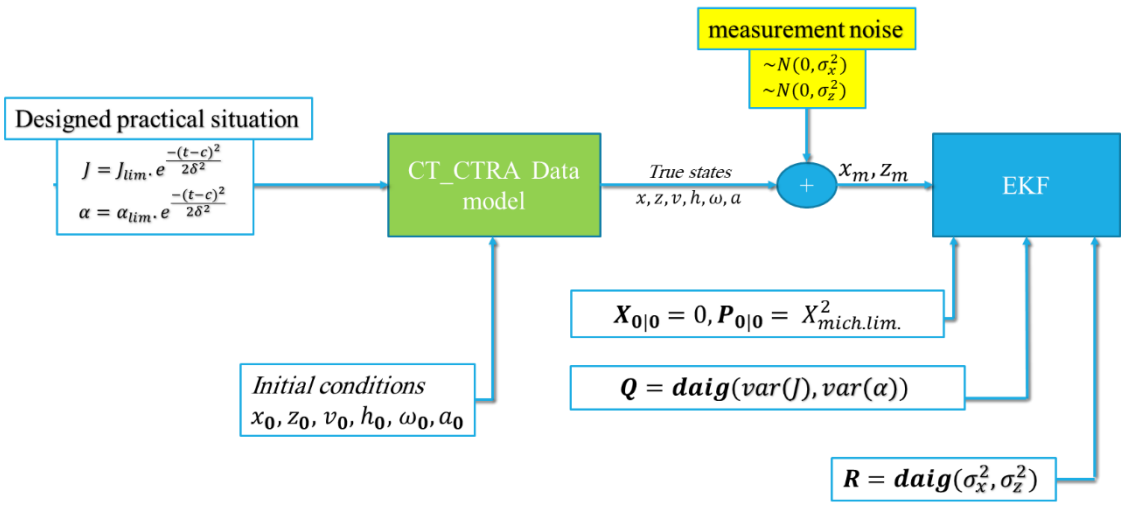

Figure (5. 29): The filter configuration of designed practical situation

5.1.2.1 left turning situation

This situation simulate a vehicle at left front of the ego at $(x_0, z_0) = (-50,20)$move forward parallel to the ego x-axis with $h_0 = 0\ deg, v_0 = 10\frac{m}{s}$, and zero ω_0, a_0, then it is turning left in an intersection urban to move forward parallel to the ego z-axis with zero exciting jerk, zero acceleration, constant velocity and the turn rate acceleration $\alpha(t)$in Figure (5.30)

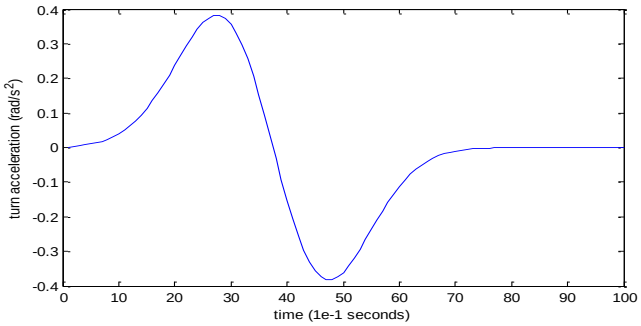

Figure (5.30): the exciting turn rate acceleration for left turning situation

The variance of the applied turn rate acceleration in figure (5.29) is computed numerically as $\sigma_\alpha^2 = 0.029\ rad/s^2$that is very small relative to the maximum mechanical that was computed in the previous section as $1.087\ rad/s^2$, and since the exciting jerk is zero, and the velocity is constant, so the actual variances $\sigma_J^2, \sigma_a^2 = 0$, so the difficulty that is facing the estimators is high, the position measurement is corrupted by gaussian noise of σ_x^2,σ_z^2 = 0.2 m, both filters are initialized by mechanical limits as in the previous section, with the maximum process variances, Table (5.12) shows the RMS estimation error for different 10 seconds simulation periods.

Table (5.12): the RMS estimation error of CTRPV, CTRA_EKF with known measurement variance, unknown process variance and initial conditions of (5.3a, b)

EKF process covariance			Sim. period	The RMS estimation error				
σ_α^2	σ_J^2	σ_a^2		$dist$	v	h	ω	a
1.087		548	10	3.52	1.6	2.35	11.5	
	61		10	3.52	1.87	3.23	5.9	1.1

The following figures shows the estimated states

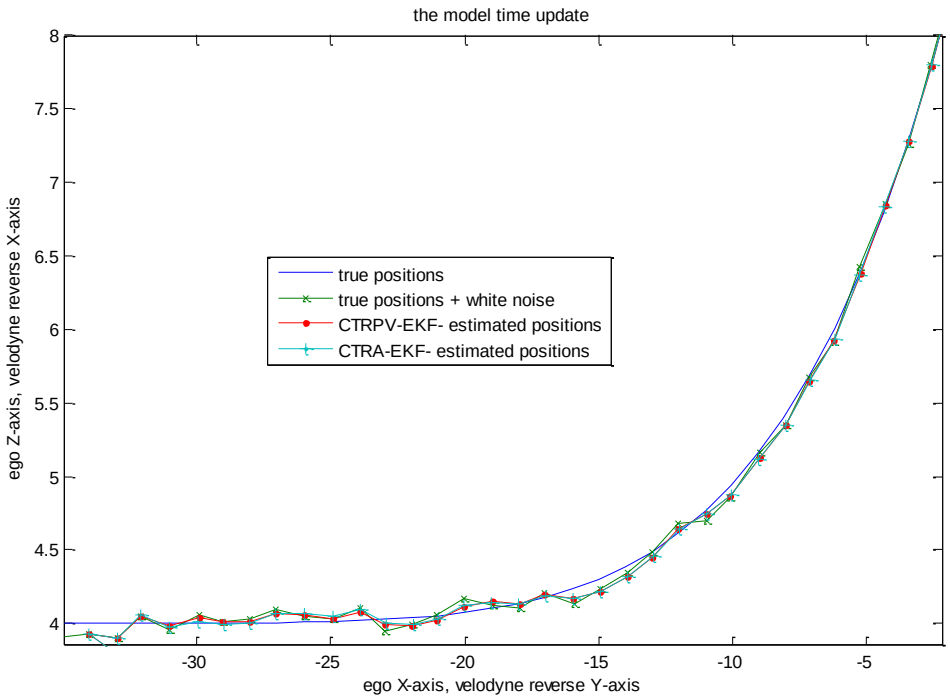

Figure (5.31): Estimated trajectory for left turning situation

In Figure (5.31), although both filters start from (0,0) position which is far from the true position they quickly capture the true trajectory with 3.52m distance error RMS for both.

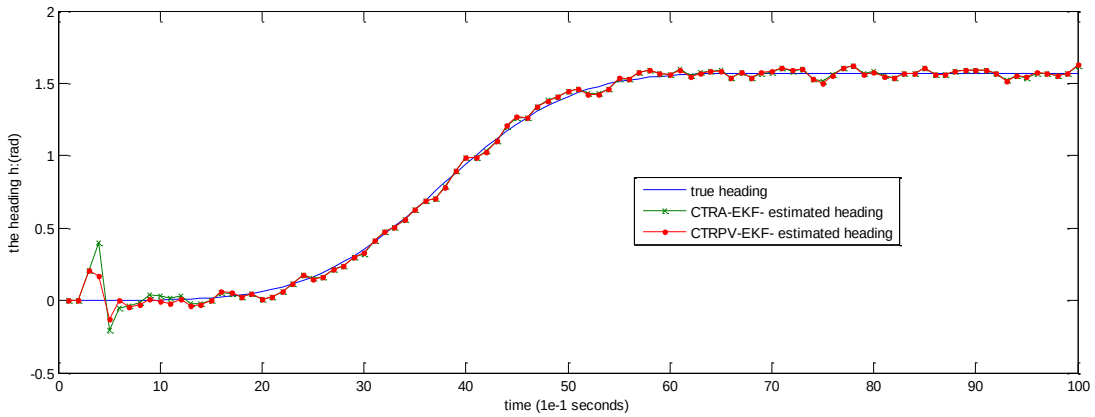

Figure (5.32): Estimated heading for left turning situation

Figure (5.32) shows good heading angle estimation by both filters, from Table (5.12) CTRA estimated heading converges to the true heading with RMS of 2.35deg, while CTRPV converges to the true heading with RMS of 3.23 deg, the polar velocity estimation in Figure (5.33),

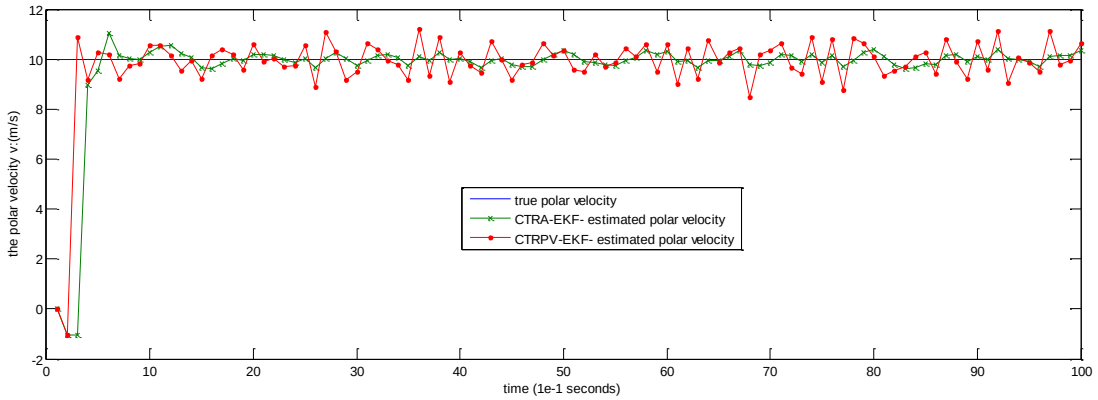

Figure (5.33): Estimated polar velocity for left turning situation

The estimated turn rate is plotted in Figure (5.34) shows alike performance of the CTRA-EKF although its rms is 5.9 rad/s while for CTRPV-EKF is 11.5 rad/s

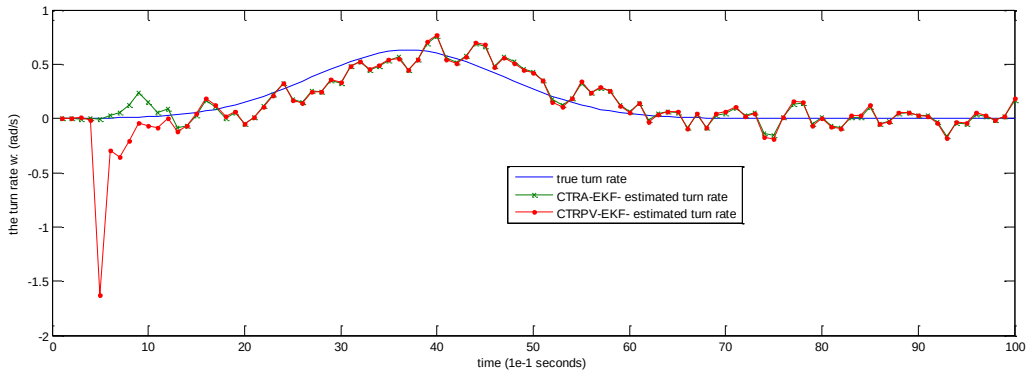

Figure (5.34): Estimated turn rate for left turning situation

The estimated acceleration in Figure (5.35) converges with rms of 1.1 m/s.

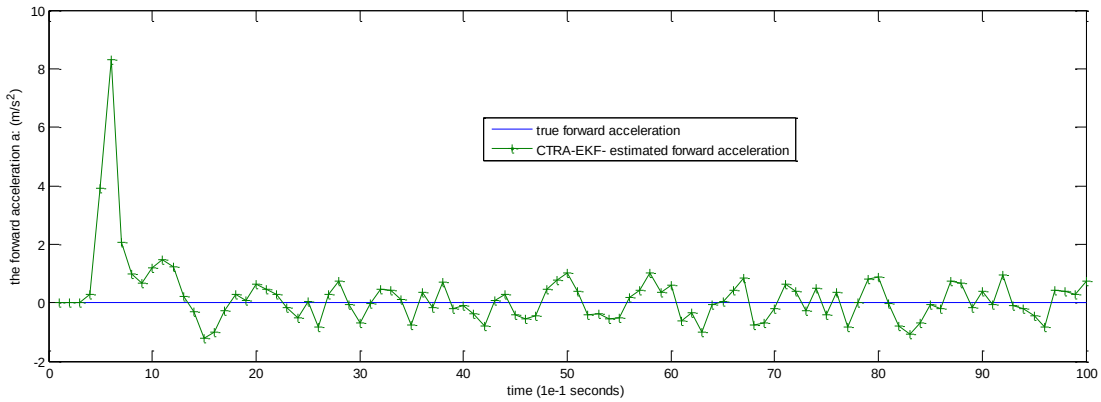

Figure (5.35): Estimated acceleration for left turning situation

Its concluded that for left turning situation both filters initialized by mechanical limited stochastic initial conditions and maximum process variances converges well and quickly with fluctuating because the process variances are too high from the true exciting inputs.

5.1.2.2 oncoming vehicle

This situation simulates straight oncoming vehicle ego from $(x_0, z_0) = (-5m, 100m)$ move towards the ego parallel to the negative ego z-axis with $h_0 = 270\ deg, v_0 = 10\frac{m}{s}$, and zero ω_0, a_0, then it with zero exciting jerk, constant velocity and zero exciting turn rate, so the actual variances $\sigma_\alpha^2, \sigma_j^2, \sigma_a^2 = 0$ that is very small relative to the maximum mechanical variances, so it shows you how the difficulty is that facing the estimators, the position measurement is corrupted by gaussian noise ofσ_x^2,σ_z^2 = 0.2 m. The two filters are initialized by mechanical limits as in the previous section, with the maximum process variances, the following Table (5.13) shows the RMS of the estimation error for different simulation periods.

Table (5.13): the RMS estimation error of CTRPV, CTRA_EKF with known measurement variance, unknown process variance and initial conditions of (5.3a, b) for oncoming vehicle situation

EKF process covariance			Sim time	The RMS estimation error				
σ_α^2	σ_j^2	σ_a^2		$dist$	$v, (-v)$	h	ω	a
1.087		548	50	8.95	1.197	718.7	9.4	
	61			8.95	1.23	718.6	6.7	7.2
1.087		548	20	14.15	19.84 (1.4845)	185.4	16.95	
	61			14.15	2.15	362.4	7.7	6.13
1.087		548	5	28.3	19.5 (2.19)	1228	18.3	
	61			28.3	2.24	708	4.42	3.95

It's clear that the longer simulation periods have less RMS estimation error because it's enough for convergence The following figures for 5seconds simulation

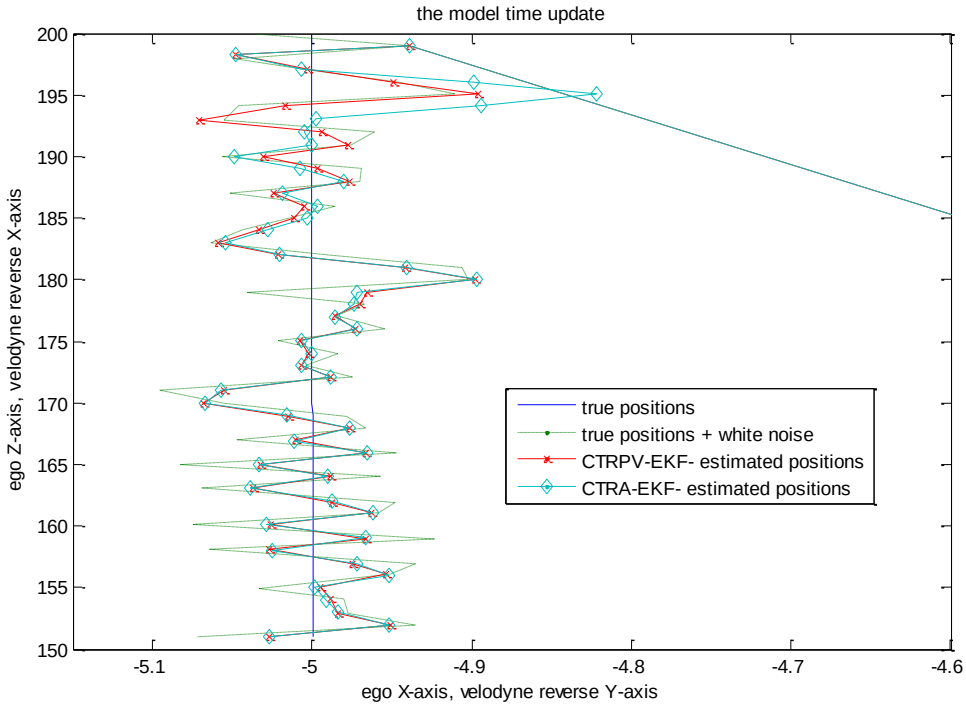

Figure (5.36): Estimated trajectory for oncoming vehicle situation

In Figure (5.36) although both filters start from (0,0) position which is far from the true position they quickly capture the true trajectory,

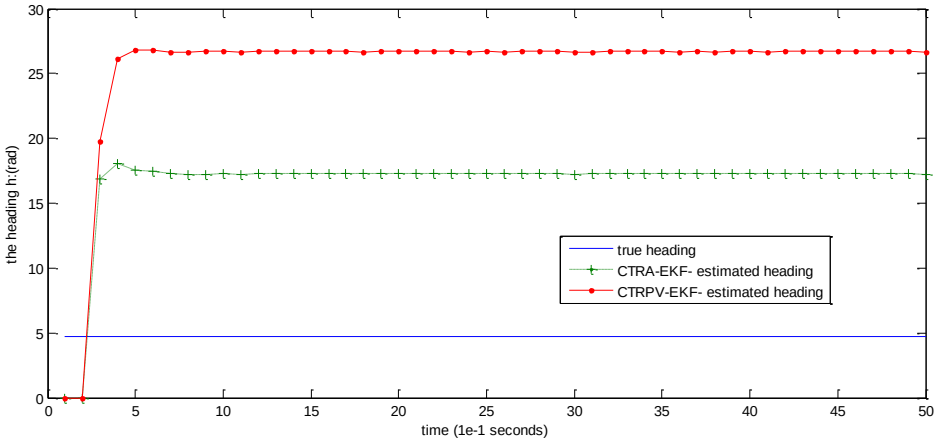

Figure (5.37): Estimated heading for oncoming vehicle situation

In Figure (5.37) CTRA estimated heading converges to 270.1 deg (990.1 deg), while CTRPV converges to 89.2deg (1529.2 deg) trapped by reverse motion estimatin, as clear

from the polar velocity estimation in Figure (5.38),

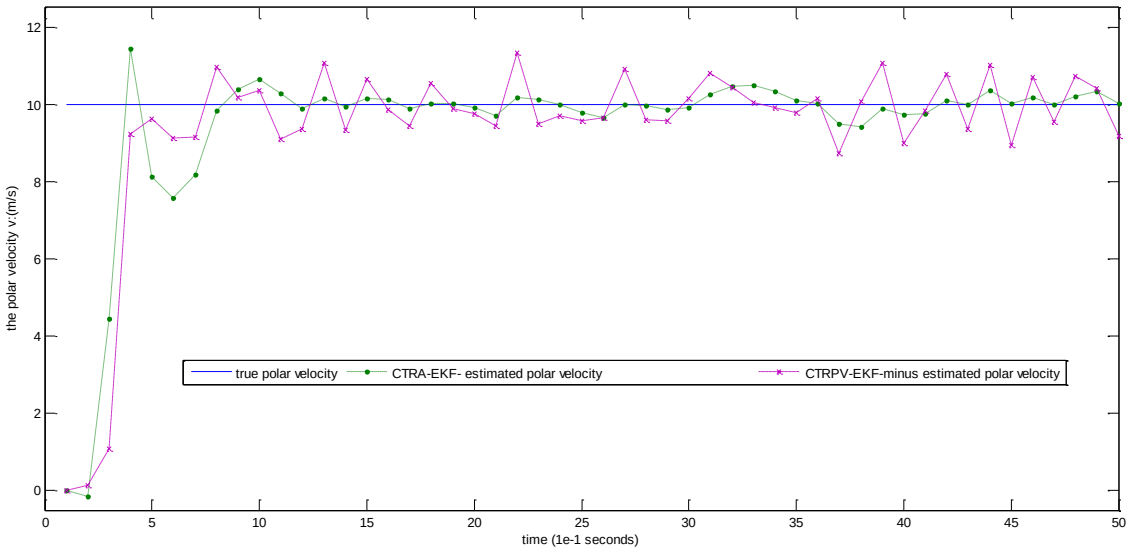

Figure (5.38): Estimated polar velocity for oncoming vehicle situation

The estimated turn rate is plotted in Figure (5.39) shows dominant performance of the CTRA-EKF since its rms is 4.42 rad/s while for CTRPV-EKF is 18.3 rad/s

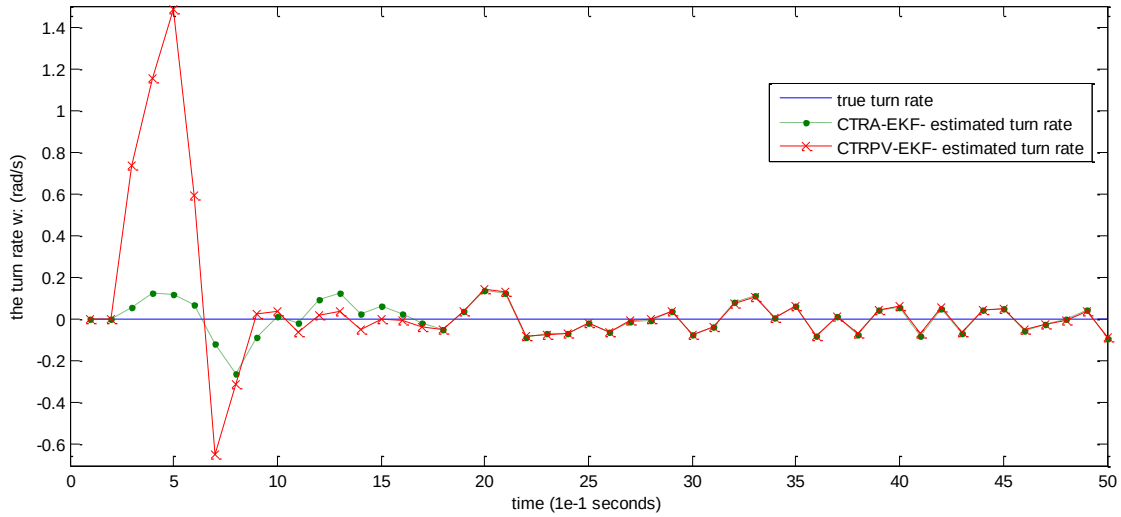

Figure (5.39): Estimated turn rate for oncoming vehicle situation

The estimated acceleration is plotted in Figure (5.40) with rms of 3.95 m/s.

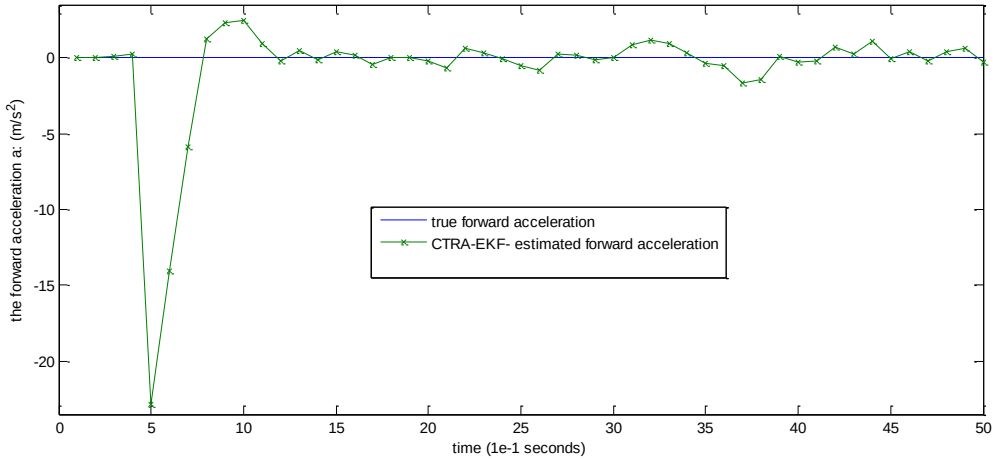

Figure (5.40): Estimated acceleration for oncoming vehicle situation

Its concluded that for oncoming vehicle situation both filters initialized by mechanical limited stochastic initial conditions and maximum process variances converges well and quickly with chance of reverse estimation trap and fluctuating because the process variances are too high from the true exciting inputs.

5.2 KITTI real dataset

The proposed estimators is applied on sample dataset from KITTI dataset represent real on-road situations for the purpose of the inspection of the reliability of the proposed estimation EKFs and the evaluation of its performance in realistic situations.

As explained in sections 3.3.1 and 3.3.2 the reference data is extracted from the velodyne laser scanner (x, y, rz) from the tracklet for the 1st dataset, but manually for the 2ndapplying the necessary processing like transformation from the observed vehicle the centroid to the rear or front center according the visible scene of the car equations (3.26-28, and transformation from laser scanner coordinates into the left camera coordinates, equations (3.29).

I prepare the stereo observations through finding manually the projection of the rear or front center point of the car in the left camera (ul, vl), using the disparity function by MATLAB to find its disparity (d) with the right camera, so we use (ul, d) to extract the measured (x, z) and applying the proposed filters. This test data classified in road category by KITTI, under the name of (2011_09_26_drive_0029) in (1.7 GB), it consists of 436 frames in period of (00:43 minutes) with image resolution of 1392 x 512 pixels, it captures 3 Cars, and , 1 Trucks, we interested the second car captured in frames 118 to 172 in 54

frames (00:54 minute), such that the observed vehicle is black Skoda that pass the ego from right straight forward in the same road faster than the ego, as in Figure (5.41)

Figure (5.41): four picked frames from test no.1 scenario

The mechanically limited full stochastic initialization in equations (3.3a, b) is used, for $x_{lim}^2, z_{lim}^2 = 50^2 m, v_{lim}^2 = 50^2 m/s, h_{lim}^2 = \pi^2 rad, h_{lim}^2 = \left(\frac{\pi}{2}\right)^2 rad/s, a_{lim}^2 = 18.53^2 m/s^2$, the linear measurement model noise variance assumed stationary was computed as the variance of difference between the stereo vision measures and the velodyne measures

$$\sigma_x^2 = var\left[x_{stereo} - x_{velodyne}\right] = 0.029\ m,$$
$$\sigma_z^2 = var\left[z_{stereo} - z_{velodyne}\right] = 7.568\ m \qquad (5.6)$$

Figure (5.42) plots $x_{stereo}, x_{velodyne}, z_{stereo}, z_{velodyne}$ for test no.1 data

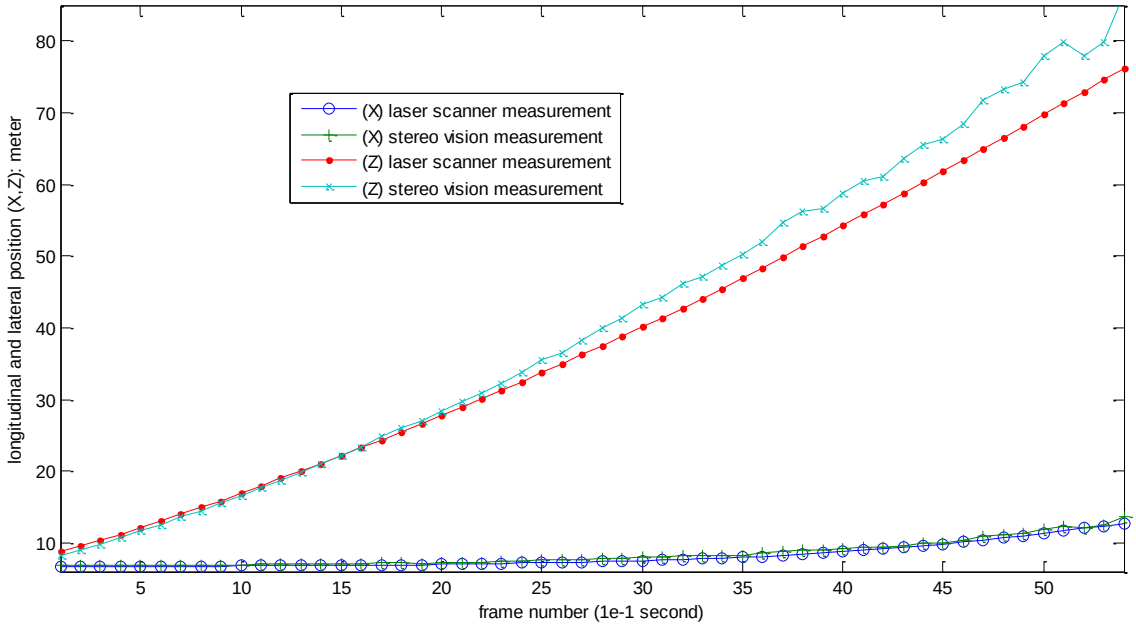

Figure (5.42): $x_{stereo}, x_{velodyne}, z_{stereo}, z_{velodyne}$ for test no.1 vs. frames

the nonlinear measurement model noise variances $\sigma_{ul}^2, \sigma_d^2$ was computed as the variance of difference between the stereo vision measures and the velodyne measures

$$\sigma_{UL}^2 = var\left[UL_{stereo} - UL_{velodyne}\right] = 191.2\ pixel$$

$$\sigma_d^2 = var\left[d_{stereo} - d_{velodyne}\right] = 0.707\ pixel \qquad (5.7)$$

$$UL_{velodyne} = \frac{f_x . x_{velodyne}}{z_{velodyne}} + x_0,\ \ d_{velodyne} = \frac{f_x . b}{z_{velodyne}} \qquad (5.8)$$

Figure (5.43) and Figure (5.44) plots $UL_{stereo}, UL_{velodyne}, d_{stereo}, d_{velodyne}$ for test no.1

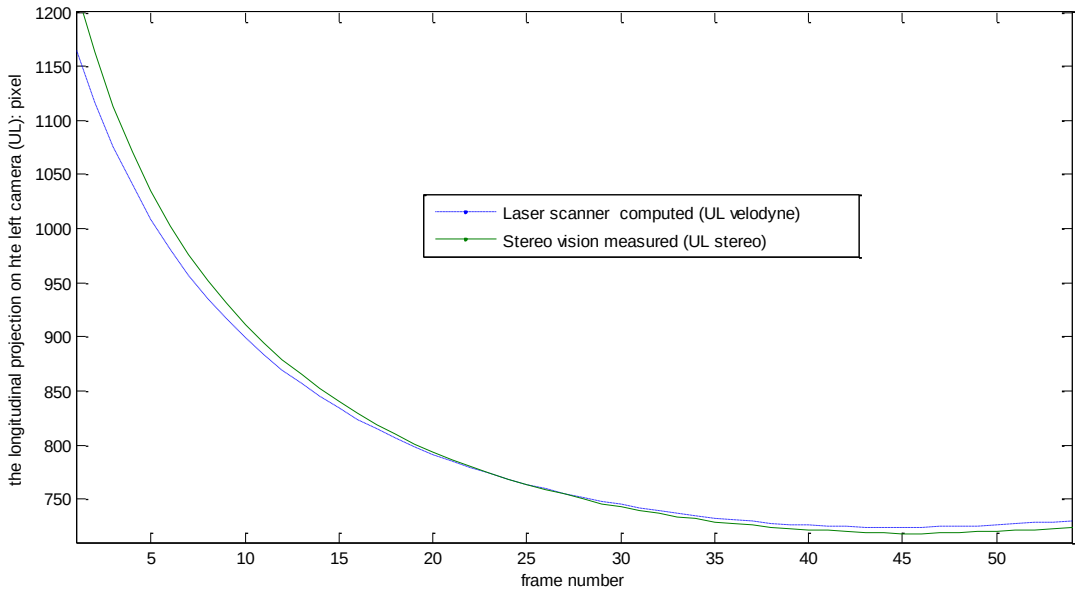

Figure (5.43): $UL_{stereo}, UL_{velodyne}$ for test no.1 along frames

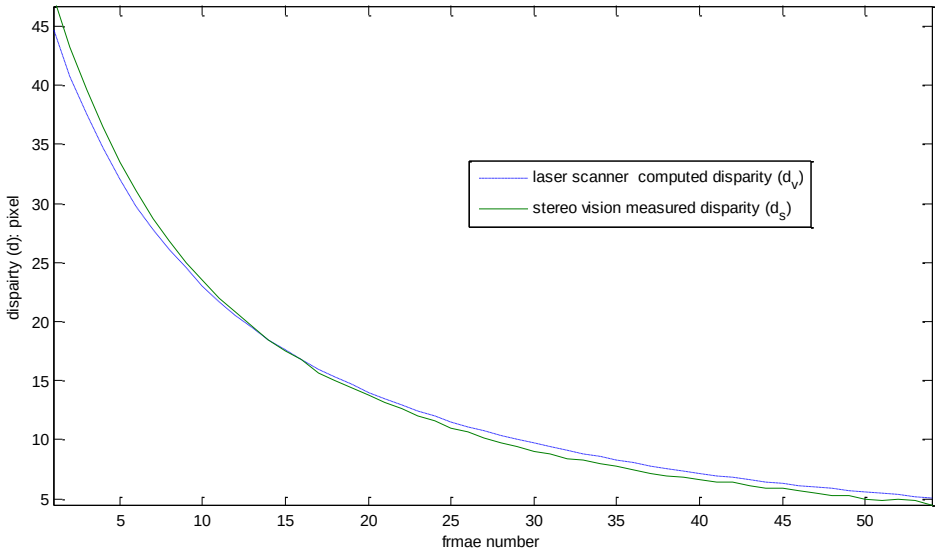

Figure (5.44): $d_{stereo}, d_{velodyne}$ for test no.1along frames

Also, the maximum process variances developed in section 5.1.2 is used,

$$\sigma_\alpha^2 = 1.087 \frac{rad}{s^2}\,, \qquad \sigma_J^2 = 61 \frac{m}{s^3}\,, \qquad \sigma_a^2 = 548\ \frac{m}{s^2} \tag{5.9}$$

5.2.1 Linear Measurement model results

Figures (5.45 through 49) plots the estimated states by the impulse discretized process models of CTRPV and CTRA filters with mechanically limited process variance in equation (5.9), linear measurement variance in equation (5.6) and initial conditions of equations (5.3a, b), for test no.1 for 54 frames (5.4 seconds).

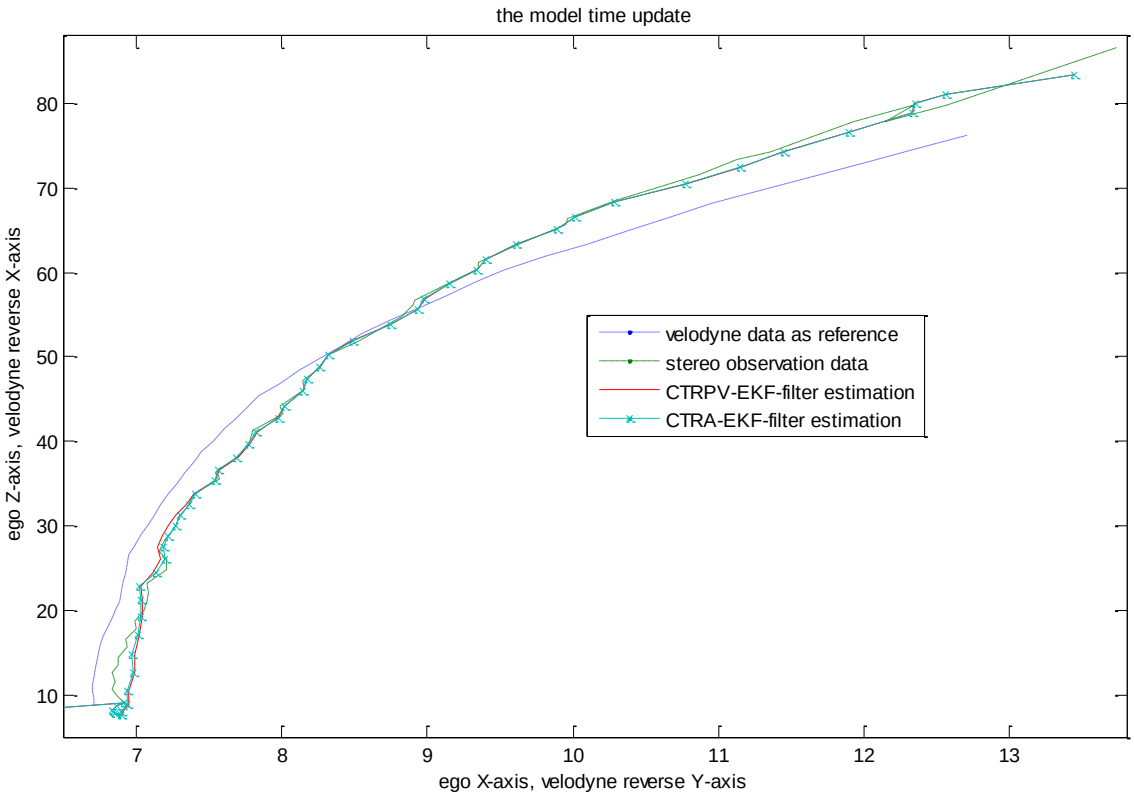

Figure (5.45): Estimated trajectory by linear measurement model for KITTI data

In Figure (5.45) although both filters start from (0,0) position which is far from the true position they quickly capture the true trajectory, the rms of lateral position x error estimation is 0.9727m, 0.9731m for CTRPV,CTRA respectively, while the rms of longitudinal position z error estimation is 4.3563m, 5.9341m for CTRPV,CTRA respectively, indicating that the rms of the distance error estimation is 4.4635m, 6.0134m for CTRPV,CTRA respectively, that is the performance of CTRPV dominants

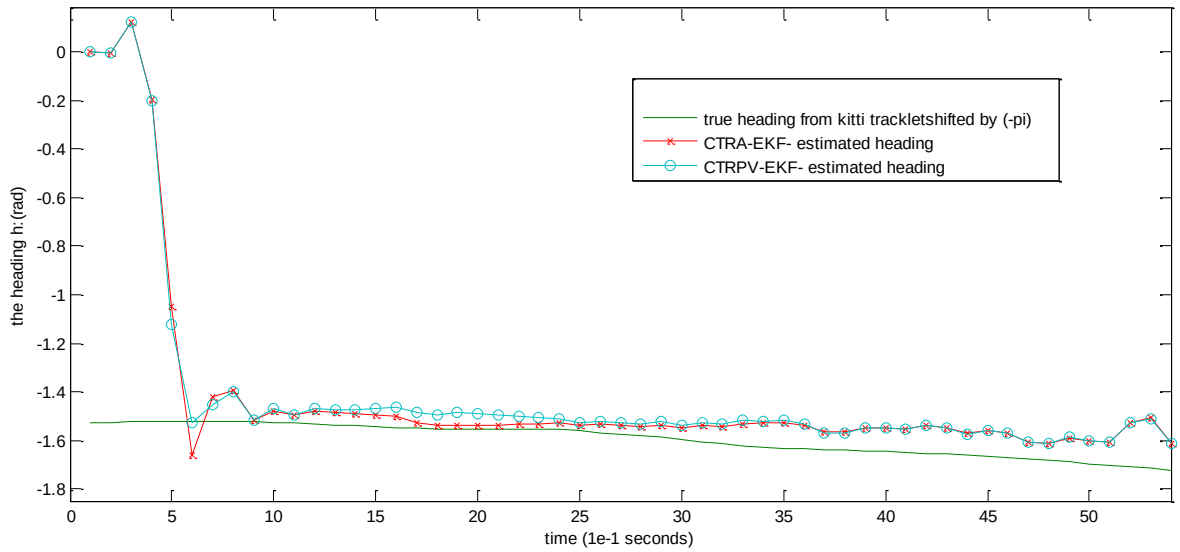

Figure (5.46): Estimated heading by linear measurement model for KITTI data

Figure (5.46) shows that CTRA estimated heading converges to the true heading shifted by $-\pi$ with total rms of 24.27 deg, while CTRPV converges to the true heading shifted by $-\pi$ with total rms of 24.21 deg that is less than CTRAbecause CTRPV converges faster than CTRA, note that the both filters is in reverse estimation trap situation, so the minus the polar velocity is the true estimation, see Figure (5.47).

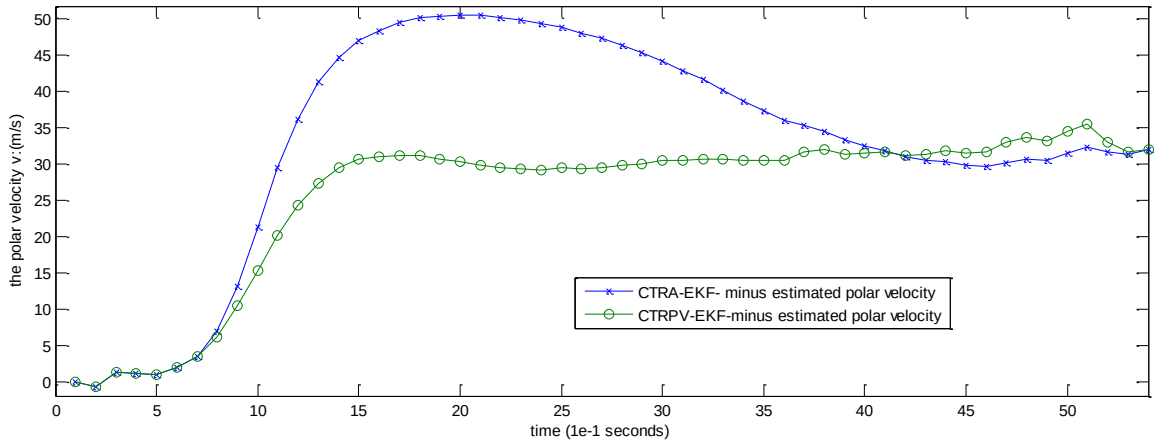

Figure (5.47): Estimated minus polar velocity by linear measurement model for KITTI data

The estimated minus acceleration is plotted in Figure (5.48).

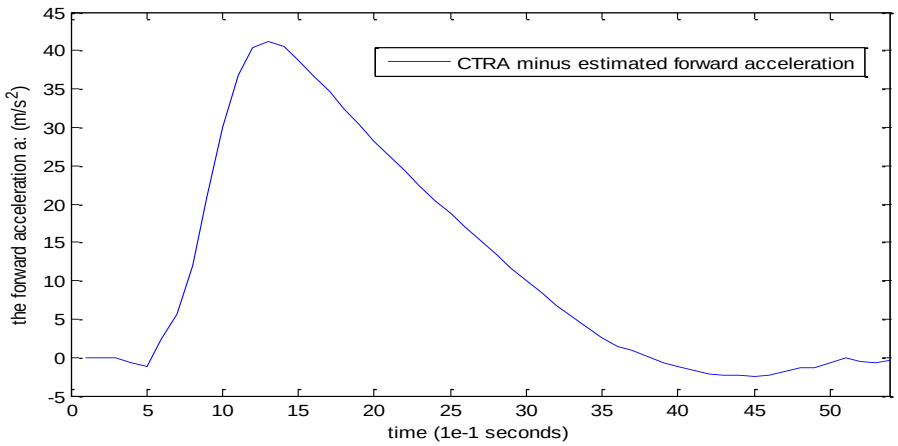

Figure (5.48): Estimated minus acceleration by linear measurement model for KITTI data

The estimated turn rate is plotted in Figure (5.49).

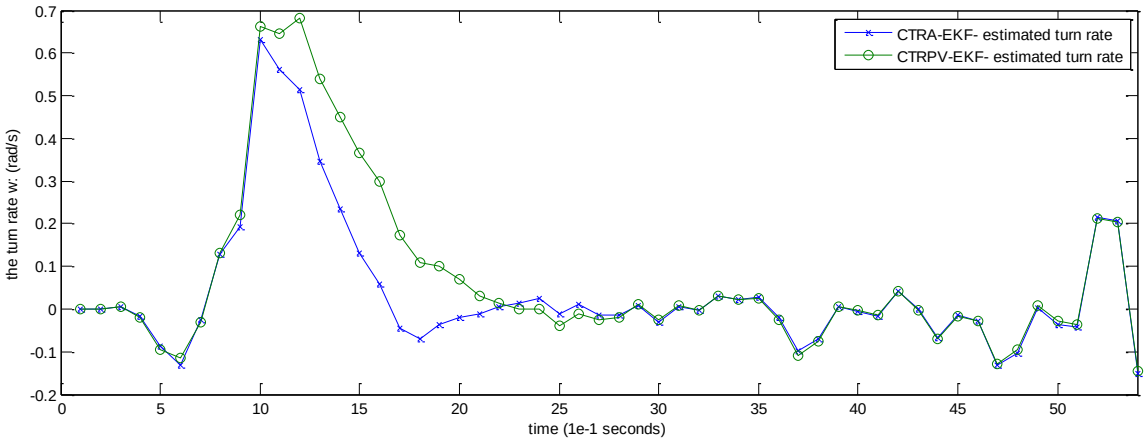

Figure (5.49): Estimated turn rate by linear measurement model for KITTI data

Applying the impulse discretized process model with linear measurement model filters with adaptive noise variances, computed as the following equations as (3.17,18)

$$\sigma_z(k) = \frac{f_x . b}{d^2(k)} * \sigma_d \qquad (5.10a)$$

$$\sigma_x(k) = \frac{(x_0 - ul(k)) . b}{d^2(k)} * \sigma_d + \frac{b}{d(k)} * \sigma_{ul} \qquad (5.10b)$$

Figure (5.50) shows that $\sigma_z(k)$ is increasing dramatically with time

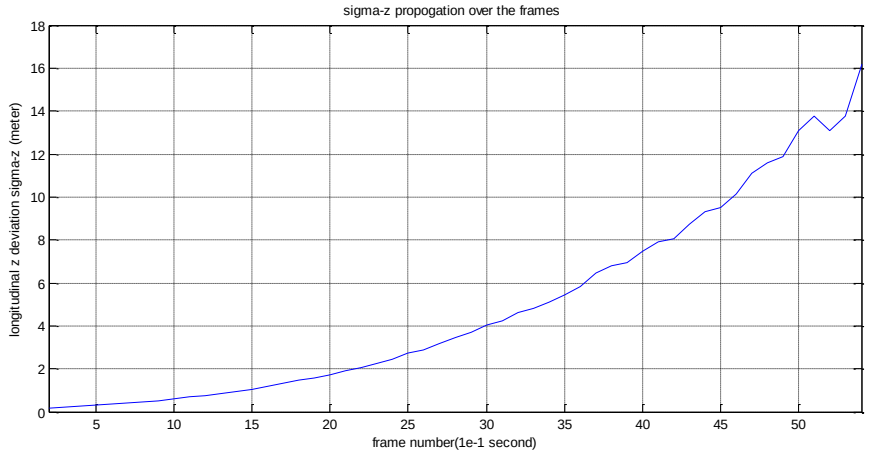

Figure (5.50): linear measurement model z_deviation for test data no.1

Figure (5.51) shows that $\sigma_x(k)$ is crossing zero at 37,38 frames

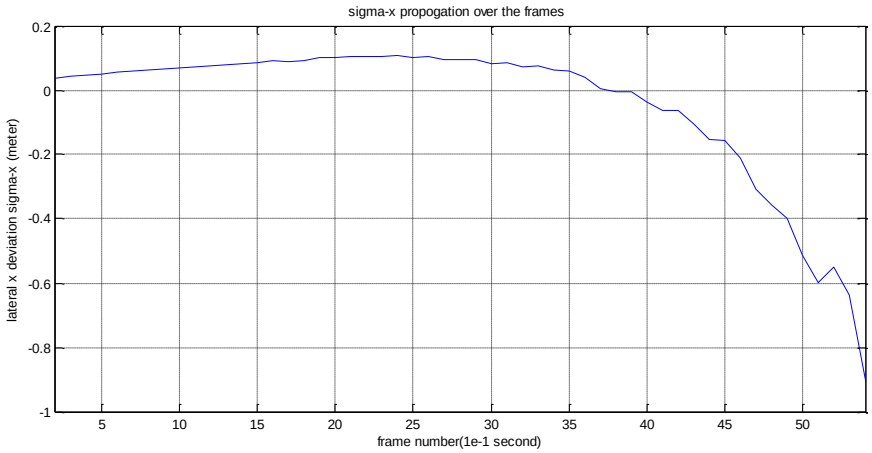

Figure (5.51): linear measurement model x_deviation for test data no.1

we have the results depicted in the following figures for 54 frames (00:54 minute)

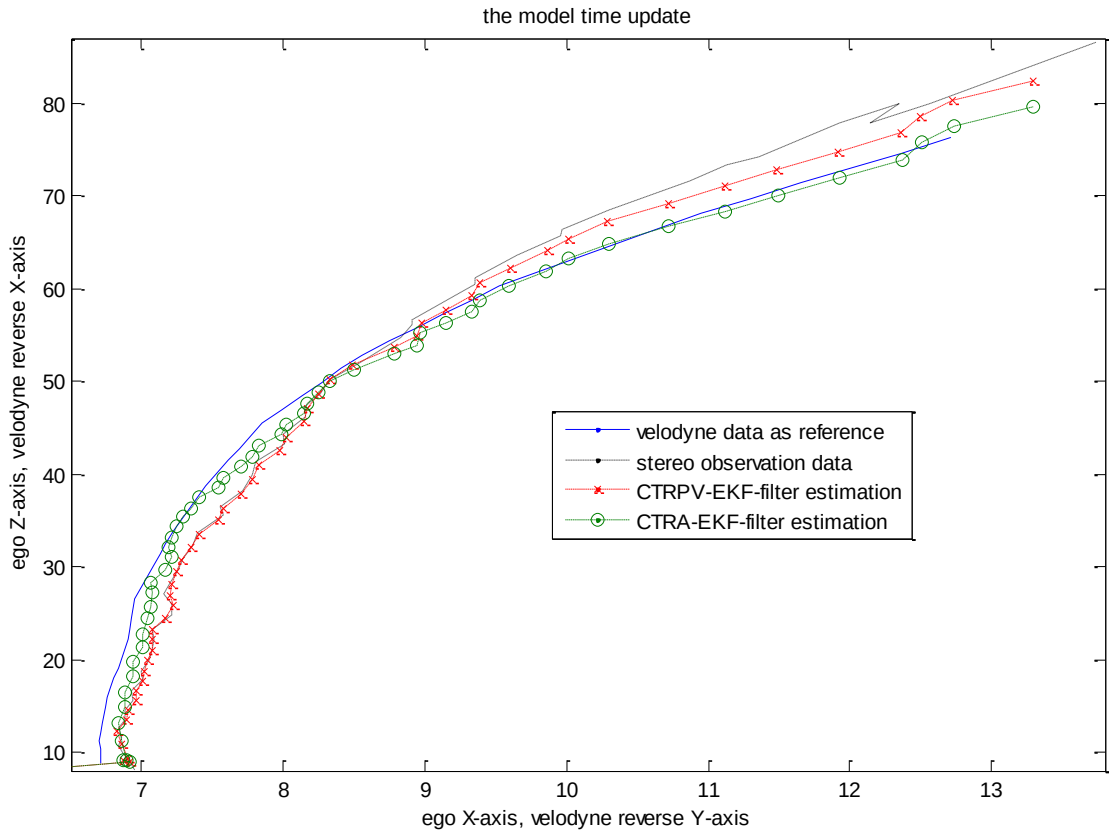

Figure (5.52): Estimated trajectory position by adaptive measurement model for KITTI data

note that CTRA filter captures the true trajectory as shown in Figure (5.52), while CTRPV still about the stereo measured trajectory, the rms of lateral position x error estimation is 0.3477 m, 0.3468m for CTRPV,CTRA respectively, while the rms of longitudinal position z error estimation is 2.8926 m, 3.5423 m for CTRPV,CTRA respectively, indicating that the rms of the distance error estimation is 2.9134 m, 3.5592 m for

CTRPV,CTRA respectively, that is the performance of CTRPV dominants, and the nonlinear measurement model dominants since its more accurate than the linear. Applying the zero-order-hold discretized process model with linear measurement model filters, we have very close results to previous.

5.2.2 Nonlinear Measurement Model Results

Figures (5.53 through 57) plots the estimated states by the impulse discretized process models of CTRPV and CTRA EKF filters with mechanically limited process variance in equation (5.9), nonlinear measurement variance in (5.7) and initial conditions equations (5.3a, b), for test no.1 for 54 frames (00:54 minute).

In Figure (5.53) both filters capture the true trajectory, the rms of x estimation is 0.3174m, 0.4355m for CTRPV,CTRA respectively, while the rms of z estimation is 3.2756m, 4.2897m for CTRPV,CTRA respectively, indicating that the rms of the distance estimation is 3.291m, 4.3118m for CTRPV,CTRA respectively, that is the performance of CTRPV dominants, and the nonlinear measurement model dominants since its more accurate than the linear.

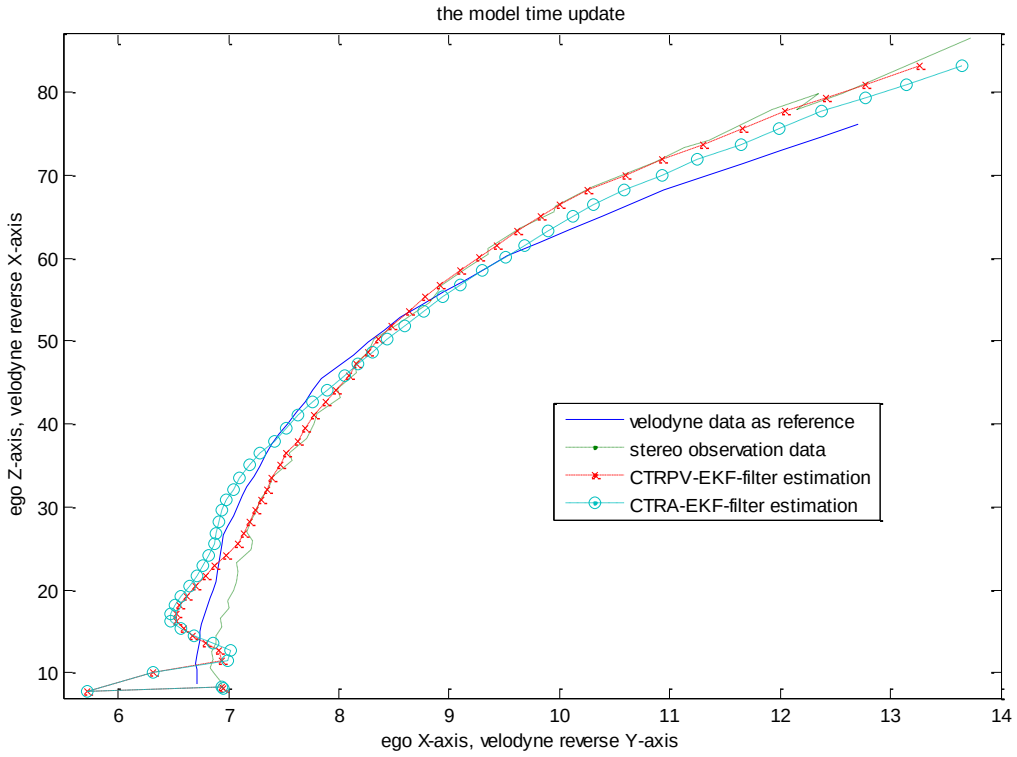

Figure (5.53): Estimated trajectory by nonlinear measurement model for KITTI data

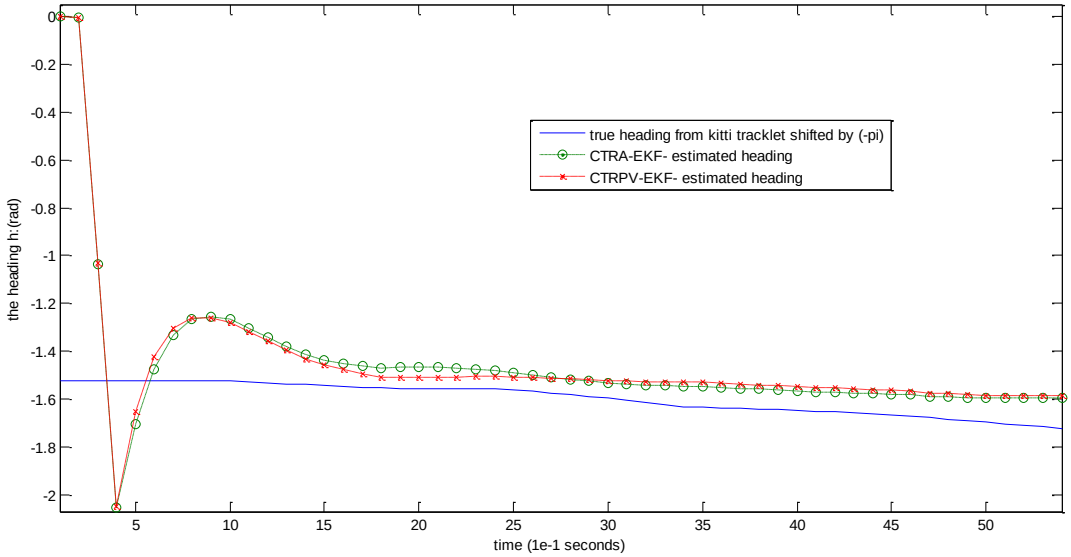

Figure (5.54): Estimated heading by nonlinear measurement model for KITTI data

In Figure (5.54) CTRA estimated heading converges to the true heading shifted by $-\pi$ with total rms of 18.88 deg, while CTRPV converges to the true heading shifted by $-\pi$ with total rms of 18.87 deg close to CTRA, note that the both filters is in reverse estimation trap situation, so the minus the polar velocity is the true estimation as in Figure (5.55), Applying the zero-order-hold discretized process model with nonlinear measurement model filters, results were very close to impulse discretized process model

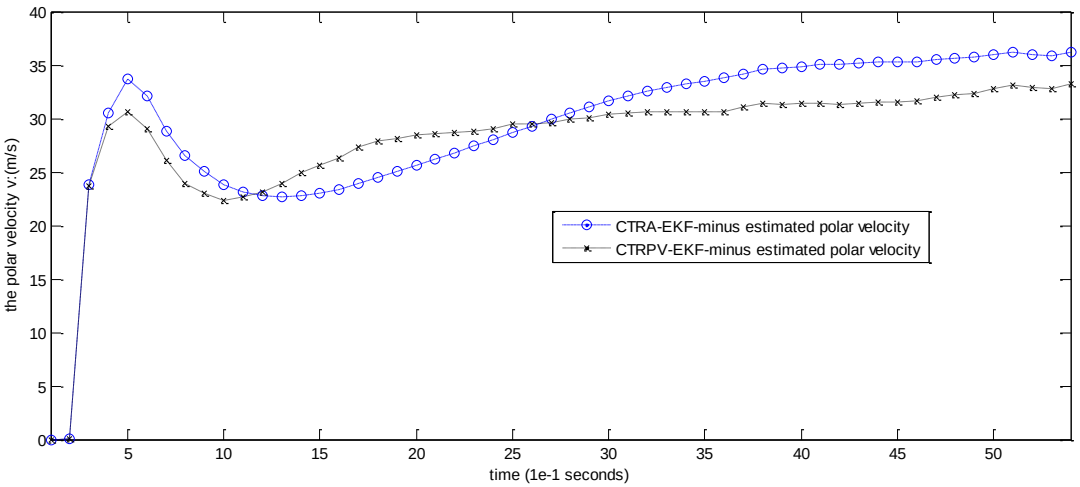

Figure (5.55): Estimated minus polar velocity by nonlinear measurement model for KITTI data

The estimated minus acceleration is plotted in Figure (5.56)

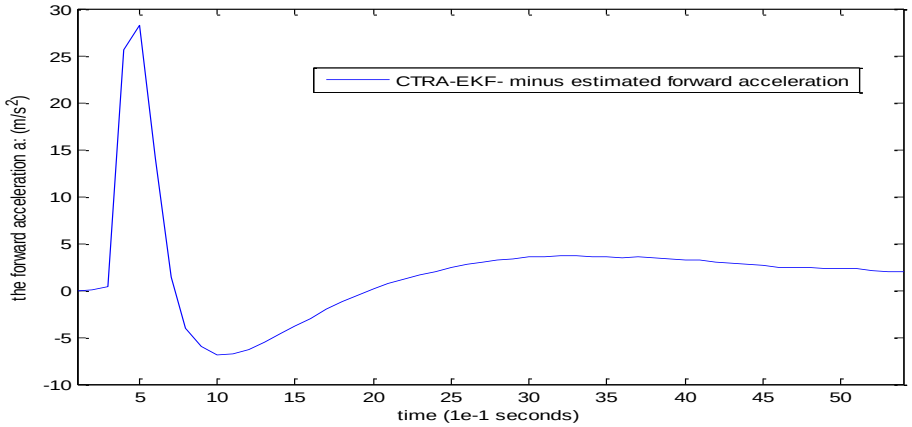

Figure (5.56): Estimated minus acceleration by nonlinear measurement model for KITTI data

The estimated turn rate is plotted in Figure (5.57).

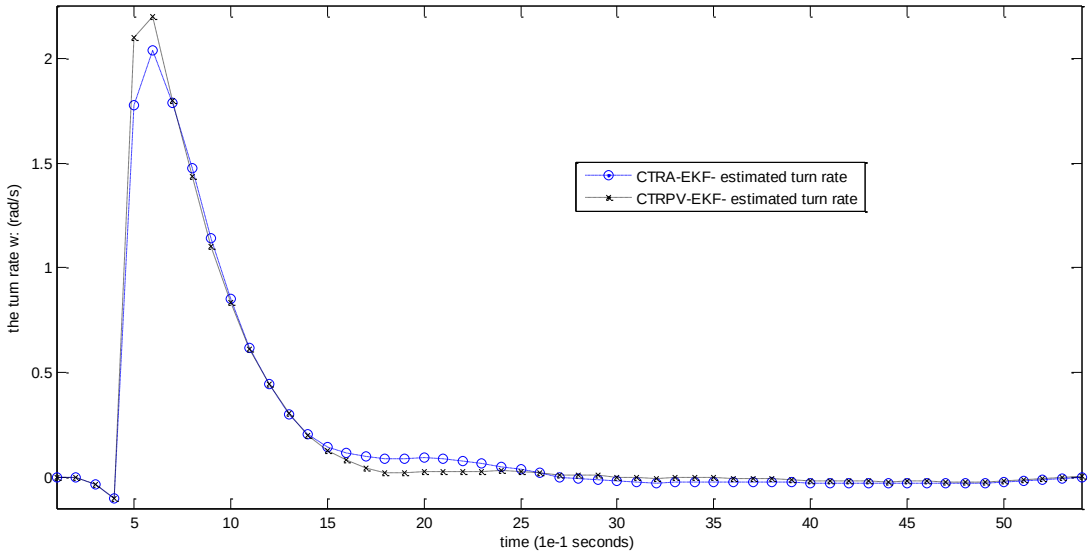

Figure (5.57): Estimated turn rate by nonlinear measurement model for KITTI data

Chapter 6

Conclusions, Recommendation and Perspectives

Chapter 6
Conclusions, Recommendations and Perspectives

6.1 General Conclusions

In this thesis, a novel approach for estimating the motion of on-road vehicles from a moving platform based on stereo image sequences by means of 1st order Extended Kalman Filter is proposed. the realistic data KITTI benchmark is suitable for our work since it provides accurate 3D pose for objects. The proposed simplified bicycle model based dynamic models CTRPV,CTRA shows its reliability in the estimation of the motion of the vehicle as proved by the results, those simple motion models recover the complexity of the vehicle dynamics that depends on internal parameters of the specified vehicle (such that its mass, center of gravity, dimensions, tire stiffness, road friction, aerodynamic coefficient, inertias) that are impossible to be estimated through the ego sensors and there are a lot of variants of the on-road vehicles differs in their structure and physical characteristics. The estimated states are the 2D position and orientation of an object relative to the ego-vehicle, as well as the object's, velocity, acceleration and the rotational velocity (yaw rate). The proposed linear measurement model assumes a stationary zero mean white noise results in reliable work although KITTI stereo vision system introduces nonstationary biased (nonzero mean) random process. The proposed discretization methods impulse and zero-order-hold at the 10 Hz sampling frequency of KITTI dataset doesn't show significant difference in terms of the filter performance for CTRPV, CTRA with both linear and nonlinear measurement models.

Its proved analytically and numerically that our proposed system is full observable for the on-road practical situations state subspace except for zero polar velocity of the observed vehicle. The practical issues such as the filter initialization, the numerical errors are covered fully. The overall system is systematically evaluated both on synthesized and real-world data of KITTI benchmark. The synthesized data results show that mechanically limited initial conditions and process noise variance filter accurately and fast convergent estimate the object pose and motion parameters for a very complicated situation, the experimental results show that the proposed approach is able to reliably estimate the object pose and motion parameters in a variety of challenging situations. The limits of the system are also carefully investigated.

For unknown initial states with known initial estimate variance and known noise characteristics the unconstrained synthesized data the known quick convergence with reverse estimation trap chance, the deterministic zero initial states show critical stability, the mechanical limited stochastic zero initial states is reliable convergent CTRA-EKF demonstrates faster convergence, less chance of reverse estimation trap and reduced steady estimation error of (x,z,v) than CTRPV-EKF. The designed practical situation data (left turning and front oncoming) the mechanical limited stochastic zero initial states CTRPV and CTRA-EKF and maximum process variances show fast fluctuating convergence. For KITTI benchmark, the stochastic zero initial states with mechanically limited variance, and the analyzed KITTI stereo vision measurement model noise characteristics and mechanically limited process noise variance the CTRPV and CTRA-EKF converges reliably and accurately indicating that the nonlinear measurement model performance dominants.

Its shown that the computational numeric errors at the computation of the Jacobeans and the inverse of the pre-fit residual covariance matrix S in the case of division by zero or close to singular matrix are big challenge for maintaining the estimator stability especially that require a lot of avoidance conditions.

6.2 Recommendations

It's sure that future investigation in accurate characterization of the stereoscopic vision measurement noise properties of no-stationarity, biasness, and variance determination would push forward the reliability of the stereo vision system, also the linear stereoscopic vision measurement model analysis shows zero lateral position variance σ_x at a specified parameter, that seems to give a chance of noise-by noise cancellation in our estimation system.

In the future work the reverse estimation trap could be solved by developing detection algorithm of the situation then adapted estimation to reverse the polar velocity v by changing its sign and reverse the heading by shifting ($k.\pi$: k *is integer*).

The reverse estimation could be solved by assisted initialization through the help of the driver or other program such that the algorithm could be adapted to reverse the polar velocity v by changing its sign and reverse the heading by shifting (pi rad).

The turn acceleration deviation of 2 rad/s^2 that excited the CTRA model means that the turn rate could change by 2*time rad/s (above fig). Therefore, the heading could change

by t^2rad, so there is chance of the 1 rad heading change (reverse the forward direction of the car) if constant 2 rad/s^2 turn acceleration applied for sqrt(pi) =1.7225 sec, but this is not practical situation since that is very sharp., Its concluded that for known fully stochastic initial conditions and known noise characteristics the CTRA-EKF converges faster than CTRPV-EKF to the true states of the system, noting that the estimated heading surely converges to the true heading or the true heading shifted by (pi rad) (the reverse direction) because of the farness of the initial estimates. If we have a near initial heading estimate, it would converge to the true heading without any shift. It's noted from large number of experiments that the reverse trap occurred 99% of times at beginning of the filter (bad initialization) and 1% in the middle course of filtering (rough turn = high sigma_alpha). Thus, the first problem could be solved by assisted initialization by the help of the driver or other program. While the second problem could be solved by knowing that the minus polar velocity is not on-road vehicle situation. Therefore, the algorithm could be adapted to reverse the negative v by changing its sign and reverse the heading by shifting (pi rad).

6.3 Improvements and Perspectives

The main contribution of the thesis is conquering the KITTI realistic dataset, such that that the coordinate frames were assigned, the dynamic models, measurement model were formulated, to be compatible for the estimation algorithms development and evaluation on that dataset, another advantage is that the all our implemented MATLAB functions were organized and written such that they are extendable for deployment in any other estimation algorithm, so it's ready to extend our work through applying advanced filters like unscented Kalman filter, interacting multiple models, particle filter.

There are lot variant dynamic models developed in the literature such as the coordinated turn siblings like Constant Steering Angle and Velocity (CSAV) and Constant Curvature and Acceleration (CCA), there are also another category called coordinate uncoupled models contains Constant Cartesian Velocity and Constant Cartesian Acceleration models, so it's ready to extend our work through applying all these models.

References

Geiger A., Lenz P. and Urtasun.R. (2012). Are we ready for Autonomous Driving? The KITTI Vision Benchmark Suite. *CVPR.*

Geiger A., Lenz P., Stiller C. and Urtasun R. (2013). Vision meets Robotics: The KITTI Dataset. *International Journal of Robotics Research (IJRR).*

ASIRT. (2017, 9 5). *road crash statistics*. Retrieved from Association for safe international road travel : http://asirt.org/initiatives/informing-road-users/road-safety-facts/road-crash-statistics

Badino H. (2004). A Robust Approach for Ego-Motion Estimation Using a Mobile Stereo Platform. *First Intern. Workshop on Complex Motion (IWCM04)*, (pp. 198-208). Guenzburg, Germany.

Barrois B., Hristova S., Woehler C., Kummert F. and Hermes C. (2009). 3D Pose Estimation of Vehicles Using a Stereo Camera. *Intelligent Vehicles Symposium, IEEE*, (pp. 267-272).

Bar-Shalom, Y., Li X., and Kirubarajan T. (2001). *Estimation with Applications to Tracking and Navigation.* Wiley Interscience.

Barth, A. (2010). *Vehicle Tracking and Motion Estimation Based on Stereo Vision Sequences.*

Buch N., Yin F., Orwell J., Makris D. and Velastin. S. A. (2009). Urban vehicle Tracking using a Combined 3D Model Detector and Classifier. *Conference on Knowledge-Based and Intelligent Information & Engineering Systems*, (pp. 169-176).

Schramm D., Hiller M. and Bardini R. (2014). *Vehicle Dynamics: Modeling nad Simulation.* Verlag Berlin Heidelberg: springer.

Dahlkamp H., Pece A., Ottlik A., and Nagel H. (2004). Differential analysis of Two Model-Based Vehicle Tracking Approaches. In *Lecture Notes in Computer Science* (pp. 71-78).

Dang T., Hoffmann C., and Stiller C. (2002). Fusing optical flow and stereo disparity for object tracking. *Intelligent Transportation Systems, IEEE Conference*, (pp. 112-117).

Gustafsson F. and Isaksson A. (1996). Best choice of coordinate system for tracking coordinated turns. *5th IEEE Conference on Decision and Control*, (pp. 3145 –3150).

Franke U. and Kutzbach I. (1996). Fast Stereo based Object Detection for Stop and Go Traffic. *Intelligent Vehicles Symposium, IEEE.*, (pp. 339-344). Tokyo, Japan,.

Gehrig S. and Stein F. (2007, june). Collision Avoidance for Vehicle-Following Systems. *Intelligent Transportation Systems, IEEE Transactions*, pp. 233-244.

Hahn M., Wöhler C., Einhaus J., Hermes C. and Kummert F. (2010). Tracking and Motion Prediction of Vehicles in Complex Urban Traffic Scenes. *Tagung Sicherheit durch Fahrerassistenz.*, (pp. 1-8). München, Germany.

Hartikainen J., Solin A. and Särkkä S. (2011). *Optimal Filtering with Kalman Filters and Smoothers a Manual for the Matlab toolbox EKF/UKF.*

Julier S. J. and Uhlmann, J. K. (2004). Unscented filtering and nonlinear estimation. *Proceedings of the IEEE*, (pp. 92(3):401–422).

Kalman, R. (1960). A New Approach to Linear Filtering and Prediction Problems. *Transaction of the ASME, Journal of Basic Engineering*, pp. 35-45.

Kamijo S., Matsushita Y., Ikeuchi K. and Sakauchi M. (2000). occlusion robust vehicle tracking for behavior analysis utilizing spatio-temporal Markov random field model. *Intelligent Transportation Systems, IEEE Conference*, (pp. 340-345).

Kim S., Kang J., Oh S., Ryu,Y., Kim K. and Park S. (2008). intelligent and integrated driver assistance system for increased safety and convenience based on all-around sensing. *Intelligent and Robotics System, 51*(3), 261-287.

Koller D., Daniilidis K. and Nagel H. (1993, june). Model-Based Object Tracking in Monocular Image Sequences of Road Traffic Scenes. *International Journal of Computer Vision*, pp. 257–281.

Labayrade R., Aubert D., and Tarel J. P. (2002). Real time obstacle detection in stereovision on non flat road geometry through "v-disparity" representation. *Intelligent Vehicles Symposium, IEEE*, (pp. 646-651).

Leibe B., Cornelis N., Cornelis K., and Van Gool L. (2007). Dynamic 3D Scene Analysis from a Moving Vehicle. *Computer Vision and Pattern Recognition*, pp. 1-8.

Leotta M. and Mundy J. (2007). Epipolar Curve Tracking in 3-D. *Image Processing, IEEE International Conference* , (pp. 325–328).

Liu M., Wu C., and Zhang Y. (2007). Motion vehicle tracking based on multi-resolution optical flow and multi-scale Harris corner detection. *Robotics and Biomimetics, IEEE International Conference*, (pp. 2032–2036).

Akhlaq. M. Tarek R. Bo Helgeson S., Shakshuki E. M. (2011). Designing an integrated driver assistance system using image sensors. *Springer Science+Business Media*.

Mark W. van der and Gavrila D. M. (2006). Real-time dense stereo for intelligent vehicles. *Intelligent Transportation Systems, IEEE Transactions*, pp. 38-50.

Roth M. (n.d.). *EKF/UKF Manuvering Target Tracking using Coordinated Turn Models with Polar/Cartesian Velocity.*

MIT, Team. (2007). *Team MIT. DARPA Urban Challenge Technical Paper.*

Mosabbeb E., Sadeghi M., Fathy M. and Bahekmat M. (2007). A low cost strong shadow-based segmentation approach for vehicle tracking in congested traffic scenes. *Machine Vision, International Conference*, (pp. 147-152).

Alvertos N. (1989). *Camera Geometries for Image Matching in 3-D Machine Vision.*

Pepy R., Lambert A. and Mounier H. (2006, June 13-15). Reducing navigation errors by planning with realistic vehicle model,. *in Intelligent Vehicles Symposium, IEEE*, pp. 300-307.

Rajagopalan, A. and Chellappa R. (2000). Vehicle Detection and Tracking in Video. *Image Processing, International Conference*, (pp. 351-354).

Hartley R. and Zisserman A. (2004). *Multiple View Geometry in Computer Vision.* New York: Cambridge University Press.

Schubert R. , Richter E. and Wanielik G. (2012). Comparison and Evaluation of Advanced Motion Models for Vehicle Tracking. 730-735.

Blackman S. S. and Popoli R. (1999). *Design and Analysis of Modern Tracking.* Artech House.

Särkkä S. (2007). On unscented Kalman filtering for state estimation of. *IEEE Transactions on Automatic Control, 52*(9), 1631–1641.

Sivaraman S. and Trivedi M. M. (2013, december). Looking at Vehicles on the Road: A Survey of Vision-Based Vehicle Detection, Tracking,and Behavior Analysis. *IEEE TRANSACTIONS ON INTELLIGENT TRANSPORTATION SYSTEMS*, pp. 1773-1795.

Sun Z., Bebis G. and Miller R. (2004). On-road vehicle detection using optical sensors: a review. *Intelligent Transportation Systems, IEEE Conference*, (pp. 585-590).

THRUN S. (2005). *PROBABILISTIC ROBOTICS.* Stanford ,Freiburg ,Seattle: Stanford University, University of Freiburg ,University of Washington of Washington.

Zeng Z. and Ma S. (2002). An efficient vision system for multiple car tracking. *Pattern Recognition, IEEE International Conference*, (pp. 609-612).

Appendix A: MATLAB Functions Implementation

CTRPV.m file

```
function [ x, z, v, h, w] = CTRPV( x, z, v, h, w ,dxe ,dze, dhe, dT)
if(abs(w)<1e-7;
        x =-dxe + x +dT*v*cos(h);
        y = -dze +z + dT*v*sin(h);
else
        x =-dxe + x + sin(w*dT/2)*cos(h+w*dT/2)*2*v/w;
        y = -dze +z + sin(w*dT/2)*sin(h+w*dT/2)*2*v/w;
end
        x = cosd(dhe)*x + sind(dhe)*y;
        z = -sind(dhe)*x + cosd(dhe)*y;
v  = v;
h  = -(dhe*pi/180) +h + w*dT;
w  = w;
end
```

CTRA.m file

```
function [ x,z,psi,v,w,a ] = CTRA( x,z,psi,v,w,a  ,dxe ,dze, d_psi_e,dT)
if(abs(w)<1e-7))%divide by zero prevent
   X =-dxe + x + (dT*cos(psi)*(2*v + a*dT))/2;
   Z = -dze + z + (dT*sin(psi)*(2*v + a*dT))/2 ;
else
   X =-dxe + x +((v*w+a*w*dT)*sin(psi+w*dT) +a*cos(psi+w*dT) -v*w*sin(psi) -a*cos(psi))/w^2 ;
   Z = -dze + z +((-v*w-a*w*dT)*cos(psi+w*dT) +a*sin(psi+w*dT) +v*w*cos(psi) -a*sin(psi))/w^2 ;
end
   x = cosd(d_psi_e)*X + sind(d_psi_e)*Z;
   z = -sind(d_psi_e)*X + cosd(d_psi_e)*Z;
   psi =-(d_psi_e*pi/180) + psi + w*dT ;
   v = v + a*dT;
   w = w;
   a = a;
end
```

Analytic_CTRA_JAC.m file

```
Syms ego_psiego_x1X_ovwdTpsiaZ_oego_x2
x_augemented = cos(ego_psi)*(-ego_x1 + X_o +((v*w+a*w*dT)*sin(psi+w*dT) +a*cos(psi+w*dT) -
v*w*sin(psi) -a*cos(psi))/w^2) + sin(ego_psi)*(-ego_x2 + Z_o +((-v*w-a*w*dT)*cos(psi+w*dT)
+a*sin(psi+w*dT) +v*w*cos(psi) -a*sin(psi))/w^2);
JA(1,3) = diff(x_augemented,psi);
JA(1,4) = diff(x_augemented,v);
JA(1,5) = diff(x_augemented,w);
JA(1,6) = diff(x_augemented,a);

if (w==0)
JA(1,3) = limit(JA(1,3),w,0);
JA(1,4) = imit(JA(1,4),w,0);
JA(1,5) = limit(JA(1,5),w,0);
JA(1,6) = limit(JA(1,6),w,0);
end
```

```
z_augemented =-sin(ego_psi)*(-ego_x1 + X_o +((v*w+a*w*dT)*sin(psi+w*dT) +a*cos(psi+w*dT) -
v*w*sin(psi) -a*cos(psi))/w^2) + cos(ego_psi)*(-ego_x2 + Z_o +((-v*w-a*w*dT)*cos(psi+w*dT)
+a*sin(psi+w*dT) +v*w*cos(psi) -a*sin(psi))/w^2;
JA(2,3) = diff(x_augemented,psi);
JA(2,4) = diff(x_augemented,v);
JA(2,5) = diff(x_augemented,w);
JA(2,6) = diff(x_augemented,a);

if (w==0)
JA(2,3) = limit(JA(2,3),w,0);
JA(2,4) = imit(JA(2,4),w,0);
JA(2,5) = limit(JA(2,5),w,0);
JA(2,6) = limit(JA(2,6),w,0);
end
```

JAC_CTRPV1.m file

```
function [ JA ] = JAC_CTRPV1( x1, x2, v, h, w ,ego_x1 ,ego_x2, ego_h, dT)

JA = zeros(5,5);

JA(1,1)= cosd(ego_h);
JA(1,2)= sind(ego_h);
JA(1,3) = cosd(ego_h)*sin(w*dT/2)*cos(h+w*dT/2)*2/w + sind(ego_h)*sin(w*dT/2)*sin(h+w*dT/2)*2/w;
JA(1,4) = -cosd(ego_h)*sin(w*dT/2)*sin(h+w*dT/2)*2*v/w + sind(ego_h)*sin(w*dT/2)*cos(h+w*dT/2)*2*v/w;
JA(1,5) = cosd(ego_h)*(cos(h+w*dT/2)*(-sin(w*dT/2)*2*v/(w^2)+cos(w*dT/2)*dT*v/w)-
(sin(w*dT/2)*sin(h+w*dT/2)*dT*v/w));
JA(1,5) = JA(1,5) + sind(ego_h)*(sin(h+w*dT/2)*(-
sin(w*dT/2)*2*v/(w^2)+cos(w*dT/2)*dT*v/w)+(sin(w*dT/2)*cos(h+w*dT/2)*dT*v/w));

if(w==0)
JA(1,3)  = dT*cos((ego_h*pi/180) - h);
JA(1,4)  = dT*v*sin((ego_h*pi/180) - h);
JA(1,5) = (dT^2*v*sin((ego_h*pi/180) - h))/2;
End

JA(2,1)= -sind(ego_h);
JA(2,2)= cosd(ego_h);
JA(2,3) = -sind(ego_h)*sin(w*dT/2)*cos(h+w*dT/2)*2/w + cosd(ego_h)*sin(w*dT/2)*sin(h+w*dT/2)*2/w;
JA(2,4) = sind(ego_h)*sin(w*dT/2)*sin(h+w*dT/2)*2*v/w + cosd(ego_h)*sin(w*dT/2)*cos(h+w*dT/2)*2*v/w;
JA(2,5) = -sind(ego_h)*(cos(h+w*dT/2)*(-sin(w*dT/2)*2*v/(w^2)+cos(w*dT/2)*dT*v/w)-
(sin(w*dT/2)*sin(h+w*dT/2)*dT*v/w));
JA(2,5) = JA(2,5) + cosd(ego_h)*(sin(h+w*dT/2)*(-
sin(w*dT/2)*2*v/(w^2)+cos(w*dT/2)*dT*v/w)+(sin(w*dT/2)*cos(h+w*dT/2)*dT*v/w));

if(w==0)
JA(2,3) =-dT*sin((ego_h*pi/180) - h);
JA(2,4) =dT*v*cos((ego_h*pi/180) - h);
JA(2,5) =(dT^2*v*cos((ego_h*pi/180) - h))/2;
end

JA(3,3) = 1;
JA(4,4) = 1;
JA(4,5) = dT;
```

```
JA(5,5) = 1;
end
```

JAC_CTRA.m file

```
function [ JA ] = JAC_CTRA( X_o,Z_o,psi,v,w,a ,ego_x1 ,ego_x2, ego_psi ,dT)
J_presecion = 1e-7;
JA = eye(6);
JA(1,1)= cosd(ego_psi);
JA(1,2)= sind(ego_psi);
JA(1,3) = (CTRA( X_o,Z_o,psi+J_presecion,v,w,a  ,ego_x1 ,ego_x2, ego_psi,dT) - CTRA( X_o,Z_o,psi,v,w,a
,ego_x1 ,ego_x2, ego_psi,dT))/J_presecion;
JA(1,4) =  (CTRA( X_o,Z_o,psi,v+J_presecion,w,a  ,ego_x1 ,ego_x2, ego_psi,dT) - CTRA( X_o,Z_o,psi,v,w,a
,ego_x1 ,ego_x2, ego_psi,dT))/J_presecion;
JA(1,5) =(CTRA( X_o,Z_o,psi,v,w+J_presecion,a  ,ego_x1 ,ego_x2, ego_psi,dT) - CTRA( X_o,Z_o,psi,v,w,a
,ego_x1 ,ego_x2, ego_psi,dT))/J_presecion;
JA(1,6) = (CTRA( X_o,Z_o,psi,v,w,a+J_presecion  ,ego_x1 ,ego_x2, ego_psi,dT) - CTRA( X_o,Z_o,psi,v,w,a
,ego_x1 ,ego_x2, ego_psi,dT))/J_presecion;

JA(2,1)= -sind(ego_psi);
JA(2,2)= cosd(ego_psi);

[  X_o1,Z_o1,psi1,v1,yawr1,a1 ] = CTRA( X_o,Z_o,psi+J_presecion,v,w,a  ,ego_x1 ,ego_x2, ego_psi,dT);
[  X_o2,Z_o2,psi2,v2,yawr2,a2  ] =  CTRA( X_o,Z_o,psi,v,w,a  ,ego_x1 ,ego_x2, ego_psi,dT);
JA(2,3) = ( Z_o1-Z_o2  )/J_presecion;
[  X_o1,Z_o1,psi1,v1,yawr1,a1  ] = CTRA( X_o,Z_o,psi,v+J_presecion,w,a  ,ego_x1 ,ego_x2, ego_psi,dT);
JA(2,4) = ( Z_o1-Z_o2  )/J_presecion;
[  X_o1,Z_o1,psi1,v1,yawr1,a1  ] = CTRA( X_o,Z_o,psi,v,w+J_presecion,a  ,ego_x1 ,ego_x2, ego_psi,dT);
JA(2,5) = ( Z_o1-Z_o2  )/J_presecion;
[  X_o1,Z_o1,psi1,v1,yawr1,a1  ] = CTRA( X_o,Z_o,psi,v,w,a+J_presecion  ,ego_x1 ,ego_x2, ego_psi,dT);
JA(2,6) =( Z_o1-Z_o2  )/J_presecion;

JA(3,5) = dT;
JA(4,6) = dT;
end
```